Translational Non-Equilibrium Effects in Reactive Dynamics of Detonations

by

Ramki Murugesan

Thesis supervised by Dr. Matei I. Radulescu
submitted to the University of Ottawa
in partial fulfillment of the requirements for the degree of
Doctor of Philosophy
in
Mechanical Engineering

Ottawa-Carleton Institute for Mechanical and Aerospace Engineering
Faculty of Engineering
University of Ottawa

Publications

The work presented in this proposal has been published in the following articles.

Journal Articles

1. R. Murugesan, N. Sirmas, and M. I. Radulescu, "Non-equilibrium effects on thermal ignition using hard sphere molecular dynamics", *Combustion and Flame*, Vol. 205, 457-465 (2019).

Conference Papers in Proceedings

1. R. Murugesan, N. Sirmas, and M. I. Radulescu, "Molecular level investigation of non-equilibrium effects on thermal ignition of reactive gases", *AIP Conf. Proc.* 2132, 140005 (2019).

Conference Presentations

1. R. Murugesan and M. I. Radulescu, "Role of Translational Non-equilibrium Effects on Reactive Dynamics Controlling the Shock to Detonation Transition Using Molecular Dynamics", 2nd International Symposium on Rarefied Gas Dynamics, Seoul, South Korea (Hybrid), 4th - 8th July 2022.
2. R. Murugesan, N. Sirmas, and M. I. Radulescu, "Non-Equilibrium Effects in Detonations Initiation using Hard Spheres", 27th International Colloquim on the Dynamics of Explosions and Reactive Systems, Beijing, 28th July - 2nd August, 2019.
3. R. Murugesan, N. Sirmas, and M. I. Radulescu, "Investigation of non-equilibrium effects on thermal ignition using molecular dynamics simulations", Proceedings of Combustion Institute - Canadian Section, Spring Technical Meeting, Ryerson University, Toronto May 14-17, 2018.

4. R. Murugesan, N. Sirmas, and M. I. Radulescu, "Thermal ignition revisited with three-dimensional molecular dynamics: role of fluctuations in activated collisions", 26th International Colloquim on the Dynamics of Explosions and Reactive Systems, Boston, 30th July - 4th August, 2017.

Declaration of Authorship

I hereby certify that this thesis is entirely my own original work except where otherwise indicated. I am aware of the University of Ottawa regulations concerning plagiarism, including those regarding consequent disciplinary actions. Any use of the works of any other author, in any form, is properly acknowledged at their point of use.

Abstract

Detonation waves in gases are very complex, involving a highly transient cellular structure and a turbulent reaction zone coupled with transverse shocks. The role of out-of-equilibrium phenomena in these waves remains unclear despite extensive research on the underlying physics. On the small scales, translational non-equilibrium associated with shocks, as postulated by Zel'dovich, may significantly affect the chemistry, and these effects are not yet fully understood. Similarly, very fast chemical processes may involve out-of-equilibrium effects due to local energy release that has been postulated by Prigogine. On larger scales, detonation waves display a cellular structure and are supported by turbulent combustion. The present thesis aims to quantify the importance of these three out-of-equilibrium effects on ignition, wave amplification, and diffraction limits of detonations.

First, the role of translational non-equilibrium in reactive dynamics in the thermal explosion problem is investigated using molecular dynamics (MD) simulations and continuum models. Ignition delays are calculated and compared with rates from kinetic theory. MD results show agreement with the Prigogine and Mahieu corrections to the reaction rate evaluated from kinetic theory assuming a Maxwell-Boltzmann distribution. Accounting for the departure from translational equilibrium was found to reduce the ignition delay by up to 30% specifically at high activation energies. However, at low activation energies, the standard equilibrium rate shows a longer delay by up to 60%. The molecular dynamics simulations reveal that translational non-equilibrium effects accelerate activated exothermic reactions, referred to as "molecular hotspots".

The second part of the study focuses on the impact of thermal non-equilibrium and its coupling with reactive kinetics in shock-to-detonation transitions in gases. Results suggest that shock-induced ignition and transition to detonation involve non-equilibrium reactions that overlap with the shock structure, showing strong translational non-equilibrium with reactive fingers. Comparison with continuum simulations using different approximations reveals that shock amplification rate and transition to detonation are approximately twice as fast as predicted by conventional Euler hydrodynamic models, despite evidence of non-equilibrium. A Navier-Stokes model with hard sphere transport properties effectively captures the acceleration process, indicating significant implications for modeling gaseous detonations with fast reactions and strongly coupled pressure wave dynamics and reactivity in the detonation structure.

In the last part of the thesis, the 3D hydrodynamic structure of cellular detonations is modeled by a global 1D mean hydrodynamic average model. Transport properties are artificially increased to account for the high-speed behavior resulting from fast turbulent diffusion. The existence of steady state Navier-Stokes detonation structure, as studied by Wood, is critically reviewed for this purpose and compared with transient calculations. Observations reveal that in the hyper-diffuse model, the shock and reaction zone overlap, resulting in a thickened reaction zone. The 1D model is used to study diffraction dynamics, with critical diffraction occurring when the tube diameter approaches the hydrodynamic reaction zone thickness. After diffraction, the complex viscous detonation structure separates, resulting in a rapid flame transitioning into a weak detonation.

The conclusion of the present survey on the role of out-of-equilibrium effects on detonation dynamics suggests that non-equilibrium ignition due to molecular hotspots may give rise to corrections on the reaction rates by at most a factor of two. The coupling of exothermic reactions with the non-equilibrium structure of shock waves also predicts rates of shock amplification different by a factor of two from the standard Euler model for ignition, but accounting for the diffusive effects brings the MD and continuum predictions into closer agreement. Similarities with the out-of-equilibrium hydrodynamic structure of detonations are discussed.

Acknowledgements

My PhD journey has been an enriching experience, and I would like to express my gratitude to those who made it possible. Firstly, I would like to extend my heartfelt thanks to my supervisor, Dr. Matei I. Radulescu, for his exceptional guidance and unwavering support throughout my doctoral study. His mentorship, patience, and insightful discussions have helped me hone my research skills and made me a better writer. His contribution has been invaluable, and I am deeply indebted to him.

I would also like to express my appreciation to the members of the Detonation and Reactive Dynamics Laboratory (DRDL) at the University of Ottawa for their academic assistance and friendship. The camaraderie and happy memories we shared will always be cherished.

Finally, I must thank my parents, wife, family and friends for their endless love, consistent support, and constant encouragement. Their belief in me has been a driving force, and I would not have achieved this milestone without their moral support.

I wish to acknowledge Natural Sciences and Engineering Research Council of Canada (NSERC) for their financial support to Dr. Matei I. Radulescu through the Discovery Grant, "Predictability of detonation wave dynamics in gases: experiment and model development".

Table of Contents

List of Tables

List of Figures

Chapter 1

Introduction

1.1 Motivation

Detonation waves are self-propagating combustion waves that travel at supersonic speeds [3]. Gaseous detonation waves are encountered in explosion safety applications and propulsion applications, such as the rotating detonation engine, pulse detonation engine and oblique detonation engine. Their reaction zone structure is transient, characterized by a frontal cellular structure and a turbulent reaction zone combined with transverse shocks [2]. This complexity makes them difficult to study experimentally and computationally. Figure 1.1 provides an example of the reaction zone structure obtained in a narrow channel, such that the cellular dynamics are mainly two-dimensional, along with an explanatory sketch. Traditionally, these waves are modeled using the Euler hydrodynamic description with kinetics provided by assuming local thermal equilibrium and neglect of viscous effects. Shocks are treated as jump discontinuities, and their inner physical structure is not explicitly accounted for in current models.

At small scales, these waves may exhibit a range of non-equilibrium phenomena that are not yet understood. Zel'dovich et al. suggested the importance of translational non-equilibrium in shocks, whereby the energy levels in pair-collisions can be much larger than at equilibrium [10]. This can in turn facilitate chemical rates at the shock wave, as suggested by Velikodnyi [11]. On the other hand, Prigogine et al. postulated that the energy released during a chemical reaction can lead to local deviations from thermodynamic equilibrium, resulting in out-of-equilibrium effects that can impact local reaction rates [8]. Despite these early suggestions, their role in detonation waves has not been studied. The main objective of the present thesis is to evaluate these two effects.

On larger scales, detonation waves display a cellular structure and are supported by turbulent combustion. The cellular structure of detonation waves has been extensively studied and has been shown to have a significant impact on the detonability of a given mixture [12, 13]. However, comprehending their structure is challenging due to the strong coupling between gasdynamic effects and fast chemical reactions. The reactive compressible turbulence in their structure has not been satisfactorily modeled, even in an approximate manner.

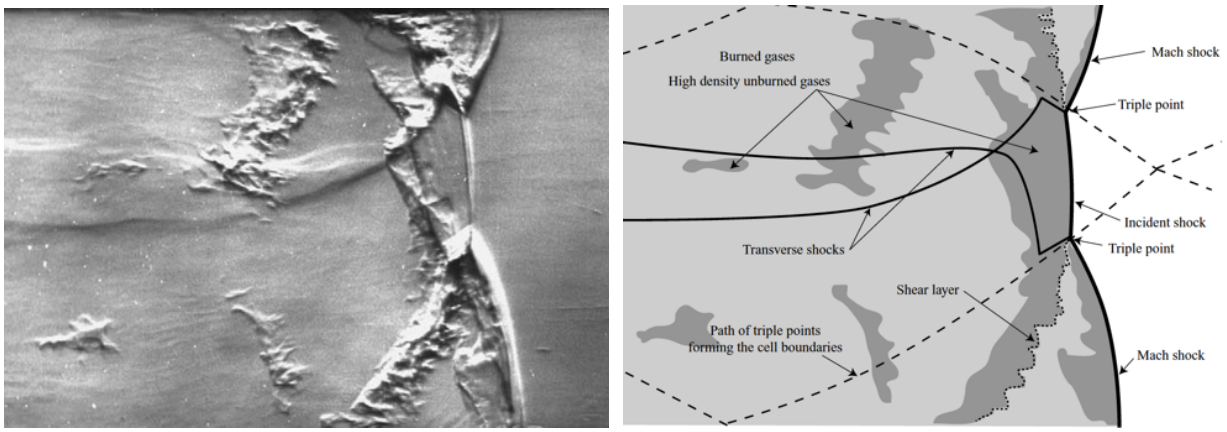

(a) (b)

Figure 1.1: Schlieren photograph of detonation structure in a $CH_4 + 2O_2$ mixture at 3.4 kPa initial pressure, and explanatory sketch [2].

This thesis revisits the fundamental assumption of thermal equilibrium and neglect of shock structure by addressing the role of thermal non-equilibrium and coupling with reactive kinetics in the problem of thermal ignition, shock-to-detonation transition internal to the detonation structure and detonation diffraction. These generic problems encapsulate well the coupling between gas-dynamics and reactivity. In the first two problems, addressing a single model exothermic reaction, a bottom-up approach is taken, starting with the kinetic theory description of reactive gases. A top-down approach for the hydrodynamic structure of cellular detonations in the third problem is used to establish the magnitude of the effective turbulent diffusion of detonations, which are treated in a mean one-dimensional (1D) way.

1.2 Thermal Ignition of Reactive Gases

Thermal ignition of a reactive gas involves the classical coupling between the temperature of a reactive mixture of gases and the rate of energy addition, which depends exponentially on temperature. A slight increase in the system's temperature by chemical reactions may bring the system into a runaway reaction occurring faster than any potential loss [14]. Thermal ignition is particularly relevant to low temperature ignition in hydrogen, for example [1].

A proper account of the reaction rate of elementary reactions is essential in problems of thermal ignition. Although most reaction rates of elementary reactions are obtained or calibrated from experiment, their assumed Arrhenius form is justified theoretically from arguments of kinetic theory of gases or transition state theory only if the gas can be assumed to be in thermodynamic equilibrium, i.e., the distribution of molecular speeds follows the Maxwell-Boltzmann distribution. While the assumption of a Maxwell-Boltzmann distribution is expected asymptotically in the limit of slow reactions, i.e., when the activation energy is large and the heat release is negligible, deviations from the Maxwell-Boltzmann

(MB) distribution are expected otherwise.

The problem of non-equilibrium associated with reactive systems has gained a considerable amount of attention in the literature for a long time [15–23]. Most of the researchers employed the Chapman-Enskog method of solution of the Boltzmann equation [24]. On the other hand, in the mid 1980s Dean and Westmoreland considered the need for including the chemically activated states in association and dissociation reactions to the kinetic models using QRRK (Quantum Rice-Ramsperger-Kassel) theory [25, 26]. They also studied the temperature and pressure dependence of the rate constants of individual reactions due to these chemically activated intermediates. For some of the elementary reactions in combustion, they identified that the radical production reaction in high temperature and the recombination reaction in low temperature plays a crucial role in combustion relevant conditions and concluded that these reactions become more pressure-dependent at high pressures. In this context, in recent years many researchers [27–31] have investigated the non-equilibrium effects specific to low-temperature combustion processes. Burke et al. proposed that the non-Boltzmann reaction sequence involved in low temperature chain branching processes significantly affect the evolution of the system [29]. Labbe et al. studied the impact of including non-equilibrium effects for the formyl radical, HCO, in simulations of laminar flame speeds in which HCO has been a prescient indicator for heat release in combustion of hydrocarbons and predicted a 7-13% increase in laminar flame speed [30]. In a similar manner, Goldsmith et al. focused on the non-Boltzmann effects of low-temperature chemistry of propane oxidation and concluded that these effects can affect the kinetics of subsequent reactions [31]. On the other hand, Döntgen et al. [27, 28] investigated the new pathway of *beta*-scission of rotationally excited radicals formed through hydrogen abstraction. They reported that hot *beta*-scission was not only found to increase the rate of dissociation, but also dominates the fuel radicals at temperatures above approximately 1050 K and pressures up to 100 atm.

Prigogine and co-workers were the first to consider the non-equilibrium effects in single reactions by extending the classical perturbation method of Chapman and Enskog to the case of reactive collisions of hard spheres [8, 15]. They investigated two separate problems: the non-equilibrium effects arising in an isothermal system [15] and in a reactive system, where the energy release may influence the rate of reactions explicitly by perturbing the spatially local MB distribution [8]. The latter is particularly important for the problem of interest in the present work, namely thermal ignition. In the isothermal case, the non-equilibrium corrections to the MB-derived rate of standard kinetic theory of gases was found to be small in such Chapman-Enskog perturbations to the MB distribution [15]. Subsequent work by other groups confirmed this finding [21, 22], although problems have been raised regarding the uniformity of the Chapman-Enskog expansion. The advent of affordable calculations using molecular dynamics (MD) or Direct Simulation Monte Carlo (DSMC) techniques [17, 19, 20, 32] permitted evaluation of the predictions of the kinetic theory results. Although a systematic comparison has not been performed over an entire parameter range of activation energies and heats of reaction, the computational results confirmed that the corrections in the isothermal case tend to slow down the reactions. More interestingly, however, is the reactive case treated in the perturbation theory of Prigogine and Mahieu. Their results indicate that the effect of heat release significantly

accelerate the reaction rate through non-equilibrium effects. That is, the reactive collisions through local energy addition give rise to highly energetic particles that serve to initiate other reactive collisions locally, before the effect is equilibrated in the entire system. In this case, the perturbation is proportional to the ratio Q/E_A, where Q and E_A are the heat release and activation energy, in that the energetic systems will benefit from these effects.

Recently, more relevant to the present study, Sirmas et al. have investigated the role of non-equilibrium effects in the problem of thermal ignition in a model system characterized by a single binary reaction by molecular dynamics in two-dimensions [6]. They have identified large departures from the equilibrium prediction at both low and high activation energies. It was observed that systems with low activation energies exhibit a homogeneous ignition event with departure from thermal equilibrium prediction, yielding lower reaction rates and longer ignition delays. On the other hand, for systems with sufficiently high activation energies and heat of reaction, they have proposed that the thermal ignition is a stochastic process with ignition due to hot-spot formations which is associated with shorter ignition delay than predicted from continuum models by approximately 30%. While these results pointed to the importance of non-equilibrium effects, the 2D problem can be argued to display a stronger propensity for non-equilibrium than 3D because of the reduction in dimensionality. In 1D for example, the gas never relaxes to a Maxwell-Boltzmann distribution. The results of their study suggest that the reduction in dimensionality of the system may further enhance the non-equilibrium effects and highlight the need for more comprehensive modeling approaches that can account for these effects in a more realistic and accurate manner. The present thesis reports such 3D simulations aimed to evaluate the role of translational non-equilibrium in reactive kinetics in thermal explosion problems.

1.3 The Reaction Zone Structure of Detonations

Over the past fifty years, researchers [33] have demonstrated that self-sustaining detonations in gaseous mixtures are unstable and have an unsteady cellular structure. Numerical investigations [34–36] have shown that mildly irregular detonation structures can be recovered accurately using Euler's equations of fluid motion with sufficient resolution. However, these equations do not take into account turbulent mixing or molecular diffusion in the reaction zone. The experiments and numerical simulations conducted by Radulescu et al. [2], for modeling highly irregular mixtures, with much higher activation energies, highlighted the importance of diffusive phenomena in determining the global reaction rate in methane-oxygen detonations. The obtained solutions were subject to changes in resolution and did not converge to unique solutions, despite providing some insight into the possible roles of shock compression or turbulent motions in detonation propagation. Researchers in the past have utilized Favre-averaging to obtain a one-dimensional description of the reaction zone structure of turbulent detonations by modeling the average reaction rate and turbulent transport terms [37]. However, to match experimental results for the critical initiation energy, they have artificially augmented the transport terms, leading to comparable diffusive and convective time scales. Direct Numerical Simulation (DNS) [38, 39] of the Navier-Stokes equations attempts to resolve the full spectrum of scales, including molecular dif-

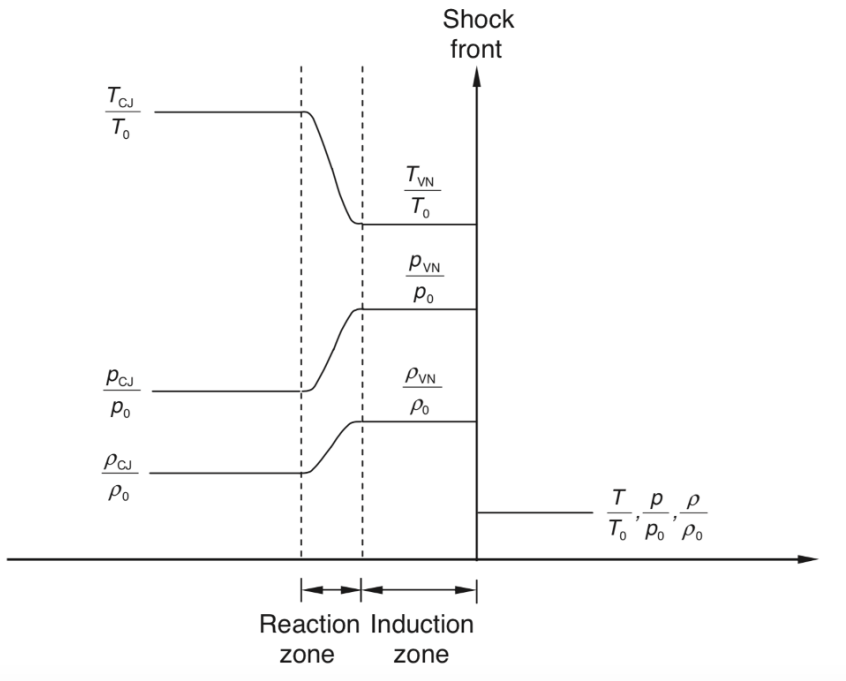

Figure 1.2: ZND model [3].

fusion effects, but practically attainable resolutions in full-scale two-dimensional problems are insufficient to capture correct reaction rates of unburned pockets. Thus, full-scale DNS is limited to providing insight on single-isolated events, such as triple point collisions [40]. Turbulence inherently contains three-dimensional limitations where two-dimensional flows produce larger-scale fluid motions compared to realistic three-dimensional flows due to the dissipation of turbulent motions being dependent on the ability of vortices to stretch in the third dimension [41–43]. Studies in the past [38, 44] have shown that Large Eddy Simulations (LES) can provide insight into sub-grid turbulent mixing effects that contribute to highly irregular detonation reaction rates. A turbulent modeling strategy has been developed for closing reaction rates on flows that are highly compressible, reactive, and contain rapid transients in pressure and energy. This strategy builds on a previously developed Linear Eddy Model for LES [45–47], which was limited to modeling weakly compressible flows in multiple dimensions. A recent study [48] utilized the Compressible Linear Eddy Model-LES (CLEM-LES) method to investigate the impact of turbulent mixing on detonation propagation in a narrow channel with premixed methane-oxygen at low pressures. Findings revealed that changing the mixing rates substantially impacted the detonation structure, cell size, and formation of un-burned pockets. The authors concluded that turbulent mixing and surface reactions were the primary mechanisms driving detonation propagation.

1.4 Reactions within the Shock Structure?

The structure of detonation waves is three-dimensional and is comprised of transverse shock waves traversing through gases at different stages of their decomposition, influenced by variations in lead shock strength [33]. The large variation in leading shock strengths [34] leads to a distribution of reaction rates behind different shock regions varying by several orders of magnitude, due to the exponential dependence of chemical kinetic rates on temperature. This high shock sensitivity results in unreacted pockets behind the front [12, 49, 50], irregularity in cell structure, and fine cellular substructure [51]. While the lead shock is spatially separated from the exothermic region by a distinct induction zone, as depicted in Fig. 1.2, the scenario is much less clear for transverse shocks. Experiments have indicated that unburnt gas pockets (as depicted in Fig. 1.1) react faster than anticipated from fundamental continuum descriptions, with turbulence being the primary reason suggested in the past [52]. However, non-equilibrium effects caused by overlapping ignition phenomena and wave propagation can also contribute. To date, the burning mechanism of these pockets and how they affect the detonation dynamics on larger scales is still not well understood.

A significant aspect of detonation waves is the occurrence of ignition phenomena at relatively high temperatures of 1000 to 2000 K. In these conditions, the problem of auto-ignition can be susceptible to translational non-equilibrium effects, although they are usually ignored for slow activated reactions. However, they can play a role in a hot environment, where a few collisions may trigger an exothermic event, which may occur within the non-equilibrium structure of transverse shocks.

The problem of transverse shock waves propagating through a reactive field can be encapsulated in the model problem of shock to detonation transition. In this canonical problem, a piston impulsively acquires a steady speed starting from rest, driving a shock in the reactive gases. The induced exothermicity by the shock provides further acceleration to the shock, which eventually transits to a detonation. This phenomenon is well-understood when the reactions are modeled by a single step Arrhenius exothermic reaction [53, 54] and non-equilibrium effects and molecular transport phenomena are neglected. The problem thus serves as a simple test-bed to determine the influence of non-equilibrium effects in a single reaction. This is the topic of the second investigation presented in this thesis. In condensed media, there is also an ongoing debate whether lead shock-induced exothermicity may depend on non-equilibrium properties of the shock, such as its strain rate. Gilman [55] suggests that mechanochemistry may play an important role. Some evidence for such strain rate dependent initiation of chemistry stems from the experiments of Armstrong et al. [56]. Their shock-initiation of hydrogen peroxide using ultrafast laser-driven shocks found reactions occurring within 100 ps immediately behind the lead shock. Molecular dynamics simulations confirmed this ultrafast response, suggesting the possibility of strain rate dependent initiation. There is also evidence that the reactions happen within the shock structure. One such study is that by Brenner and colleagues [4], who conducted numerical experiments using molecular dynamics study on a model 2D semi-infinite energetic molecular solid described by reactive many-body potentials. They studied the shock-induced chemistry in the reactive medium and related it to the continuum theory of planar detonations. They have also shown that in condensed phase,

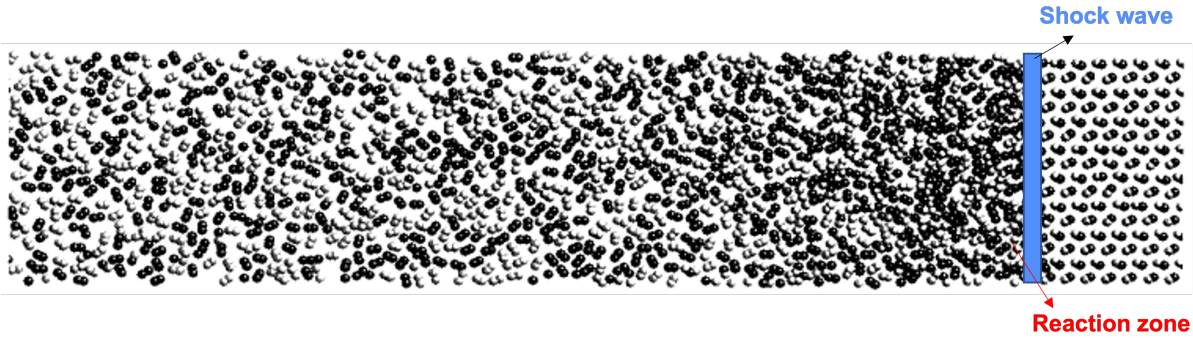

Figure 1.3: Snapshot of a chemically sustained shock wave at 15 ps initiated by a four-layer flyer plate with an impact velocity of 6 km/sec. The two types of atoms are depicted in black and white. The shock front is propagating from left to right [4].

detonations are supported by chemically sustained shock waves (see Fig. 1.3). Similarly, Heim and co-workers [5] indicated that condensed phase detonations with realistic molecular properties can sustain detonations with 2D instabilities. The detonation propagated with velocities higher than CJ and their predicted reaction zone structure was convoluted with the structure of transverse wave. An example of their observations is reproduced in Fig. 1.4, the degree of reaction shown on the left and the density profile is shown on the right. Fig. 1.4(f-j) shows that the reactants are completely burnt immediately after the triple point, indicating the overlap of reaction zone with the shock structure. The same phenomenon is also seen in the degree of reaction plot especially in Fig. 1.4(e) on the left. Anderson and Long [57] also observed similar phenomena in model gas phase detonations using Direct Simulation Monte Carlo (DSMC) simulations. They confirmed that at high activation energies (20 kcal/mol), the reaction and shock waves overlap as opposed to the continuum assumption. In the same study, they reported that for low activation energy, not only do the shock and reaction zones overlap, but they also form an ultrafast detonation, higher than CJ speed. While the reaction rate was chosen in an *ad hoc* manner in this study, the results spark questioning whether such physics persist when reaction rates follow strict magnitudes given by the frequency of collisions. The MD simulations performed in the present study will permit these earlier claims and provide models at the continuum level that can predict these effects to be substantiated. The last section of the thesis discusses the magnitude of diffusive terms required to obtain weak detonations propagating at speeds larger than CJ, and their relation to the laminar and turbulent structure of real detonations.

1.5 Global Model for the Detonation Structure

On the small scales of detonations, many phenomena remain unknown. This precludes simulations from first principles with predictive capability. Nevertheless, approximate engineering models can still be posed at large scales. A hydrodynamic description at large scales has been advocated as early as the study of White [58] and Rybanin [59] in the

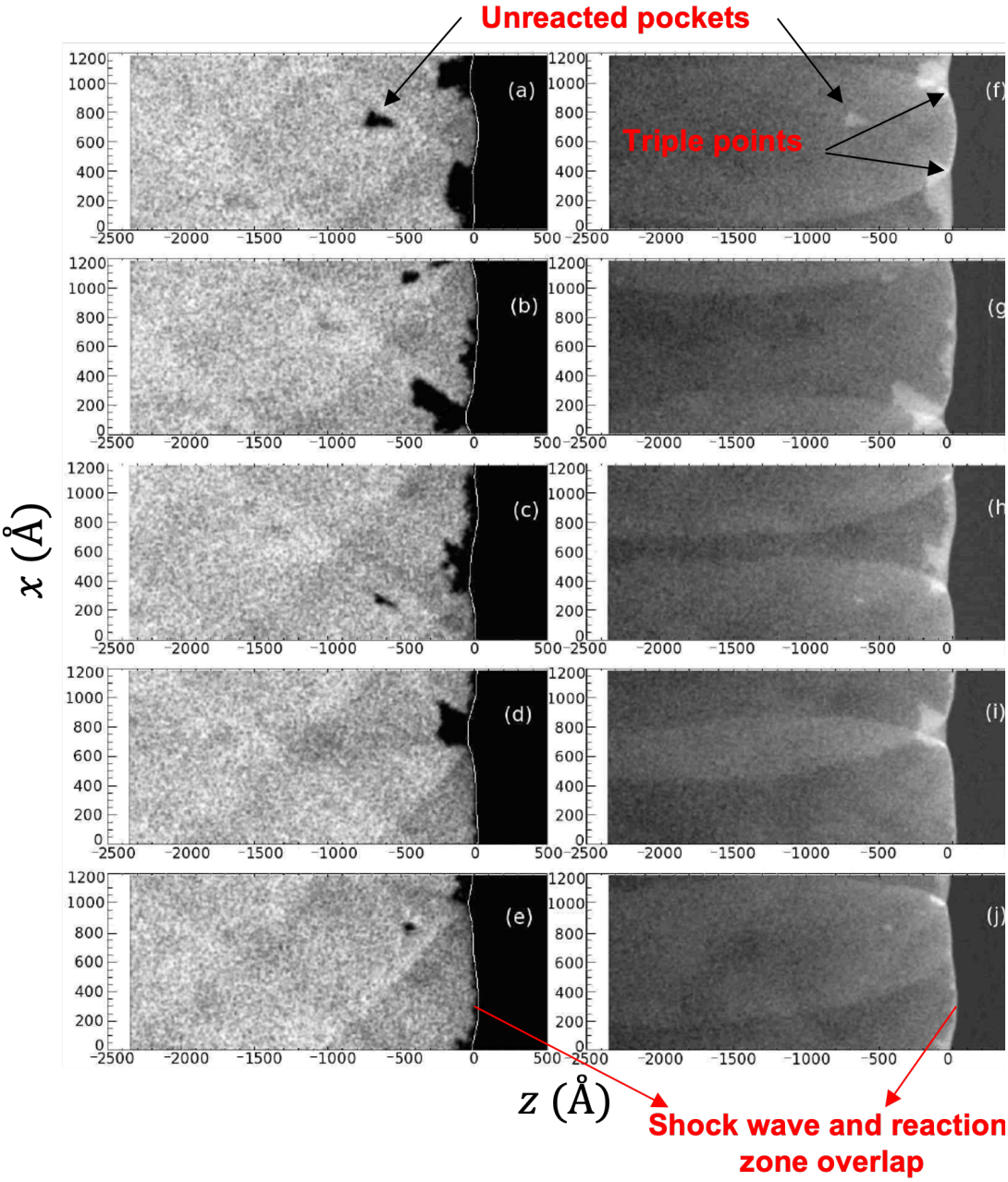

Figure 1.4: Time evolution of the degree of reaction (left column), defined as the fraction of particles in the product state, and the number density (right column). White lines indicate the position of the shock front. Values increase from black to white. From top down, each row is at time t = 44.5, 47.4, 50.3, 53.1, and 56.0 ps [5].

1960s, adopting essentially a Reynolds-Average Navier-Stokes approach for turbulence closure. This was further refined to involve Favre averaging [2, 37, 60]. Closure is of course required for the equivalent Reynolds stresses and global reaction rates. To date, closure of these terms, even empirically, has been limited to few studies [37, 61].

An important metric for closure was advocated by Lee and Radulescu [62] to be the hydrodynamic thickness of the wave, i.e., the average distance between the mean lead shock position and the surface at which the average speed of the gas is sonic with respect to the front. In fact, Lee et al. [63] have proposed earlier the hydrodynamic thickness as a fundamental characteristic length for cellular detonation. The study by Edwards et al. [64] used pressure data along the detonation tube wall to locate the sonic surface in detonations. They observed that the onset of the expansion wave occurred around 4λ to 10λ downstream of the leading front, where λ refers to the preferred spacing between interacting detonation modes. Soloukhin [65] also observed the onset of the expansion wave to be about 4λ downstream of the leading front, which is in agreement with the findings mentioned earlier.

A second metric for closure is the empirical evidence that unstable detonations propagate at velocities higher than Chapman Jouguet values. Experimental results show that detonations in gases travel at velocities 1 to 2% higher than CJ, when extrapolated to zero losses (e.g., infinite tube diameter for detonation in tubes). One study reported [66] that for initial pressures between 0.5 and 3 atm, the detonation speeds are systematically higher (0.3 to 1%) and (0.8 to 1.1%) than CJ for C_3H_8+$5O_2$ and C_2H_4+$3O_2$, respectively. Similarly, the extrapolation of experimental results by Radulescu et al. and Xiao et al. [13, 67], when there is no loss, shows that the detonation travels approximately 1% and 3% higher than CJ for ethylene-oxygen and propane-oxygen mixtures, respectively.

Interestingly, the study of 1D viscous detonations of Wood does predict weak detonations with propagation speeds above the CJ value for sufficiently high diffusivities [68]. Such weak detonations have been later confirmed in numerical simulations by Gamezo et al. [69] in a study for an effective 1D model of high speed turbulent flames. Super-CJ detonations have also been reported by Anderson and Long in their DSMC study [57] and by Mi et al. [70] and later by Radulescu and Shepherd [71] in 1D models with pulsed reactions.

An approximate 1D macro-scale model for turbulent detonations is proposed. The model consists of a simple 1D Navier-Stokes model where the reaction rate is calibrated to recover the desired hydrodynamic thickness and the augmented transport in real detonations modeled by a standard gradient assumption. Diffusion coefficients are then calibrated such that the correct super-CJ detonation speed is recovered, according to Wood's theory.

The last part of the thesis reviews Wood's theoretical model for weak detonation structures and provides numerical verification of the different steady solutions predicted. The dynamics of such weak detonations are then studied in the context of detonation wave diffraction and compared with experiment.

An extensive review of the detonation diffraction problem can be found elsewhere [9, 72, 73]. When a detonation emerges from a tube or channel into open space, the detonation is first weakened by diffraction process. If the initial lateral expansion is sufficiently

strong, for small tubes or channels, the detonation decouples into a shock flame complex. Otherwise, a detonation is reformed on a critical length scale of a few cells. Schultz [73] provides a comprehensive review of diffraction studies up to 2000. Despite extensive research over six decades, critical conditions for detonation diffraction have not been predicted from first principles. Semi-empirical models, such as the one proposed by Schultz, are currently used to estimate the critical tube diameter. The empirical evidence for a wide range of mixtures suggests that the ratio of critical tube diameter to detonation cell size, d_c/λ, is approximately equal to 13 for detonation diffraction from tubes, with a generally larger value observed in detonations with very regular structures [74]. Edwards et al. [75] verified this correlation with cell width for acetylene mixtures and extended it to hydrogen mixtures. In channels with 3D cellular structure, the ratio of critical channel height to cell size, W_c/λ, varies between 3 and 6, with a smaller value in some systems, which is not well understood. Lee [76] discussed the relation between the hydrodynamic thickness of the wave and the critical tube diameter for transmission.

Edwards et al. [75] used soot foils and streak camera records to describe re-initiation at criticality occurring in the immediate vicinity of the unsteady expansion head intersection with the tube axis. They observed a steady decay of shock velocity after the unsteady expansion head propagated to the tube axis in the sub-critical case, while the shock velocity dropped to $0.6V_{\mathrm{CJ}}$ before accelerating back to V_{CJ} in the super-critical case. More recently, Zangene et al. [9] performed detonation diffraction experiments in several hydrocarbon-oxygen mixtures with a more irregular structure in a channel geometry. Through high speed video, they have resolved the evolution of the detonation front with adequate spatial and temporal resolution. The fidelity of the proposed hydrodynamic model to predict the dynamics of the experimentally observed detonation diffraction process is further discussed in the last section of the thesis.

1.6 Objectives and Structure of the Thesis

The questions that arise can be categorized into three parts. Firstly, it is of interest to determine whether non-equilibrium chemical kinetics are faster or slower when compared to equilibrium kinetics. Secondly, it is important to assess the effect of non-equilibrium when there is a coupling between chemical kinetics and gas dynamic shocks. Lastly, this study aims to investigate if the multi-dimensional hydrodynamic reaction zone can be modeled in a mean 1D way using a simple viscous model when calibrated to recover the correct detonation speed. The present thesis thus aims to quantify the importance of these three out-of-equilibrium effects on ignition, wave amplification, and diffraction limits of detonations. By studying the behavior of detonation waves under various conditions, this study hopes to gain a better understanding of the non-equilibrium phenomena that occur in detonations.

The organization of the thesis is as follows: Chapter 2 discusses the impact of translational non-equilibrium effects on thermal ignition in a three-dimensional space without flow, using molecular dynamics simulations of hard sphere gases. The chapter compares the analytical predictions of non-equilibrium kinetic theory with MD simulations. Chapter

3 explores the impact of translational non-equilibrium effects on the coupling of hydrodynamic phenomena and reactive dynamics in the problem of shock to detonation transition in gases. The chapter compares the MD and continuum models and discusses their differences in terms of structure and evolution.

Chapter 4 presents a 1D model to analyze the 3D hydrodynamic structure of cellular detonation and reviews a numerical technique to integrate steady-state hyper-diffusive detonations involving a global reaction zone. The model is also used to study the diffraction dynamics of detonations. Chapter 5 concludes the thesis and provides final remarks on the study.

Chapter 2

Constant Volume Ignition

2.1 Overview

The present chapter examines the impact of molecular non-equilibrium effects on thermal ignition in a three-dimensional physical space. Using molecular dynamic simulations of a one-step exothermic system with chemistry, the release of energy during ignition is observed and compared to available kinetic theory predictions to determine if reactions are accelerated or decelerated with respect to local equilibrium models for the kinetics. The simulation results are compared with analytical predictions of non-equilibrium kinetic theory for both isothermal and reactive collisions. Additionally, the significance of the results for addressing auto-ignition issues in combustion systems, such as the oxidation of hydrogen by oxygen or air, is discussed. Overall, this chapter provides a comprehensive analysis of the role of molecular non-equilibrium effects in thermal ignition problems.

2.2 Problem Definition

The problem addressed in this chapter concerns the evolution of a system of hard spheres within an insulated cube of side L, specifically, a constant volume ignition problem. The hard spheres referred to in this context are particles that only exert force on each other at the instant of collision, where the laws of momentum and energy conservation determine the post-collision velocities [77]. The gas in this system comprises three species, A, B, and C, which may undergo a binary irreversible exothermic reaction according to a specified model.

$$\mathrm{A} + \mathrm{B} \rightarrow \mathrm{C} + \mathrm{C} + \text{heat} \tag{2.1}$$

The focus of this chapter is to investigate and analyze this system, with particular attention to the interplay between the different species and the dynamics of the reactions that occur.

Both reactants and the product have identical mass and diameter, d. Initially, at time zero, the gas is assumed to be in equilibrium, such that the speed distribution follows the

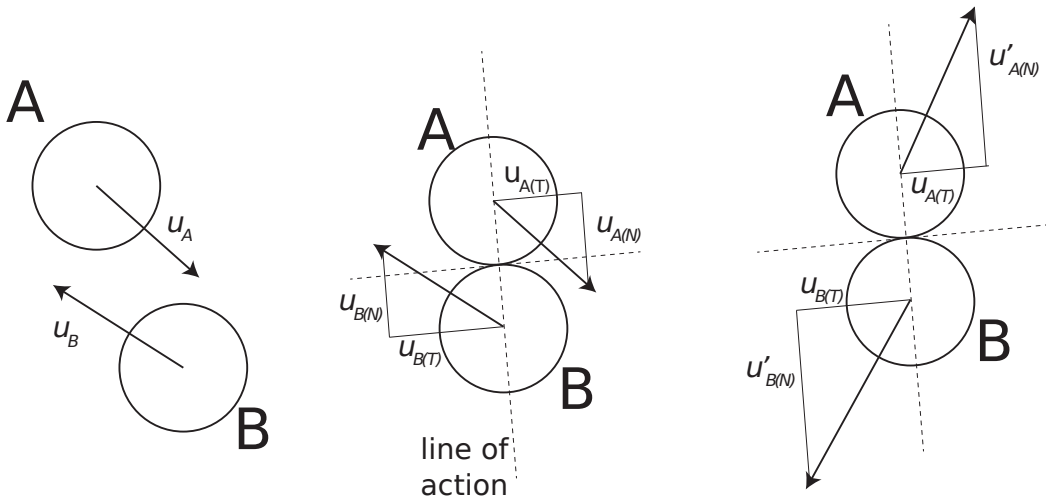

Figure 2.1: Schematic of interactions between particles A and B before impact (left), during impact (center) and after impact (right) along the line of action [6].

Maxwell-Boltzmann distribution. The initial temperature of the system, defined from the mean speed of the particles, uniquely defines the initial condition in the thermodynamic sense. Starting from these initial conditions, the dynamics of the particles inside the box are allowed to evolve, leading to an overall thermal ignition process.

All collisions are assumed to be elastic with the exception of reactive collisions. The heat release Q of a reactive collision increases the kinetic energy of each species C. The collision occurs along the line of action, i.e., the change in the speed can take place only in the normal direction while the tangential components remain unchanged (as seen in Fig. 2.1). The reactive collision can occur only when the relative speed between the two colliding reactants exceeds the minimum impact velocity, u_{cr}, satisfying the condition

$$\left(|u_{\mathrm{A(N)}} - u_{\mathrm{B(N)}}| > u_{\mathrm{cr}}\right) \tag{2.2}$$

The impact velocity is related to the activation energy by

$$u_{\mathrm{cr}} = (4E_{\mathrm{A}}/m)^{1/2} \tag{2.3}$$

The post collision speed of particle A (which becomes a particle C) after a reactive collision, is derived from the energy equation of the form:

$$\frac{1}{2}m_{\mathrm{A}}u_{\mathrm{A}}^2 + \frac{1}{2}m_{\mathrm{B}}u_{\mathrm{B}}^2 + Q = \frac{1}{2}m_{\mathrm{A}}u_{\mathrm{A}}'^2 + \frac{1}{2}m_{\mathrm{B}}u_{\mathrm{B}}'^2 \tag{2.4}$$

The focus of this study is the evolution of the system's temperature for a given initial temperature and species concentrations. Ignition is defined as the time it takes for half of the energy of the system to be released, which corresponds to the depletion of half of the least abundant reactant. Figure 2.2 provides a comparison of the ignition delay obtained using this definition and the ignition delay calculated at the point of inflection

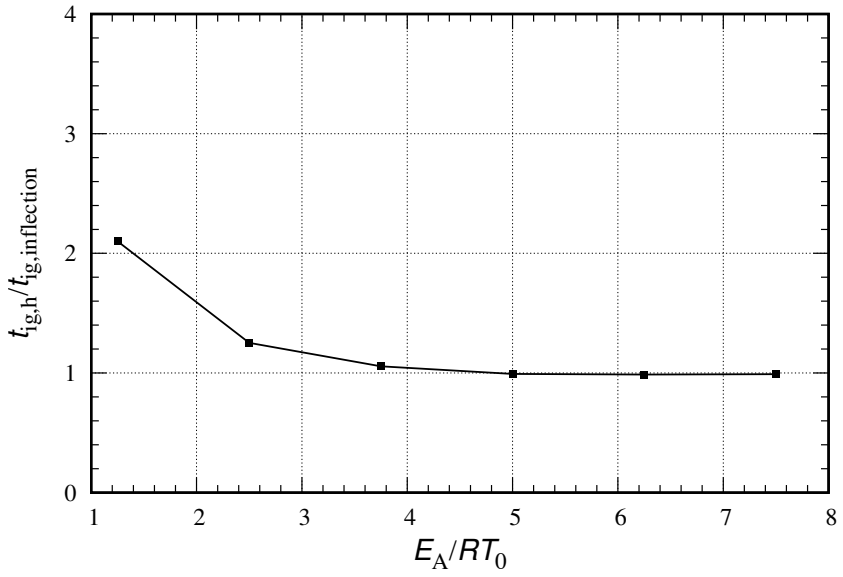

Figure 2.2: Ratio of ignition delay obtained at the depletion of half of the least abundant reactants to the ignition delay calculated at the point of inflection of the temperature profile for various E_A/RT_0 and $Q/RT_0 = 2.5$.

of the temperature profile, for reference. As previously observed [78], both definitions are equivalent for high activation energies, which are typically above 5.

2.3 Molecular Dynamics Description

The evolution of the particles positions and velocities are calculated with the classical Event Driven Molecular Dynamics algorithm [79, 80]. The dynamics of hard sphere models can be determined analytically. For any pair of particles, the collision time can be determined analytically as

$$t^* - t = -\frac{\vec{r}_{ij} \cdot \vec{v}_{ij}}{\vec{v}_{ij}^2} - \left[\left(\frac{\vec{r}_{ij} \cdot \vec{v}_{ij}}{\vec{v}_{ij}^2} \right)^2 + \frac{R_{ij}^2 - \vec{r}_{ij}^2}{\vec{v}_{ij}^2} \right]^{0.5} \tag{2.5}$$

In the current system, t and t^* represent the current and next collision times, respectively. Additionally, $\vec{r}_{ij}$, $\vec{v}_{ij}$, and $R_{ij} = R_i + R_j$ denote the relative distance, relative velocity, and sum of the radii of the colliding spheres, respectively. The system evolves from collision to collision or event to event, hence the name of the algorithm. The method used in this study follows Pöschel's procedure [80] for implementation.

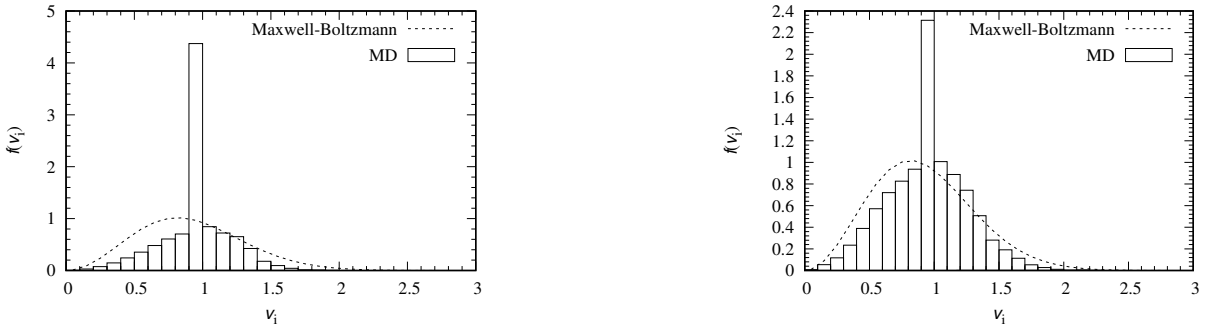

(a) $t = \tau_0$

(b) $t = 3\tau_0$

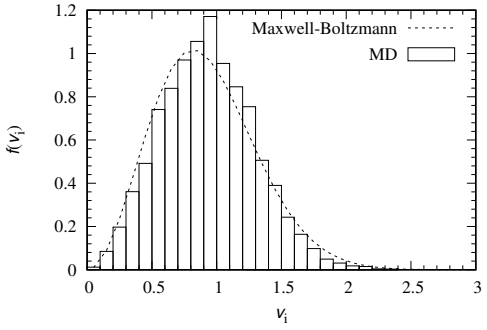

(c) $t = 5\tau_0$

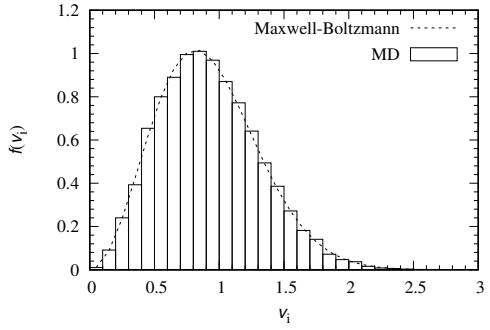

(d) $t = 10\tau_0$

Figure 2.3: Probability distribution of speeds obtained from MD for different times for N=10,000 and compared with MB distribution.

2.3.1 Simulation details

For the initial condition, the numbers of type A and B spheres are specified and denoted as N_A and N_B, respectively. Unless stated otherwise, in all reported calculations, the number of particles for species A and B was equal. The initialization of each calculation included particles with equal speeds and randomized trajectories. This ensures accurate control of the initial temperature (energy) of the system, as it is conserved exactly through elastic collisions. Collisions with the boundaries are treated as reflective. The system is then allowed to evolve with all reactive collisions turned off until all particles undergo a sufficient number of collisions such that their speed distribution converges to the Maxwell-Boltzmann (MB) distribution, which is given by:

$$f(v_i) = \left(\frac{m}{2\pi kT}\right)^{3/2} \exp\left(-\frac{m{v_i}^2}{2kT}\right) \tag{2.6}$$

Figure 2.3 shows an example of the thermalization process. After one mean collision time (Fig. 2.3a), there is a large peak in the distribution, corresponding to the initial speed of the particles. This peak progressively disappears as collisions deplete this class of particles; energy is eventually partitioned in classes of the tails of the distribution. The distribution of speeds is seen to evolve towards the MB distribution within less than 10 mean collision times, τ_0.

Once a thermal equilibrium is achieved among the reactants A and B, reactive collisions are allowed. This marks time 0 of the problem formulation. As very few particles have a high enough speed to give rise to a reactive collision, the rate of energy release in the box is initially slow. As time progresses and the energy released heats the system, more and more particles can undergo reactive collisions. This thermal ignition eventually raises the temperature of the system progressively faster, until depletion of the reactants moderates the rates. The temperature of the system is calculated from the root-mean-square speed of the spheres, $\bar{C}^2$, which is given by:

$$(\bar{C}^2)^{1/2} = (3RT)^{1/2} \tag{2.7}$$

Figure 2.4 shows the evolution of the system's temperature for two such calculations, which show the molecular noise, reflected by different configurations of the system at the same thermodynamic temperature give rise to a stochastic effect in the time of ignition. The calculations were conducted 100 times for each set of parameters of interest, such that the ignition delay reported is the mean value. Likewise, the standard deviation is also recorded, as a measure of the stochasticity. To test the influence of the system size, calculations have been performed by changing the total number of spheres, N, ranging from 50 to 10,000, representing different system sizes. The size of the system was characterized by the side length of a cube, L, which ranged from 1.103 to 6.45 mean free paths. The relationship between the number of particles and the system size can be established by

$$\eta = \frac{N \times V_{hs}}{V} \tag{2.8}$$

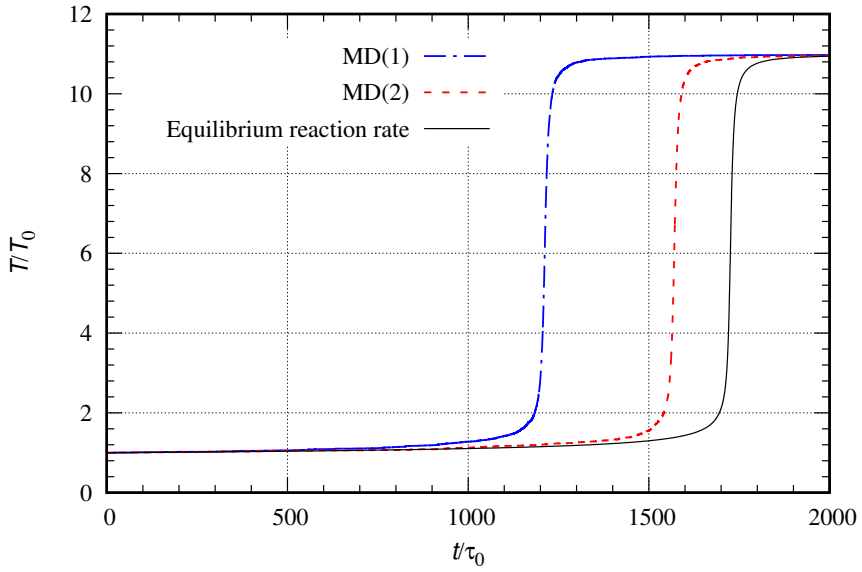

Figure 2.4: Example evolutions of temperature obtained for $N = 10{,}000$ with $Q/RT_0 = 10$ and $E_A/RT_0 = 7.5$.

where, V and V_{hs} are the volume of cube and volume of hard sphere.

All calculations were performed in the ideal gas regime with a particle volume fraction of $\eta = 0.01$. For reference, Fig. 2.5 shows the compressibility factor for various values of η calculated from an equation of state for hard spheres provided by Song et al [81]. The compressibility factor for $\eta = 0.01$ is found to be $Z = 1.04$, which is close to unity (the ideal gas limit) and more than an order of magnitude away from the freezing phase transition. This emphasizes the fact that the value of η used in the present work corresponds to a dilute, ideal gas regime.

2.4 Continuum Level Description from Kinetic Theory

The results from molecular dynamics simulations described in the previous section were compared with those obtained from kinetic theory descriptions, where the reaction rate is either the standard form assuming thermal equilibrium at every instant, or its corrected versions to account for non-equilibrium effects in the evolution of the speed distribution function [8, 15].

For the problem of an insulated system at constant volume, its macroscopic evolution is given by [14]:

$$\rho c_V \frac{dT}{dt} = Q\omega_C \tag{2.9}$$

$$\rho \frac{dY_C}{dt} = \omega_C \tag{2.10}$$

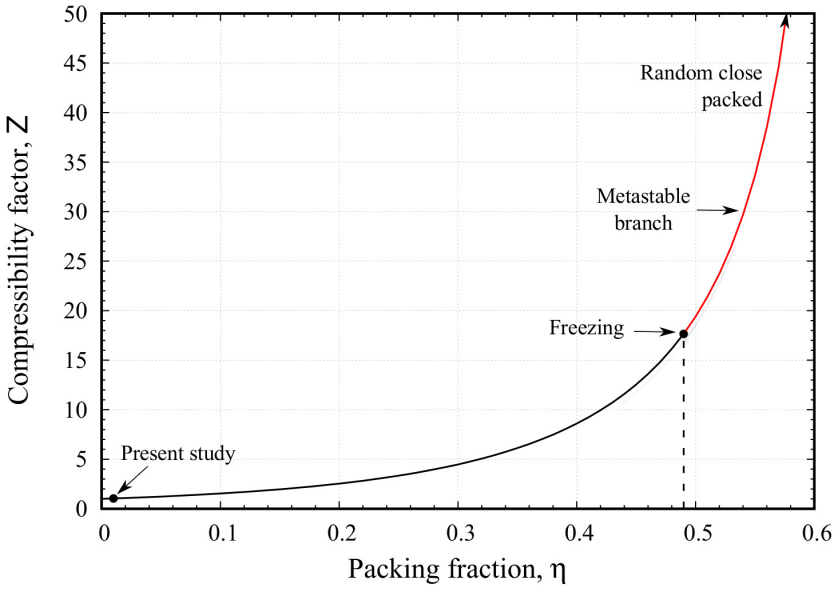

Figure 2.5: Phase diagram of a Hard sphere fluid [7].

where Y_C and ω_C are the mass fraction and the production rate of product C, respectively; c_V is the specific heat at constant volume. Given an initial temperature T_0 and concentrations, the integration of these equations provide the evolution of the system's temperature and concentrations, and hence permits the ignition delay to be determined.

The standard rate of reaction, if one assumes a gas in local thermal equilibrium, takes the form [77]:

$$\omega_C = 48\frac{\eta}{\sqrt{\pi}d}\rho Y_A Y_B \sqrt{T}\exp\left(-\frac{E_A}{T}\right) \tag{2.11}$$

where Y_A and Y_B are the mass fractions of reactants A and B, respectively. η is the volume fraction, ρ is the density and R is the gas constant. The complete derivation of the reaction rate from kinetic theory can be found in the Appendix A.1. The pair correlation function g(η) is

$$g_2(\eta) = \frac{(2-\eta)}{2(1-\eta)^3} \tag{2.12}$$

The initial mean free path and mean free time are ,

$$\lambda_0 = \frac{\sqrt{\pi}d}{8\sqrt{3}\eta g_2(\eta)}; \qquad \tau_0 = \lambda/u_{\mathrm{rms}(0)}$$

For the current study, the length and the time scales are normalized by initial mean free path and initial mean free time of the gas. With this scaling the homogeneous ignition description is independent of η, allowing Q/RT_0 and E_A/RT_0 to uniquely define the

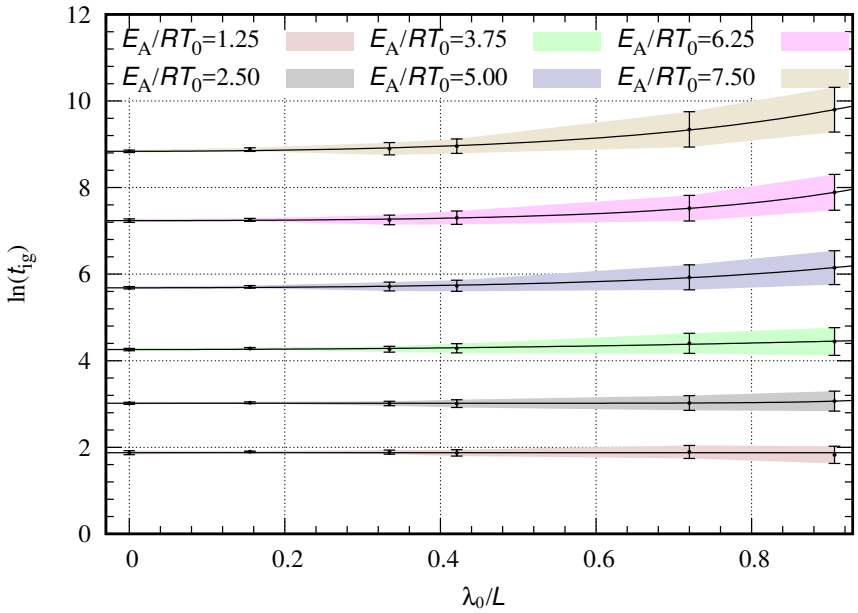

Figure 2.6: Logarithm of ignition delay extrapolated to infinite domain size for $Q/RT_0 = 2.5$. The error bars indicate the standard deviation of ignition delay time. The color band represents the confidence zone of MD results for each activation energy. Solid line indicates the asymptote calculated from Eq. (2.13).

system's evolution.

2.5 Results and Discussion

The results for the ignition delay determined using the MD model described above are shown in Figs. 2.6 and 2.7 for the two values of heat release considered, respectively $Q/RT_0 = 2.5$ and 10. Each data point represents the average ignition delay among 100 calculations, while the error bar is the standard deviation. Each color band in the figure indicates the confidence zone of MD results for a particular activation energy for varying domain size. For all values of Q and E_A, the calculated asymptote falls within the confidence zone of ignition delay time. It is prominent from the figure that the ignition delay and standard deviation decrease with increasing domain size. For low activation energies, regardless of heat release, the ignition delay time is very weakly influenced by the domain size effects. However, for increasing Q and E_A, the trend line is steeper, showing a stronger influence of domain size. For all the calculations performed, the ignition delay was found to converge well to a system of infinite size (abscissa of 0 in the figures).

In order to determine the extrapolated value of ignition delay in an infinite system, the ignition delay dependence on system size was assumed to have the form

$$\ln(t_{ig}) = \ln(t_{ig,\infty}) + b\cosh\left(\frac{c\lambda}{L}\right) \tag{2.13}$$

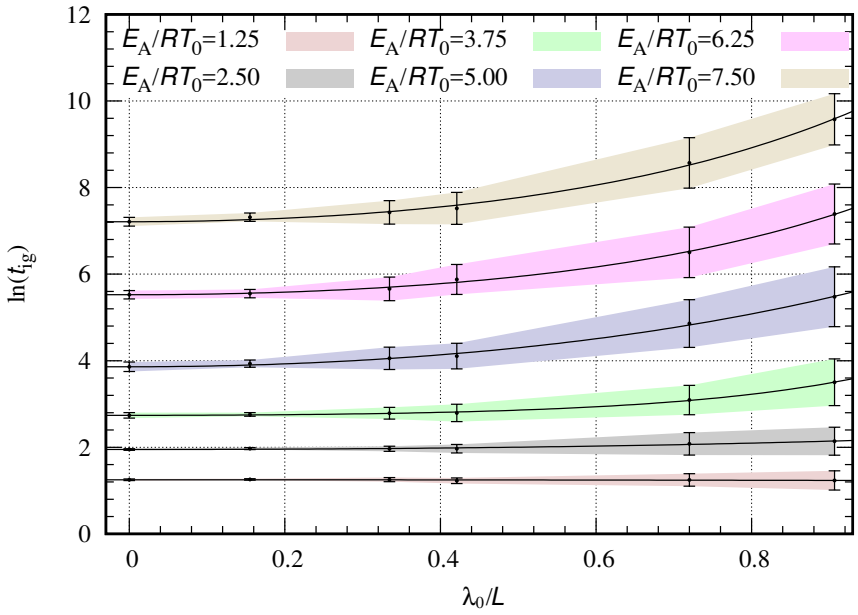

Figure 2.7: Logarithm of ignition delay extrapolated to infinite domain size for $Q/RT_0 = 10$. Same description as Fig. 2.6.

where b, c and $t_{\mathrm{ig},\infty}$ are fitting constants, the latter being the desired ignition delay time at infinite domain size. The fits are also shown in the Fig. 2.6 and 2.7. The presence of uncertainty is inherent in almost all extrapolation methods, which is also represented by error bar for the extrapolated values in Figs. 2.6 and 2.7. Therefore, the obtained values are valid with a confidence of approximately 68%.

The ignition delays extrapolated to infinite domains are shown in terms of the activation energy in Figs. 2.8 and 2.9 for $Q/RT_0 = 2.5$ and 10, respectively. These are compared with three predictions of ignition delay calculated with expressions for the reaction rate from kinetic theory: the thermal equilibrium standard reaction rate (Eq. (2.11)), the rate perturbed by Prigogine and Xhrouet for an isothermal system and the rate perturbed by Prigogine and Mahieu incorporating the effect of energy release.

For the isothermal system, Prigogine and Xhrouet derived the rate ω_{X} [15]:

$$\omega_{\mathrm{X}} = \omega_C \left\{ 1 - \frac{1}{32} e^{-\frac{E_{\mathrm{A}}}{RT}} \left(\frac{E_{\mathrm{A}}}{RT} \right)^3 \left[\left(\frac{E_{\mathrm{A}}}{RT} \right)^2 - 5 \frac{E_{\mathrm{A}}}{RT} + \frac{17}{2} \right] \right\} \tag{2.14}$$

Incorporating the effects of reaction, the non-equilibrium reaction rate, ω_{M}, derived by Prigogine and Mahieu is [8],

$$\omega_{\mathrm{M}} = \omega_C \left\{ 1 + 1.2 Y_{\mathrm{A}} Y_{\mathrm{B}} \left(\frac{Q}{E_{\mathrm{A}}} \right) \right\} \tag{2.15}$$

The reaction rate obtained from the first model (Eq. (2.14)), is found to be lower than the standard reaction rate by 9%, 23% and 20% for activation energies of 2.5, 5 and 7.5,

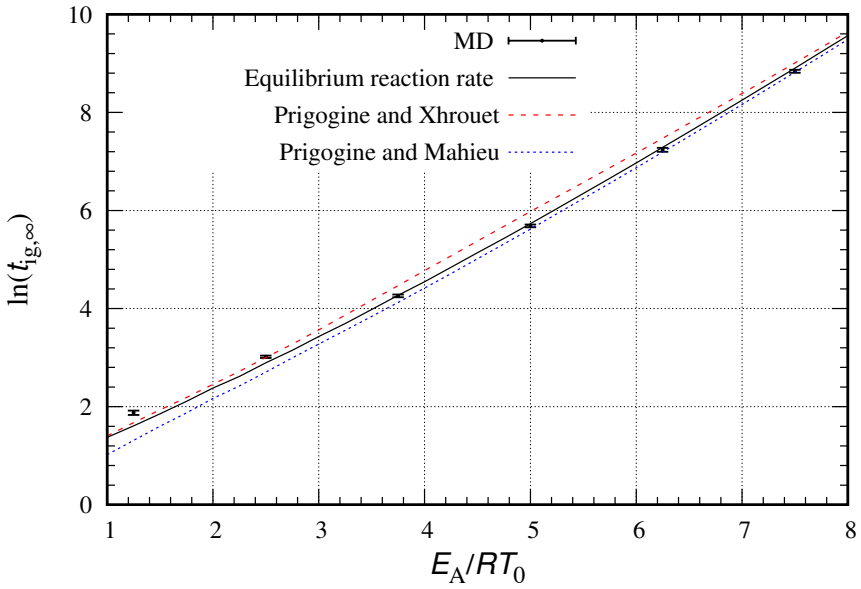

Figure 2.8: Ignition delay time with varying E_A obtained for $Q/RT_0 = 2.5$ from MD (errorbars) are compared with equilibrium reaction rate (solid line) and non-equilibrium reaction rate calculated from Eqs. (2.14) (dashed red line) and (2.15) (dotted blue line).

respectively. Similarly, for the second model, the reaction rate calculated from Eq. (2.15) predicts a reaction rate higher than the equilibrium reaction rate by 10%, 30%, 40% and 120% for Q/E_A ratio of 0.3, 1, 1.3 and 4, respectively. This explains the fact of longer ignition delay predicted by the first model and the shorter ignition delay predicted by the second model. The molecular dynamics results for ignition delay in Fig. 2.8 and 2.9 are compared with those obtained from kinetic theory permits establishing certain clear trends. First, a comparison with the results of standard kinetic theory is made and the differences from it are also shown in Fig. 2.10. For the low value of energy release of $Q/RT_0 = 2.5$, the standard equilibrium kinetic theory captures the trend obtained from the molecular dynamics calculations well, although it slightly over-predicts the ignition delay. Larger deviations are observed for low activation energies, below E_A/RT_0 of approximately 3. In this regime, the ignition delay was found to be longer than predicted by as much as 30% at low activation energies. For the high energy release of $Q/RT_0 = 10$ shown in Fig. 2.9, the predictions of the standard kinetic rate is significantly deteriorated for all activation energies. The largest departure is seen for intermediate activation energies of $E_A/RT_0 = 5$, where the ignition delay calculated from molecular dynamics is more than 30% shorter than anticipated from the standard equilibrium rate. Likewise, for low values of activation energy, the equilibrium model predicts an ignition delay longer by 60%.

The isothermal model prediction of Prigogine and Xhrouet, which is shown in red, systematically predicts an ignition delay longer than the one obtained from the equilibrium value. Nevertheless, this model does not capture any of the molecular dynamic results. At large activation energies, this is the opposite trend from both the low heat release and high heat release results obtained in this study. On the other hand, at low activation energies, the isothermal model provides a correction in the correct direction of lengthening

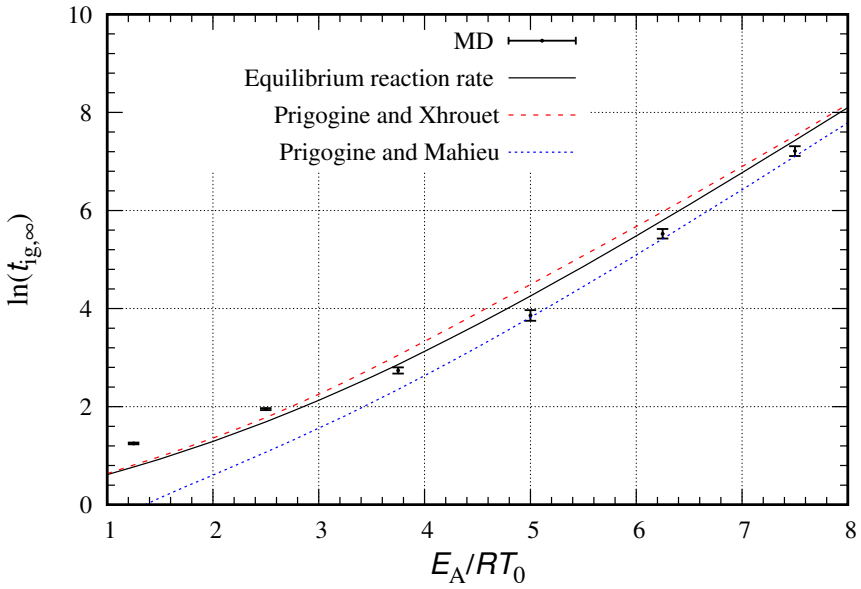

Figure 2.9: Ignition delay time with varying E_A obtained for $Q/RT_0 = 10$. Same description as Fig. 2.8.

the induction delay, but it fails to capture the trend obtained with activation energies approaching unity. According to Prigogine et al., at high temperature, the fraction of reactive collisions is sufficiently high even during the early phases of the run-away process [15]. Therefore, they proposed that the departure from equilibrium can be attributed to the reactions occurring at a faster rate than they are able to transfer their kinetic energy to the non-reacted spheres. Thus, moving the system away from equilibrium. It is these non-equilibrium effects caused by the reactions that yield a higher ignition delay.

Interestingly, the model of Prigogine and Mahieu provides a much better approximation to both low heat release and high heat release results for sufficiently high activation energies only [8]. This model includes the importance of heat of reaction, which can perturb the Maxwell distribution to an appreciable extent in the order of Q/E_A. As a result, the rate of reaction is increased for exothermic reactions and decreased for endothermic reactions. Also, this model demonstrates the inclusion of a sufficiently large heat of reaction which yield a non-equilibrium reaction rate larger than the one derived with the assumption of local equilibrium, using the same perturbation method. Therefore this model is found to be better than the former for the particular problem of thermal ignition, where exothermicity plays a strong role in introducing non-equilibrium effects and modifying the macroscopic rate of reactions. For E_A/RT_0 greater than 5, the prediction is within the standard deviation associated with the stochasticity of the ignition. This result is encouraging, as the model captures the data at the linear order correction in Q/E_A, not requiring higher order terms in the Chapman-Enskog perturbation. At lower activation energies, however, the prediction significantly diverges from the molecular dynamic data for both low and high heat release.

At low temperatures (high activation energy), the good agreement between the calculations and those using the perturbed rate of Prigogine and Mahieu supports the validity

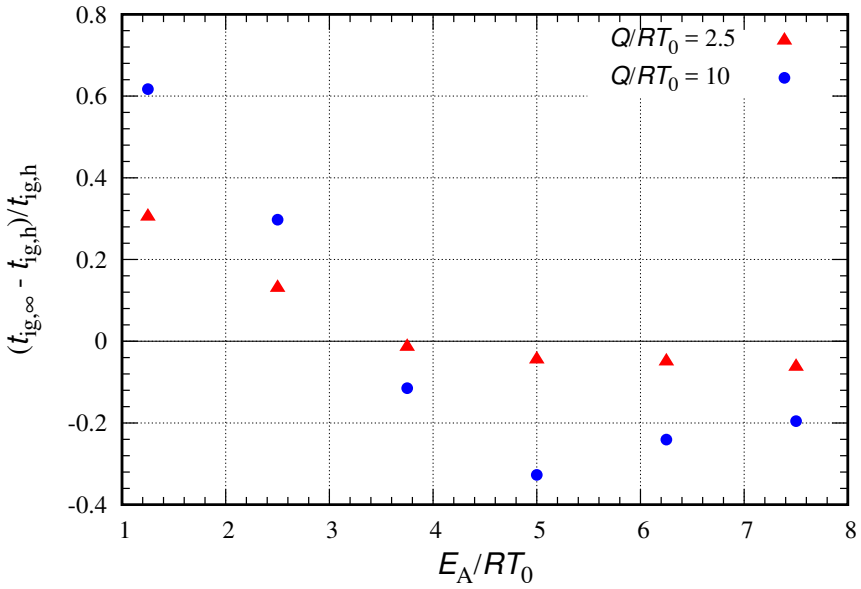

Figure 2.10: Relative difference between ignition delay time obtained from MD and homogeneous mixture.

of the physical mechanism proposed by them. Highly energetic particles resulting from reactive collisions promote local reactions. These particles do not have enough time to equilibrate with the rest of the system, thus giving rise to what is referred to as *molecular hotspots*. This result is also in accordance with the previous numerical results by Sirmas and Radulescu in the two-dimensional system [6]. In this regime of ignition, where non-equilibrium effects significantly promote ignition, there is also a much higher stochasticity of ignition, as shown in Fig. 2.11. As the heat release and activation energy are increased, so is the stochasticity among the 100 simulations, measured by the standard deviation. Interestingly, this is also the regime where ignition is *mild* in practice: it takes the form of localized ignition spots [82, 83]. In this regime, the picture that emerges is the ever-increasing role of molecular fluctuations. In a previous study [6], the authors compared their results only with reaction rates assuming homogenous ignition. Whereas, in the present work along with the equilibrium reaction rate, the results are compared with the existing kinetic theory models which takes into account the effect of heat of reaction while calculating the reaction rate. For high Q and low E_A, the ignition delay is found to be 50% longer than equilibrium kinetic theory in 2D whereas, it is 60% in 3D. Similarly, for high Q and high E_A, the delay time is approximately 30% lower than equilibrium kinetic theory in both 2D and 3D. However, the low heat release case is not much affected by the presence of third dimension and recovers the 2D results well by roughly about 3% difference. When compared to 2D simulations, the standard deviation of ignition delay for both low and high heat release case is reduced almost by 2% and 20%, respectively. These results show that the statistical fluctuations become important with growing Q and E_A. Also, it is to be noted that the ignition delay calculated in 2D are not extrapolated to infinite domain as discussed in this study. Therefore, it can be concluded that the magnitude of the results is different, but the trend followed by each set of parameter recovers the same as obtained

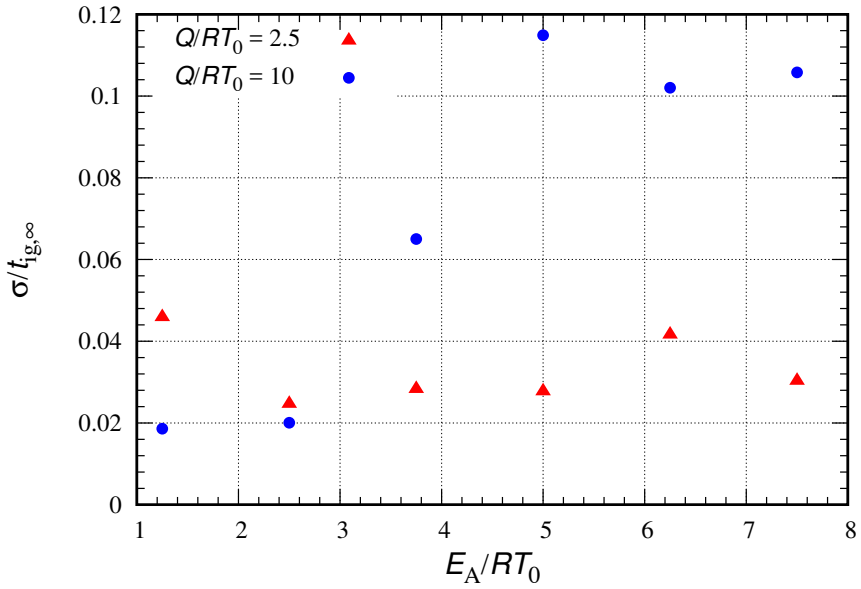

Figure 2.11: Standard deviation of ignition delay times obtained from MD for different values of heat release.

Table 2.1: Comparison of ignition delay time from MD for $N_A = 9\ N_B$ with that obtained for homogeneous ignition for $E_A/RT_0 = 7.5$ and $Q/RT_0 = 10$.

	Ignition time (t_{ig}), N = 10,000					
	A+B			9A+B		
	Equilibrium	Molecular Dynamics	Standard Deviation	Equilibrium	Molecular Dynamics	Standard Deviation
	1682.4	1502.6	151.5	4868.4	4631.5	403.1
Relative Difference		-10.98			-4.86	

from 2D.

For all the simulations discussed above, the proportion of species A and B were equal and no diluent was introduced. However, in actual combustion systems, other species may be present, hence representing a potential heat bath to absorb part of the energy released and diminish the magnitude of the non-equilibrium effects documented. To investigate this, separate calculations were performed with an initial mixture of 9A+B, where the excess A acted as a diluent. Table 2.1 reports the results performed in the undiluted and diluted cases for $Q/RT_0 = 10$ and $E_A/RT_0 = 7.5$ using $N = 10{,}000$ particles. In the diluted regime, the ignition delay was found lower than the one predicted with the assumption of Maxwell-Boltzmann distribution by approximately 5%, whereas the difference was approximately 11% for the non-diluted case. This clearly shows that the non-equilibrium effect reported will be a strong function of dilution. These are left for future study.

It is also of interest to comment on the relevance of the present results for problems of auto-ignition in combustion systems, as for example the oxidation of hydrogen by oxygen

Table 2.2: Activation temperature T_a(K), heat of reaction $\bar{Q}$(J/mol) and heat of reaction temperature $\bar{Q}/\sum_{\text{Reactants}} \nu_i R_u$ (K) of reactions controlling ignition processes in hydrogen (partially adapted from Sanchez and Williams [1]- see text).

		T_a(K)	$\bar{Q}$(J/mol)	$\bar{Q}/\sum_{\text{Reactants}} \nu_i R_u$(K)
1	$H + O_2 \rightarrow OH + O$	8590	-70158	-4219
2	$H_2 + O \rightarrow OH + H$	3165	-7810	-470
3	$H_2 + OH \rightarrow H_2O + H$	1825	62814	3777
4	$H + O_2 + M \rightarrow HO_2 + M$	0.0	196599	11823
5	$H_2 + O_2 \rightarrow HO_2 + H$	27888	-239399	-14397
6	$H_2O_2 + M \rightarrow OH + OH + M$	25703	-213974	-25736
7	$HO_2 + HO_2 \rightarrow H_2O_2 + O_2$	5556	179110	10771
8	$HO_2 + H_2 \rightarrow H_2O_2 + H$	12045	-60289	-3625

or air. It is now relatively well established that low temperature ignition in hydrogen is governed by a thermal mechanism of initiation [1]. Nevertheless, the reaction network controlling the ignition process is not a single reaction, but a local network of reactions. In hydrogen chemistry, the chemical mechanism is sufficiently simple to qualitatively comment on the potential role of non-equilibrium effects discussed in the present paper. The eight important reactions are listed in Table 2.2 [1]. Also listed in this table is the activation temperature and an equivalent heat of reaction calculated in dimensions of Kelvin (Q/R), such that their division by the local temperature yields the relevant parameters $E_A/RT = T_a/T$ and Q/RT. The relevant low temperature regime of auto-ignition to be discussed is around 1000 K - 1300 K depending on the pressure, as referenced in [1]. This shows that non-dimensional activation energies lie in the range 0 to 30 and the heat release in the range -26 (negative means endothermic) to 12. This shows that non-equilibrium effects associated with low activation temperatures discussed in the present study may directly affect the reaction rates of reactions 2, 3, 4 and 7. On the other hand, the hot-spot mechanism associated with high heat release and high activation energy may *directly* affect mostly reaction 7, as other highly energetic recombination reactions (e.g., reaction 4) have negligible activation. Likewise, reactions 5 and 6 may be slowed down through equivalent cold spots due to their strong endothermicity.

Nevertheless, reaction networks may bring non-equilibrium hot spot effects in sequence of energetic reactions (giving rise to non-equilibrium high speed molecules B) followed by high activation reactions involving the molecule B. This is precisely the case for hydrogen ignition at low temperatures. At temperatures below cross-over, hydrogen auto-ignition is controlled mainly by the auto-catalytic role of hydrogen peroxide (H_2O_2) through the sequence of reactions 6, 3, 4 and 7, leading to the global reaction $2H_2+O_2 \rightarrow 2H_2O$, with the rate controlling step given by reaction 6 [1]. Reaction 6 has a very high activation energy and produces two OH. These proceed through reaction 3, which occurs twice and produces two H atoms which are then consumed by reaction 4 to form two HO_2 in an energetic reaction. These two energetic HO_2 molecules then form a H_2O_2 molecule in the activated and highly energetic reaction 7 to complete the auto-catalytic loop, which occurs locally with negligible influence by transport phenomena. Of interest in this loop is that the

highly energetic hydrogen peroxide molecule then restarts the loop in a very high activation energy reaction. The auto-catalytic H_2O_2 loop thus has the form of the model reaction studied in the present study. Highly energetic products of an exothermic reaction promote local temperature non-equilibrium, which then affect the rate of reactions involving this product. The multiple reaction mechanism is clearly more complicated than the single toy reaction studied in the present work, and future study should focus on multiple reactions such as the auto-catalytic H_2O_2 loop described above. Interestingly, the same H_2O_2 auto-catalytic loop has also been found responsible of auto-ignition in hydrocarbons [84, 85].

In hydrogen low temperature chemistry, the auto-catalytic loop for H_2O_2 described above is also controlled by the concentration of HO_2, which is controlled by another loop sharing the same potential for non-equilibrium effects, the sequence of reactions 8 and 4. The high activation energy reaction 8 consumes HO_2 and produces H, which is consumed by reaction 4 to produce again the highly energetic HO_2. The net reaction of these two is $H_2+O_2 \rightarrow H_2O_2$, and it proceeds through the sequence of highly energetic HO_2 undergoing a highly activated reaction. This second overall step is also very prone to the same non-equilibrium effects through molecular hotspots.

Interestingly, the low temperature auto-ignition of hydrogen is also known experimentally to be very prone to hotspot formation, as first shown by Meyer and Oppenheim [82]. This is generally attributed to the high sensitivity of the ignition delay to fluctuations, inherited from the very high activation energies of reactions 6 for the first loop and 8 for the second loop controlling the auto-ignition. Future study should clearly address whether the propensity for hot spots observed experimentally for this regime is due mainly to coupling to hydrodynamic scale fluctuations [83, 86–88], molecular non-equilibrium effects, or the acceleration of slow reactions by quantum tunneling effects [89, 90], or a combination of these.

2.6 Conclusion

The study presented in this chapter reveals the existence of two non-equilibrium regimes in a single model reaction for thermal ignition problems. At high temperatures (low reduced activation energies), the ignition delay is longer than predicted by standard kinetic theory assuming local equilibrium. Although the trend was captured by Prigogine and Xhrouet qualitatively, the perturbation model failed at this extreme, as the perturbation assumes slow reactions in the limit of high activation energy. For low temperatures (high activation energies), particularly for high heat release, the ignition delay was found to be shorter than the one predicted by the standard kinetic theory. The perturbation scheme of Prigogine and Mahieu, which incorporates the effect of energy release in the perturbation of the distribution function, accurately captures the effect.

The corrections found do not exceed a factor of 2. The present study clearly highlights the necessity of incorporating non-equilibrium effects in kinetic predictions, particularly for systems where the kinetics are calibrated experimentally in nearly isothermal conditions, if an accuracy better than a factor of 2 is required. It also clearly shows that no existing

perturbation scheme provides a uniformly valid approximation. Hence, molecular dynamic results, such as provided in the current manuscript, can be used to form empirical correction factors to the existing reaction rates.

The study also suggests that non-equilibrium effects involving energy release can be expected in the auto-catalytic loops of H_2O_2 and HO_2 through local sequences of high energy release followed by high activation reaction of these two species. The magnitude of such corrections is currently unknown. Future research should focus on these auto-catalytic multiple reactions.

Chapter 3

Shock to Detonation Transition

3.1 Overview

The primary objective of this chapter is to investigate the effect of translational non-equilibrium within shock waves on chemical kinetic rates and hence study the coupling between wave phenomena and non-equilibrium energy release. The model problem investigated is the shock to detonation transition in a reactive gas, treated for the single Arrhenius reaction treated in the last chapter. The focus is on transverse waves of detonations, with parameters adjusted in the range of actual reactive conditions. The problem is investigated through molecular dynamics simulations, which are then compared to continuum descriptions obtained by hydrodynamic simulations of reactive Euler and Navier-Stokes models for hard spheres. This comparison permits drawing conclusions on the importance of translational non-equilibrium on fast reactive gasdynamic problems of shock induced chemistry.

3.2 Problem Definition

The problem of shock to detonation transition (SDT) in gases and condensed phase has received considerable attention, due to its practical importance and fundamental nature. In gases, auto-ignition behind reflected shocks is identical in formulation. The dynamics of ignition and transition to detonation are now well understood for simple chemical systems described by one or a few chemical reactions [53, 54, 91, 92] and the neglect of transport and non-equilibrium effects.

In the SDT problem, an impulsively started piston initiates movement with constant speed into a gas initially at rest. As the piston moves forward, a shock wave propagates ahead of it at a constant rate, as depicted in Fig. 3.1. It is assumed that the shock wave has enough strength to raise the gas temperature behind the shock sufficiently in order allow reactive collisions. A convenient ignition temperature is used, close to the initial temperature, in order to ensure the reactions remain frozen in the non-compressed gas.

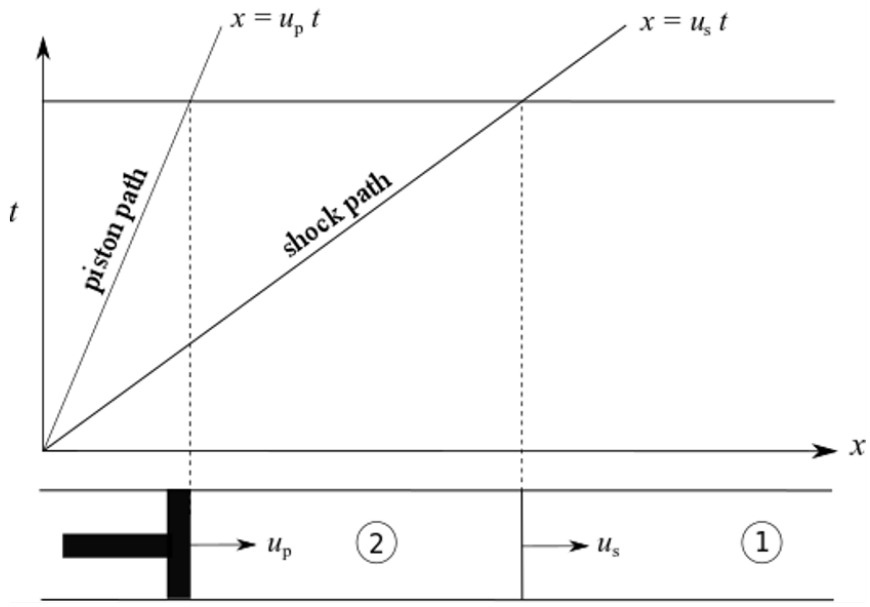

Figure 3.1: Schematic of piston-generated shock wave problem.

The reaction's progress results in the release of chemical heat, further accelerating the shock wave.

3.3 Molecular Dynamics Model

This chapter investigates a 3D system comprised of N identical hard spheres with uniform masses and diameters, occupying a volume fraction of η. Specifically, the study examines the problem of a detonation transition triggered by a shock wave, formulated at the molecular level using the hard sphere gas approach. To this end, the simulation method follows the EDMD algorithm outlined in Chapter 2.

3.3.1 Simulation details

The number of particles for species A and B are equal in all reported calculations, unless otherwise stated, similar to the constant volume ignition problem. However, unlike in Chapter 2, each calculation is initiated with particles at randomized initial trajectories and velocities, which are generated from a Maxwellian distribution. The Gaussian distribution of random variables is derived from the Box-Muller method, as illustrated in Fig. 3.2. This initialization procedure ensures that the system is in equilibrium and that reactions can occur from the start without any thermalization process. To model the reactions, a single irreversible exothermic chemistry is utilized, offering a physically realistic three-dimensional representation of the model presented in Chapter 2.

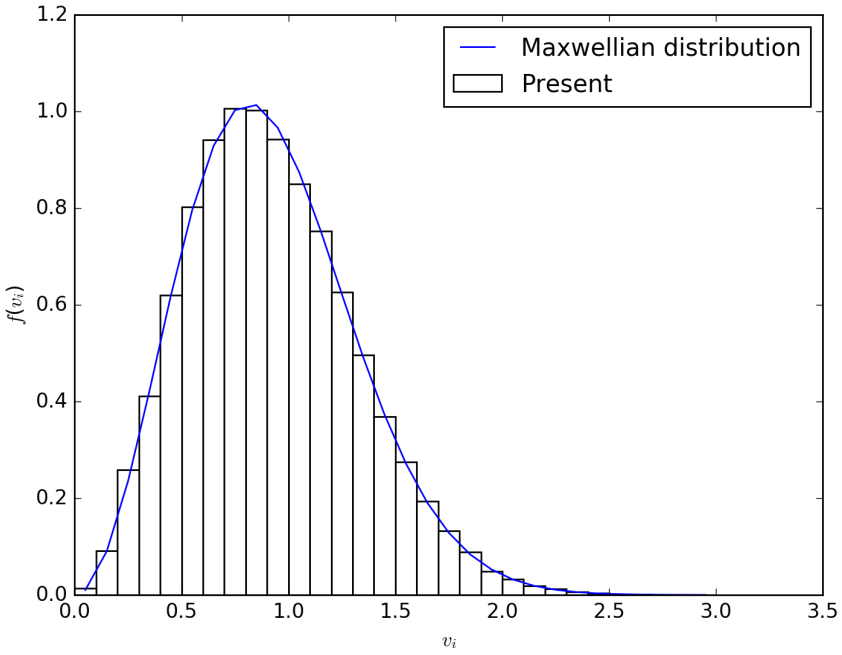

Figure 3.2: Probability distribution of speeds obtained using Box-Muller method compared with MB distribution.

3.3.2 Simulation parameters

Initially, the mixture is in a state of rest. However, at time zero, an abrupt acceleration of the piston is initiated to attain a velocity of u_{p}. The magnitude of the piston's velocity is carefully chosen to achieve a post-shock activation energy of $\bar{E}_{\mathrm{A}}/\bar{R}\bar{T}_{\mathrm{s}} = 5$, a value that holds significance in the context of auto-ignition in shock heated of detonation waves [13]. To investigate the impact of heat release on the transition process, two distinct heat release values are selected for a given activation energy, as delineated in Table 3.1. In this study, a rectangular channel with a third dimension of one mean free path is employed to examine the behavior of the gas in a three-dimensional space, taking into account collisions and interactions. This is because, the computational time scales with the number of particles as $N \log(N)$, and the domain size is influenced by the number of particles as given in equation (2.8). Thus, to account for 3D effects and allow more room for the principal direction of propagation, the z-direction is restricted to one mean free path.

Through the previous investigation of domain effects (refer to Figs. 2.6 and 2.7), it was observed that the results remained largely unaffected when the domain size exceeded the mean free path for the activation energies considered in this study. The size of the domain, particle diameter, volume fraction, and the number of particles remain constant throughout the study.

Table 3.1: Parameters used in MD simulations.

Initial conditions and parameters	Dimensionless values
$(\bar{L}_x \times \bar{L}_y \times \bar{L}_z)/\bar{\lambda}_0$	$102.35 \times 10.325 \times 1.0235$
$\bar{d}/\bar{\lambda}_0$	0.08
η	0.01
No. of particles (N)	40,000
$\bar{u}_\mathrm{p}/\sqrt{\bar{e}_0}$	2.26
$\bar{E}_\mathrm{A}/\bar{R}\bar{T}_\mathrm{s}$	5
$\bar{E}_\mathrm{A}/\bar{R}\bar{T}_0$	20
$\bar{Q}/\bar{R}\bar{T}_0$	20 and 40

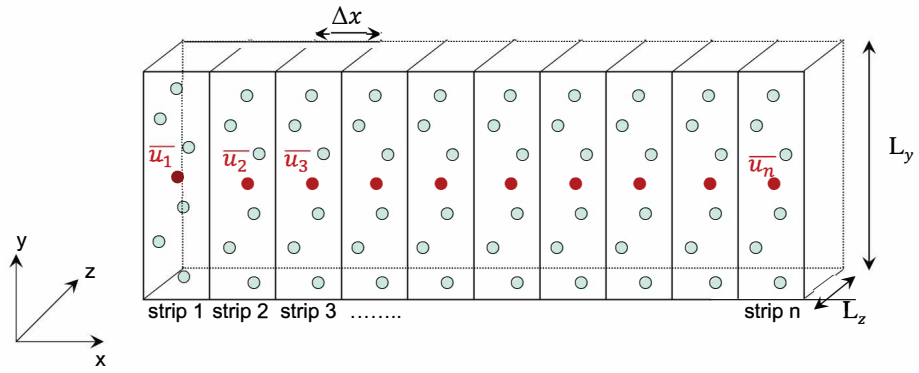

Figure 3.3: Sketch defining the division of domain into small strips for calculating the average properties of the mixture.

3.3.3 Data collection

In the present study, the macroscopic properties of a system consisting of $N = 40,000$ hard spheres are investigated using ensemble averaging. To achieve this, a coarse-grain averaging technique is employed by dividing the domain into vertical strips or boxes of size $\Delta x \times \bar{L}_y \times \bar{L}_z$. These strips are used to obtain a one-dimensional distribution of macroscopic properties by coarse-grain averaging the microscopic properties within them, with a width of $\Delta x = 1\bar{\lambda}_0$, where $\bar{\lambda}_0$ is the initial mean free path. Ensemble averaging is employed in this study to obtain precise measurements of the coarse-grained density and temperature. This is achieved by repeating the calculations with statistically distinct initial conditions, which are generated by randomizing the trajectories of the particles. By averaging the results of 100 simulations with varying initial conditions, the macroscopic properties at each strip can be determined with greater accuracy and reliability. To determine the local temperature $\bar{T}(\bar{x})$ of each strip or box, the internal energies in the $x-$, $y-$ and z directions are averaged over all particles in the strip. In the $x-$direction, the contribution of the mean velocity of the macroscopic motion is subtracted in order to evaluate the thermodynamic temperature. The normalized local temperature at position $\bar{x}$, bounded by the strip of

width Δx, is expressed as follows:

$$\bar{T}(\bar{x}) = \frac{\bar{T}_x + \bar{T}_y + \bar{T}_z}{3} \tag{3.1}$$

$$\bar{T}_x(\bar{x}) = \frac{1}{N(\bar{x})} \sum_{i=1}^{N(\bar{x})} \frac{1}{2} (\bar{u}_{xi} - \langle \bar{u}_x \rangle)^2 \tag{3.2}$$

$$\bar{T}_y(\bar{x}) = \frac{1}{N(\bar{x})} \sum_{i=1}^{N(\bar{x})} \frac{1}{2} (\bar{u}_{yi})^2 \tag{3.3}$$

$$\bar{T}_z(\bar{x}) = \frac{1}{N(\bar{x})} \sum_{i=1}^{N(\bar{x})} \frac{1}{2} (\bar{u}_{zi})^2 \tag{3.4}$$

where $N(\bar{x})$ is the number of hard spheres at position $\bar{x}$ bounded by the strip of width Δx, and $\langle \bar{u}_x \rangle = \frac{1}{N(\bar{x})} \sum_{i=1}^{N(\bar{x})} \bar{u}_{xi}$, is the local mean velocity in the x-direction. The overbar indicates the dimensional values. The local number density in each strip is determined by dividing the number of hard spheres at position $\bar{x}$ bounded by the strip by the volume of the strip.

$$\bar{n}(\bar{x}) = \frac{N(\bar{x})}{\Delta x \times \bar{L}_y \times \bar{L}_z} \tag{3.5}$$

3.4 Continuum Models

In the present study, two different continuum models have been considered for the investigation of the fluid flow. The first model belongs to the category of inviscid hydrodynamic equations, also known as the Euler equations. The second model is based on the viscous hydrodynamic equations, known as the Navier-Stokes equations, which account for the transport properties of the fluid and the diffusive nature of the flow. These two models are the major classification of continuum models and have been extensively used in the field of fluid mechanics.

3.4.1 Governing equations in dimensional form

Euler

Traditionally, the modeling of detonation waves in gases has been accomplished by utilizing the Euler hydrodynamic description, which assumes that the gas is a continuum with uniform properties. In this approach, the kinetics of the reaction are provided by assuming local thermal equilibrium, where the temperature and pressure are assumed to be uniform throughout the gas. The governing equations used for this approach in one dimension are

as follows:

$$\frac{\partial}{\partial \bar{t}}(\bar{\rho}) + \frac{\partial}{\partial \bar{x}}(\bar{\rho}\bar{u}) = 0 \tag{3.6}$$

$$\frac{\partial}{\partial \bar{t}}(\bar{\rho}\bar{u}) + \frac{\partial}{\partial \bar{x}}\left(\bar{\rho}\bar{u}^2 + \bar{p}\right) = 0 \tag{3.7}$$

$$\frac{\partial}{\partial \bar{t}}(\bar{\rho}\bar{e}_{tot}) + \frac{\partial}{\partial \bar{x}}\left((\bar{\rho}\bar{e}_{tot} + \bar{p})\bar{u}\right) = \bar{Q}\bar{\omega}_i \tag{3.8}$$

$$\frac{\partial}{\partial \bar{t}}(\bar{\rho}Y_i) + \frac{\partial}{\partial \bar{x}}(\bar{\rho}\bar{u}Y_i) = -\bar{\omega}_i \tag{3.9}$$

where, $\bar{\rho}$, $\bar{u}$, $\bar{p}$, $\bar{e}_{tot}$, Y_i and $\bar{\omega}_i$ are the density, velocity, pressure, total sensible plus kinetic energy, species mass fraction and reaction rate (Eq. (2.11)), respectively. The total energy is

$$\bar{e}_{tot} = \frac{\bar{p}}{\bar{\rho}(\gamma - 1)} + \frac{1}{2}\bar{u}^2 \tag{3.10}$$

Navier-Stokes (NS)

The next model under consideration involves solving the compressible Navier-Stokes equations in one dimension. These equations not only account for the convective transport of the gaseous mixture, but also incorporate the effects of diffusion, thereby providing a more accurate representation of the system under study. Specifically, the inclusion of the transport properties of the mixture accounts for the diffusive nature of the system, which can have significant implications on the overall behavior of the system. In this model, the transport coefficients, such as viscosity, thermal conductivity, and diffusivity, are assumed to be constant, meaning they do not vary with respect to time, temperature, or other factors. This simplification allows for easier mathematical treatment and numerical simulations.

The governing equations for the model are as follows:

$$\frac{\partial}{\partial \bar{t}}(\bar{\rho}) + \frac{\partial}{\partial \bar{x}}(\bar{\rho}\bar{u}) = 0 \tag{3.11}$$

$$\frac{\partial}{\partial \bar{t}}(\bar{\rho}\bar{u}) + \frac{\partial}{\partial \bar{x}}\left(\bar{\rho}\bar{u}^2 + \bar{p}\right) = \frac{4}{3}\bar{\mu}\frac{\partial}{\partial \bar{x}}\left(\frac{\partial \bar{u}}{\partial \bar{x}}\right) \tag{3.12}$$

$$\frac{\partial}{\partial \bar{t}}(\bar{\rho}\bar{e}_{tot}) + \frac{\partial}{\partial \bar{x}}\left((\bar{\rho}\bar{e}_{tot} + \bar{p})\bar{u}\right) = \bar{k}\frac{\partial}{\partial \bar{x}}\left(\frac{\partial \bar{T}}{\partial \bar{x}}\right) + \frac{4}{3}\bar{\mu}\frac{\partial}{\partial \bar{x}}\left(u\frac{\partial \bar{u}}{\partial \bar{x}}\right) + \bar{Q}\bar{\omega} \tag{3.13}$$

$$\frac{\partial}{\partial \bar{t}}(\bar{\rho}Y_i) + \frac{\partial}{\partial \bar{x}}\left(\bar{\rho}\bar{u}Y_i\right) - \bar{D}\frac{\partial}{\partial \bar{x}}\left(\bar{\rho}\frac{\partial Y_i}{\partial \bar{x}}\right) = -\bar{\omega} \tag{3.14}$$

where, the reaction rate, $\bar{\omega}$, is obtained from the one-step Arrhenius form:

$$\bar{\omega} = \bar{k}_0\bar{\rho}Y\exp\left(\frac{\bar{E}_{\mathrm{A}}}{\bar{R}\bar{T}}\right) \tag{3.15}$$

$\bar{k}_0$ is the rate constant. Applying rigorous kinetic theory to the hard-sphere model yields the following expressions for the transport coefficients. Specifically, when the masses of the gas are equal, the thermal conductivity, viscosity, and self-diffusion coefficients take the following forms, respectively [93]:

$$\bar{D} = \frac{3}{8}\frac{\sqrt{\pi \bar{m} \bar{k}_{\mathrm{B}} \bar{T}_0}}{\bar{\rho}\pi\bar{\sigma}^2}$$
$$\bar{\eta} = \frac{5}{16}\frac{\sqrt{\pi \bar{m} \bar{k}_{\mathrm{B}} \bar{T}_0}}{\pi\bar{\sigma}^2}$$
$$\bar{k} = \frac{25}{32}\frac{\sqrt{\pi \bar{m} \bar{k}_{\mathrm{B}} \bar{T}_0}}{\pi\bar{\sigma}^2}\frac{\bar{c}_{\mathrm{V}}}{\bar{m}}$$

3.4.2 Non-dimensional parameters for the governing equations

The governing equations used are non-dimensionalized using the following scales: the initial density $\bar{\rho}_0$, the initial internal energy $\bar{e}_0 = 3\bar{R}\bar{T}_0/2$, and the initial mean free path $\bar{\lambda}_0$. Applying the scaling yields the following non-dimensional properties:

$$\rho = \frac{\bar{\rho}}{\bar{\rho}_0} \quad T = \frac{\bar{R}\bar{T}}{\bar{e}_0} \quad u = \frac{\bar{u}}{\sqrt{\bar{e}_0}} \quad x = \frac{\bar{x}}{\bar{\lambda}_0} \quad t = \frac{\bar{t}\sqrt{\bar{e}_0}}{\bar{\lambda}_0} \quad \mathrm{Le} = \frac{\bar{k}}{\bar{\rho}_0 \bar{c}_{\mathrm{P}} \bar{D}}$$
$$\mathrm{Pr} = \frac{\bar{\mu}\bar{c}_{\mathrm{P}}}{\bar{k}} \quad Q = \frac{\bar{Q}}{\bar{e}_0} \quad E_{\mathrm{A}} = \frac{\bar{E}_{\mathrm{A}}}{\bar{e}_0} \quad e = \frac{\bar{e}}{\bar{e}_0} \quad \omega_i = \frac{\bar{\omega}_i \bar{\lambda}}{\sqrt{\bar{\rho}_0 \bar{e}_0}}$$

3.4.3 Governing equations in non-dimensional form

Euler

With the application of described scaling, the non-dimensional form of the Euler equations (3.6)-(3.9) can be expressed as follows:

$$\frac{\partial}{\partial t}(\rho) + \frac{\partial}{\partial x}(\rho u) = 0 \tag{3.16}$$
$$\frac{\partial}{\partial t}(\rho u) + \frac{\partial}{\partial x}\left(\rho u^2 + p\right) = 0 \tag{3.17}$$
$$\frac{\partial}{\partial t}(\rho e_{tot}) + \frac{\partial}{\partial x}\Big((\rho e_{tot} + p)u\Big) = Q\omega_i \tag{3.18}$$
$$\frac{\partial}{\partial t}(\rho Y_i) + \frac{\partial}{\partial x}(\rho u Y_i) = -\omega_i \tag{3.19}$$

The reaction rate, ω_i, is the same as the one obtained from equilibrium kinetic theory (Eq. (2.11)).

Navier-Stokes

The Navier-Stokes equations (3.11)-(3.14) in non-dimensional form is given by:

$$\frac{\partial}{\partial t}(\rho) + \frac{\partial}{\partial x}(\rho u) = 0 \tag{3.20}$$

$$\frac{\partial}{\partial t}(\rho u) + \frac{\partial}{\partial x}\left(\rho u^2 + p\right) = \frac{4}{3} C\mathrm{Pr} \frac{\partial}{\partial \bar{x}}\left(\frac{\partial u}{\partial x}\right) \tag{3.21}$$

$$\frac{\partial}{\partial t}(\rho e_{tot}) + \frac{\partial}{\partial x}\left((\rho e_{tot} + p)u\right) = C\frac{\gamma}{\gamma - 1}\frac{\partial}{\partial \bar{x}}\left(\frac{\partial T}{\partial x}\right) + \frac{4}{3} C\mathrm{Pr}\frac{\partial}{\partial x}\left(u\frac{\partial u}{\partial x}\right) + Q\omega \tag{3.22}$$

$$\frac{\partial}{\partial t}(\rho Y_i) + \frac{\partial}{\partial x}(\rho u Y_i) - \frac{C}{\mathrm{Le}}\frac{\partial}{\partial x}\left(\rho \frac{\partial Y_i}{\partial x}\right) = -\omega \tag{3.23}$$

$$\omega = k_0 \rho Y \exp\left(\frac{E_\mathrm{A}}{T}\right) \tag{3.24}$$

The constant C is defined as $C = \frac{\beta_\mathrm{k} 3(\gamma-1)}{2\gamma}$. For the hard sphere gas, the Prandtl number and Lewis number are $2/3$ and $5/4$, respectively. Appendix B provides the procedure used to non-dimensionalize the governing equation. For the sake of simplicity, the overbar is omitted in the rest of this chapter.

3.4.4 Numerical implementation of continuum model

The continuum models mentioned above are numerically implemented using the finite-volume computational package, *MG*, which was developed by Falle and Komissarov [94, 95]. To enhance simulation accuracy, a second-order accurate exact Godunov scheme is employed for the convective terms [96]. Additionally, a Cartesian grid with adaptive mesh refinement [97] is utilized to increase solution accuracy near discontinuities, where significant changes in fluid properties occur.

To investigate the hydrodynamics equations, the flow is studied in the piston frame of reference, where a slip wall boundary is imposed on the left (piston face). Here, the flow travels towards the wall at a constant velocity of u_p. The right boundary, on the other hand, has zero gradient boundary conditions. The computational domain spans 100 mean free paths and is covered by a Cartesian grid with 200 grid points on the base grid. To increase the resolution near regions of significant variation in flow properties, five additional levels of adaptive mesh refinement are added, with each level doubling the resolution when differences between flow properties exceed a tolerance of 0.01. The fixed parameters considered in the simulations are listed in Table. 3.1. This numerical approach provides a valuable tool for studying compressible fluid dynamics and can lead to insights into a wide range of physical phenomena.

A resolution study was conducted to ascertain the required resolution for the simulations, as depicted in Figs. 3.8 and 3.9. Increasing the resolution from $\lambda_0/16$ to $\lambda_0/32$ did not alter the solution profile in both Euler and Navier-Stokes calculations. Hence, for the subsequent chapters focusing on shock evolution using the continuum model, a minimum resolution of $\Delta = \lambda_0/32$ is adopted, where Δ is the cell size.

3.5 Results

For the first case, with $Q/RT_0 = 20$, the piston is initially accelerated from the left into the quiescent reactive medium, creating a shock that eventually transitions into detonation. The resulting temporal evolution of reactant and product species is depicted in Fig. 3.4, with the product sizes magnified for better visualization. The species density and temperature profiles with distance along the x axis in the piston frame of reference for this case are shown in Figs. 3.5a and 3.5b, respectively. As can be seen in the figure, upon establishment of detonation, finger-like reaction stems are observed ahead of the compression wave, contributing to the diffusive structure. These stems continuously formed and are overcome by the compression wave, which is also marked by the rise in the x-component of temperature couple of mean free paths ahead of the other components, as seen in Fig. 3.5b. Furthermore, the species density profile in Fig. 3.5a shows that there is no distinct reaction zone, with the reaction starting immediately after the reactants enter the shock, marked by the immediate formation of the product species profile. This is also evident in the temperature profile in Fig. 3.5b.

The investigation now moves on to the second case, where $Q/RT_0 = 40$. The transition occurs faster in this case due to the more prominent non-equilibrium effect observed with higher values of heat release, as discussed in Chapter 2. The temporal evolution of reactant and product species is depicted in Fig. 3.6, with a magnified view of the product sizes to aid visualization. The temperature and species profiles for this case are shown in Figs. 3.7a and 3.7b, respectively. The resulting finger-like structures ahead of the compression wave act as hotspots, accelerating the ignition process. This is evidenced by the clear temperature peaking for the reactive fingers in Fig. 3.7b. It is important to note that the trend remains consistent for both cases, with the transition occurring faster for higher heat release values.

In order to analyze the initiation process of the detonation wave, Figs. 3.10a and 3.10b provide visual representations of temperature contours in the piston frame of reference for the two heat release cases considered from the Euler model. The figures offer a zoomed-in view of the entire domain to show a detailed picture of the initiation process, with the shock wave visible moving from left to right and marked by the white solid line.

To investigate the non-equilibrium effects in the transition/initiation process, a more detailed analysis of the x-t diagram is carried out. This diagram includes C^+ characteristics, represented by dashed black lines running towards the right, and the particle path, represented by dotted white lines running towards the left. The particles that are shocked first ignite first, and they send some compression waves to the shock to transition to deto-

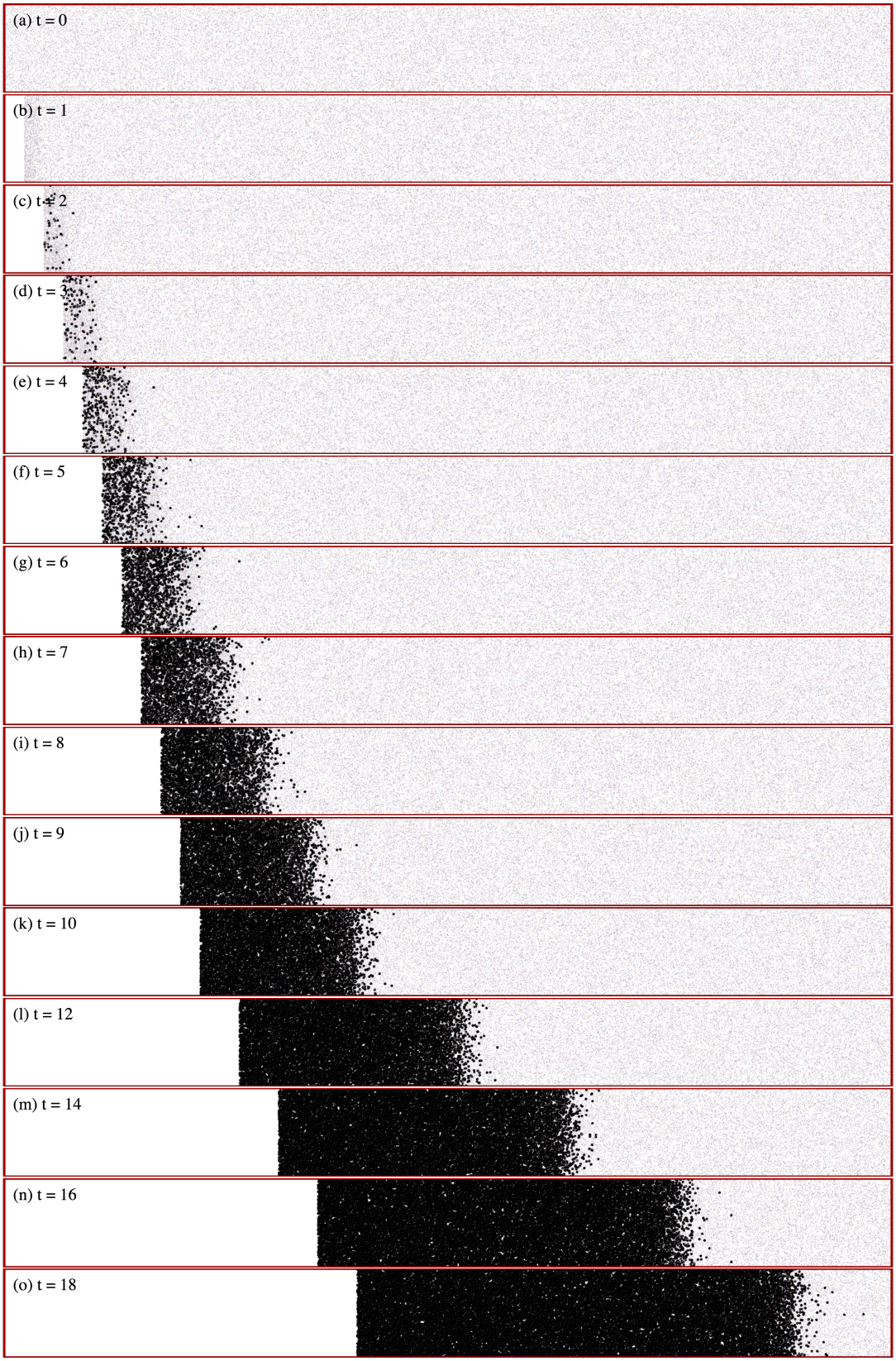

Figure 3.4: Time series snapshot of a sliced three-dimensional box for $\frac{Q}{RT_0} = 20$, $\frac{E_A}{RT_0} = 20$, $\frac{E_A}{RT_s} = 5$ from 0 to 18 mean free time.

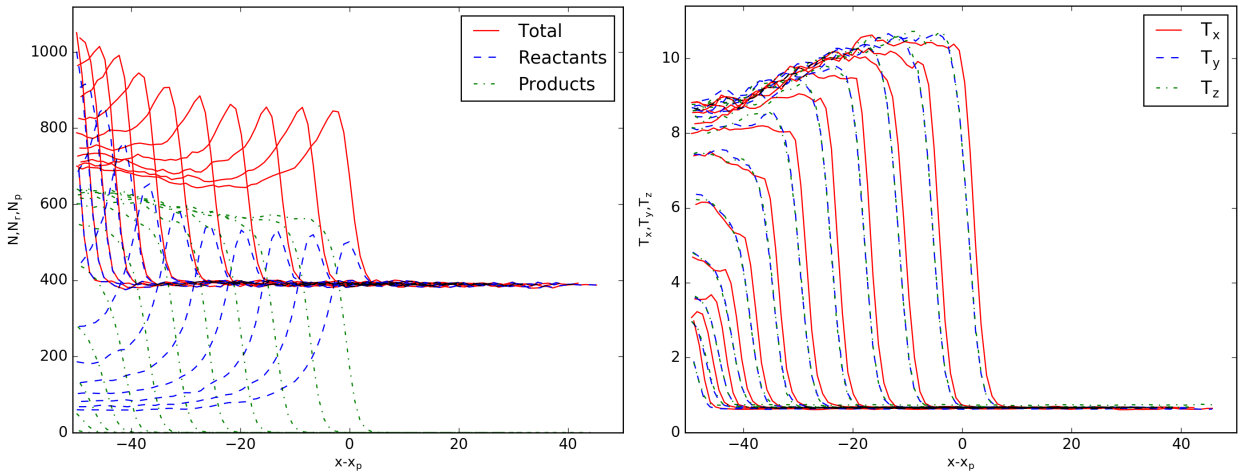

(a) (b)

Figure 3.5: Time evolution of (a) species profile with reactants (dashed blue line), products (dash-dotted green line) and total species (red line) and (b) temperature profile in the piston frame of reference for $\frac{Q}{RT_0} = 20$, $\frac{E_A}{RT_0} = 20$, $\frac{E_A}{RT_s} = 5$.

nation, which is visible in the C^+ characteristics. The location where the C^+ characteristics coalesce marks the transition point.

This analysis provides insights into the initiation process of the detonation wave and highlights the role of non-equilibrium effects in this process. The C^+ characteristics and particle path help to explain the order of ignition and the transition from shock to detonation, as well as the location of the transition point.

3.6 Discussion

To establish a comparison between the results of Molecular Dynamics (MD) and Continuum simulations, the shock speed is analyzed. The MD approach utilizes a coarse-grain technique, which involves averaging the microscopic velocities within each strip, as elaborated in Section 3.3.3. To determine the macroscopic velocity, 100 simulations are averaged. The position of the shock is determined by analyzing the average velocity profile at each time step, and the shock speed is calculated using the distance-time formula. In contrast, the Continuum model tracks the position of the shock front over time, using a particular temperature or pressure threshold. The shock or detonation speed is then calculated using finite-difference approximations from the position data obtained.

The comparison of shock speed between MD and three other models, namely the reactive Euler model, the model based on Prigogine and Mahieu's work on slow reactions considering heat release, and the reactive NS model with one-step chemistry, is performed, as discussed above. Figures 3.11a and 3.11b illustrate the comparison of shock speed between MD and Euler model for both values of heat release considered. The onset of transition in MD is observed to occur faster, with the transition happening around 10 and

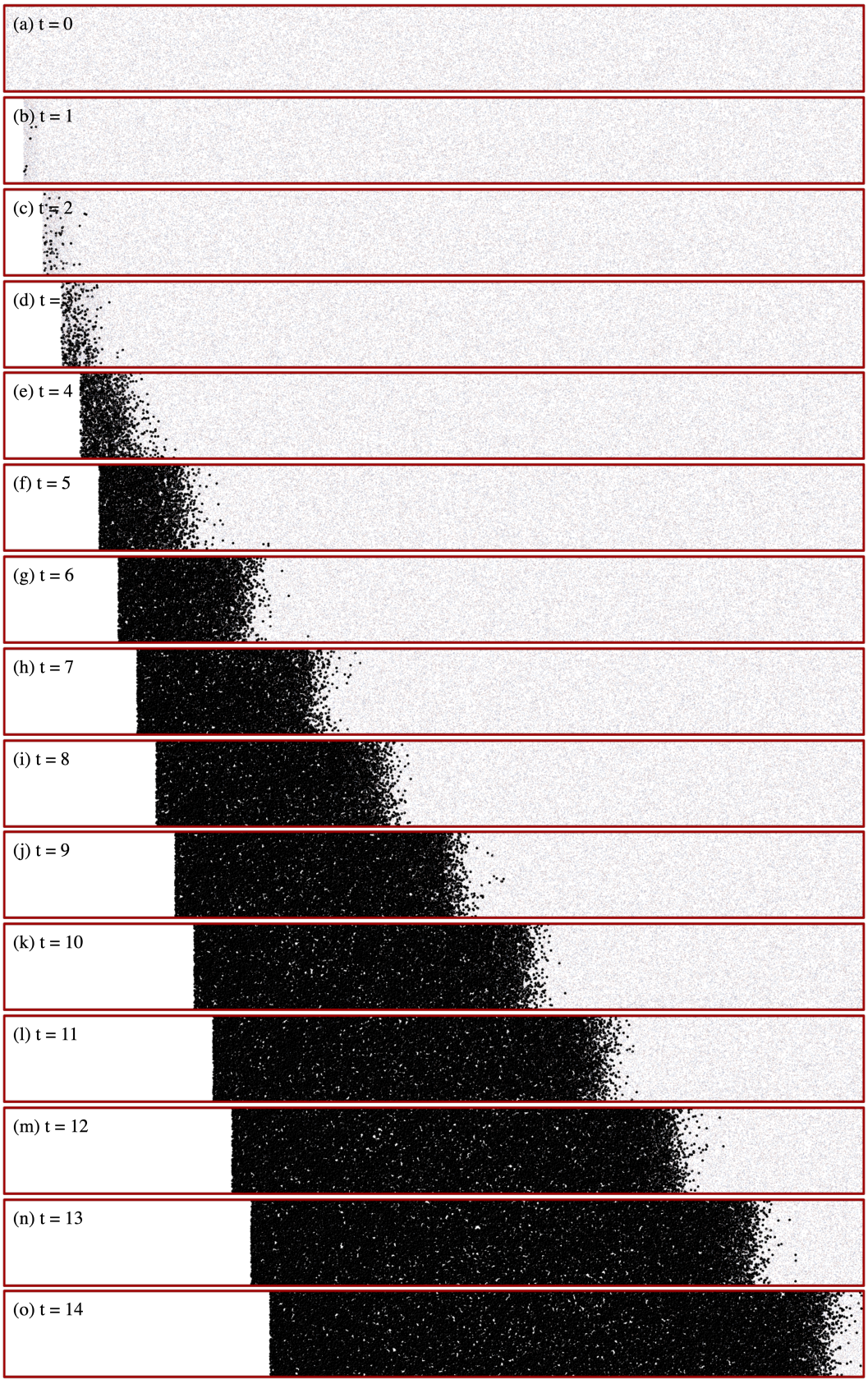

Figure 3.6: Time series snapshot of a sliced three-dimensional box for $\frac{Q}{RT_0} = 40$, $\frac{E_A}{RT_0} = 20$, $\frac{E_A}{RT_s} = 5$ from 0 to 14 mean free time.

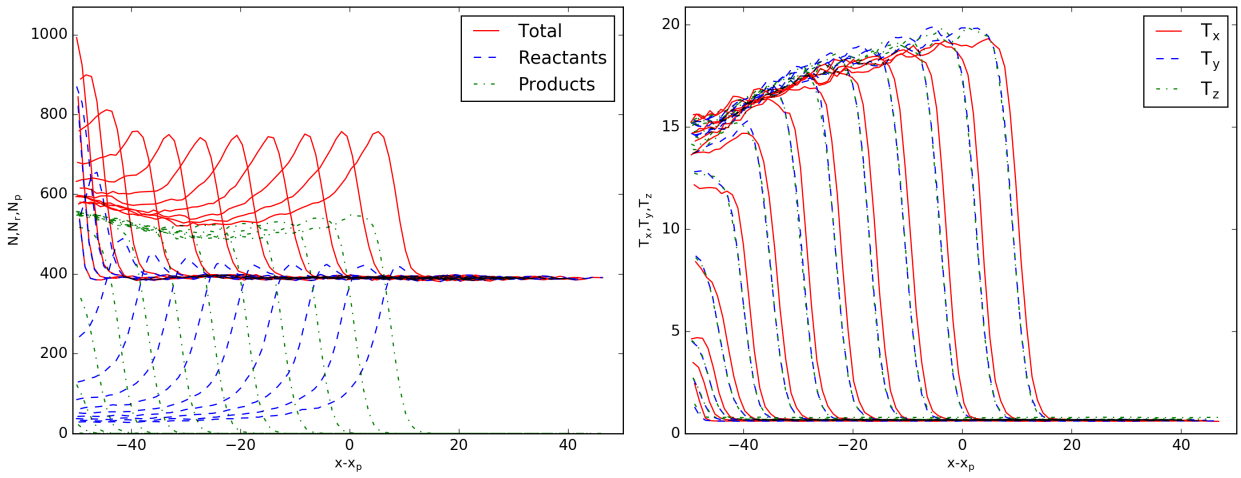

(a) (b)

Figure 3.7: Time evolution of (a) species profile with reactants (dashed blue line), products (dash-dotted green line) and total species (red line) and (b) temperature profile in the piston frame of reference for $\frac{Q}{RT_0} = 40$, $\frac{E_A}{RT_0} = 20$, $\frac{E_A}{RT_s} = 5$.

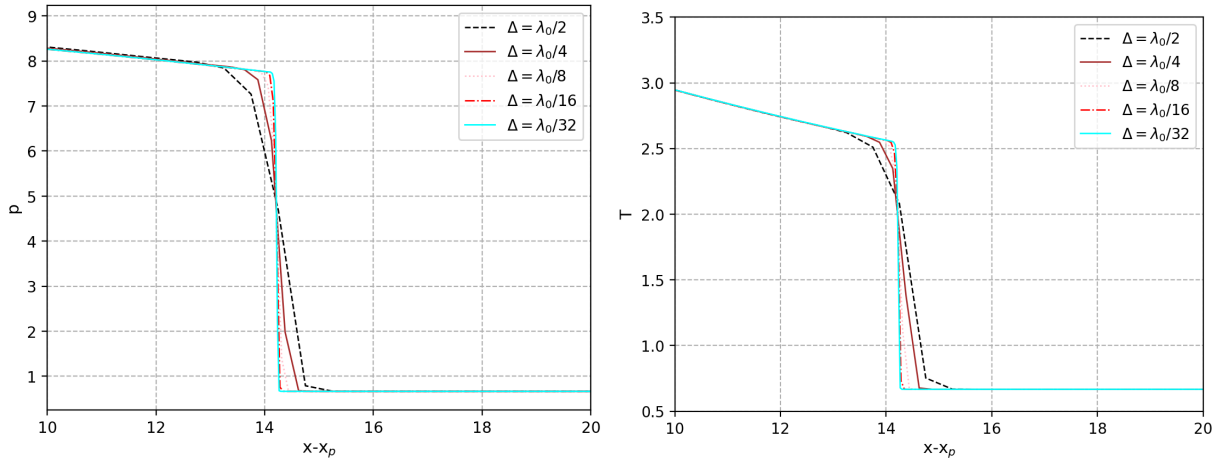

(a) Pressure (b) Temperature

Figure 3.8: Comparison of shock structure for various resolutions for Euler calculations with $\frac{Q}{RT_0} = 20$, $\frac{E_A}{RT_0} = 20$.

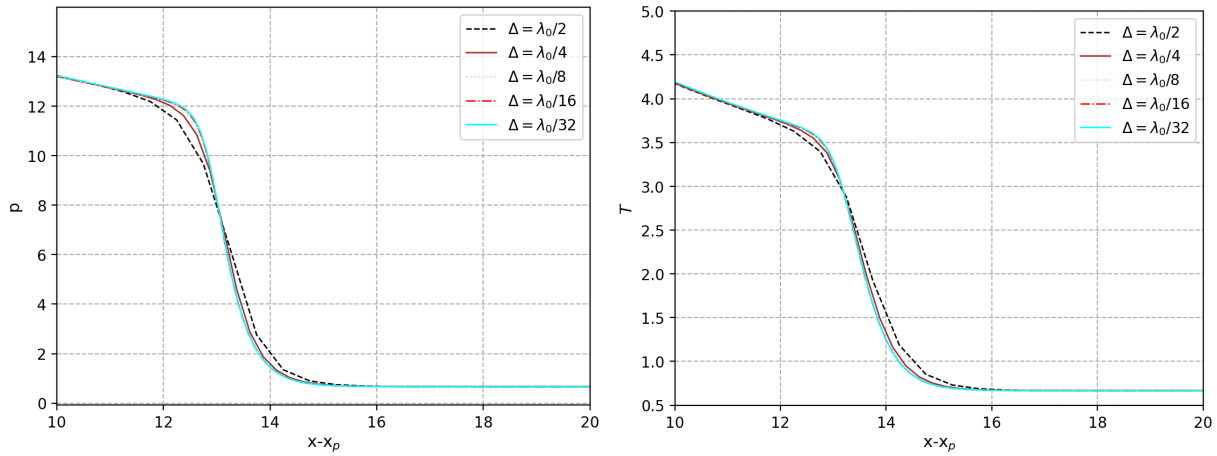

(a) Pressure (b) Temperature

Figure 3.9: Comparison of shock structure for various resolutions for Navier-Stokes calculations with $\frac{Q}{RT_0} = 20$, $\frac{E_A}{RT_0} = 20$.

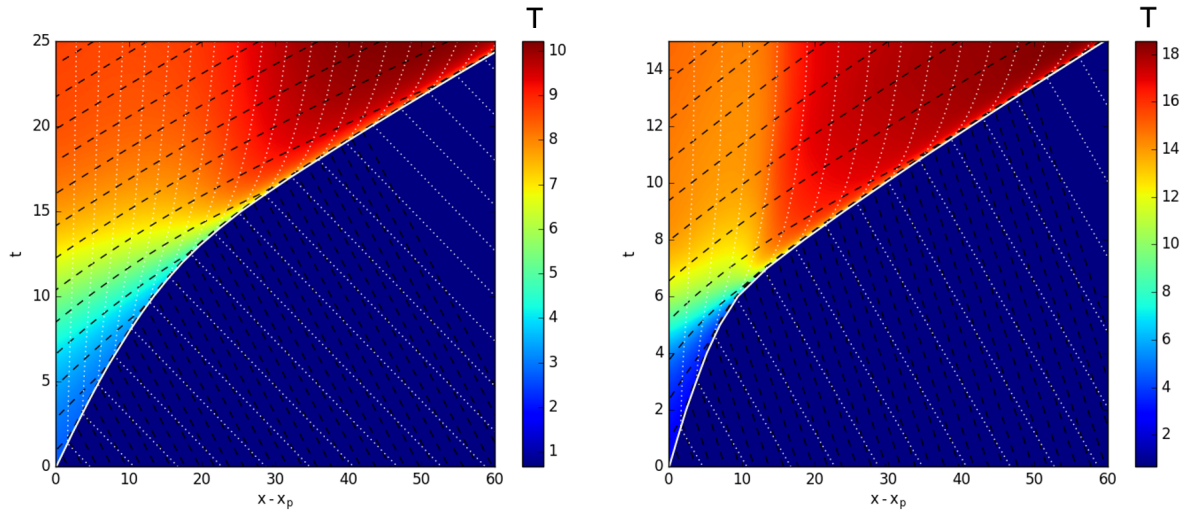

(a) $\frac{Q}{RT_0} = 20$, $\frac{E_A}{RT_0} = 20$ (b) $\frac{Q}{RT_0} = 40$, $\frac{E_A}{RT_0} = 20$

Figure 3.10: Temperature contour on a $x - t$ diagram from Euler calculations for $\frac{E_A}{RT_s} = 5$ with C^+ characteristics (dashed black lines running towards the right) and particle path (dotted white lines running towards the left).

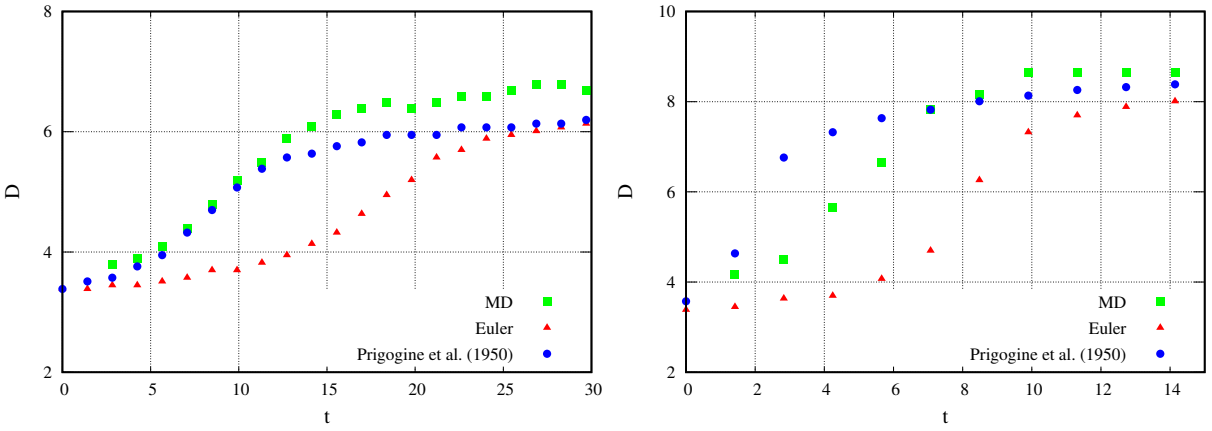

(a) $\frac{Q}{RT_0} = 20$, $\frac{E_A}{RT_0} = 20$ (b) $\frac{Q}{RT_0} = 40$, $\frac{E_A}{RT_0} = 20$

Figure 3.11: Comparison of detonation initiation process from MD with the reaction rates obtained from equilibrium and Prigogine et al. [8] for $\frac{E_A}{RT_s} = 5$.

4 mean free time earlier for the lower and higher heat release cases, respectively. In MD, the transition to detonation occurs approximately twice as fast as predicted by the conventional Euler hydrodynamic model. However, there exist significant discrepancies between the results obtained from the Euler and MD approaches.

Although the traditional approach for modeling detonation waves has been successful in many scenarios, it has limitations when dealing with gases that are not in local thermal equilibrium or when strong pressure gradients are present. To address the non-equilibrium effects caused by the chemistry, the non-equilibrium reaction rate (Eq. (2.15)), ω_M, developed by Prigogine and Mahieu [8], is incorporated into the continuum Euler calculations. The comparison between the results obtained through this approach and MD simulations, as presented in Figs. 3.11a and 3.11b, demonstrates good agreement for lower values of heat release. However, for higher values of heat release, the non-equilibrium corrections introduced by Prigogine and Mahieu appear to overestimate the shock speed, similar to the findings in the 0D calculations.

One can perform a qualitative analysis of the results obtained in Chapter 2 in the context of compressible flow. To gain a better understanding, it is informative to revisit the plot of the natural logarithm of ignition delay versus activation energy, as shown in Figs. 2.8 and 2.9, for the low and high heat release cases discussed in Chapter 2. These figures reveal that the results obtained from molecular dynamics (MD) simulations and those from Prigogine et al. [8] are in good agreement and are situated below the curve of the equilibrium reaction rate for an activation energy of 5, which is the post-shock activation energy considered in this chapter. However, as the activation energy decreases, the difference between the equilibrium and MD results diminishes, and further reducing the activation energy leads to an opposing trend. Comparing these results with the present study, it becomes apparent that the non-equilibrium process initially leads to a faster increase in shock speed, but a slower transition to detonation. This can be attributed to the decrease in post shock activation energy with an increase in shock strength, resulting

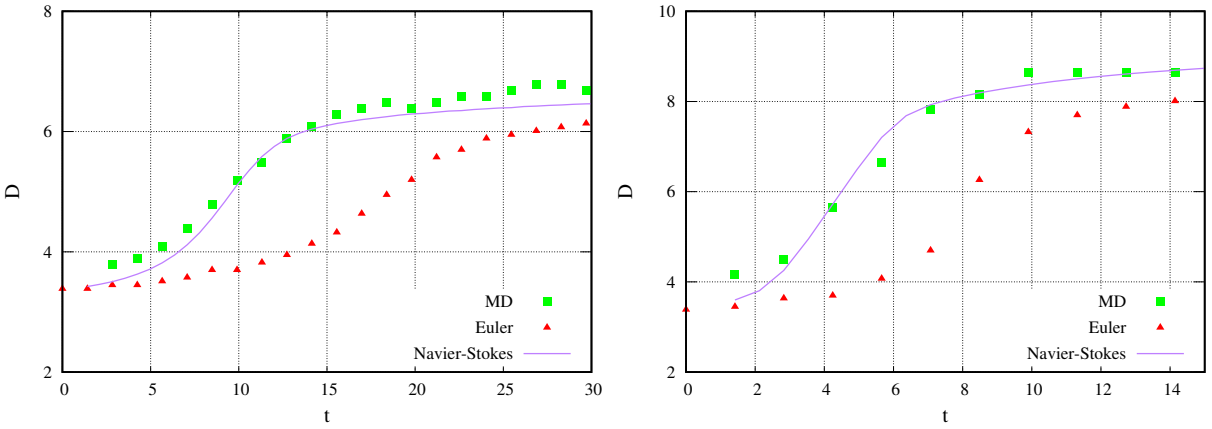

(a) $\frac{Q}{RT_0} = 20$, $\frac{E_A}{RT_0} = 20$ (b) $\frac{Q}{RT_0} = 40$, $\frac{E_A}{RT_0} = 20$

Figure 3.12: Comparison of detonation initiation process from MD with continuum models for $\frac{E_A}{RT_s} = 5$.

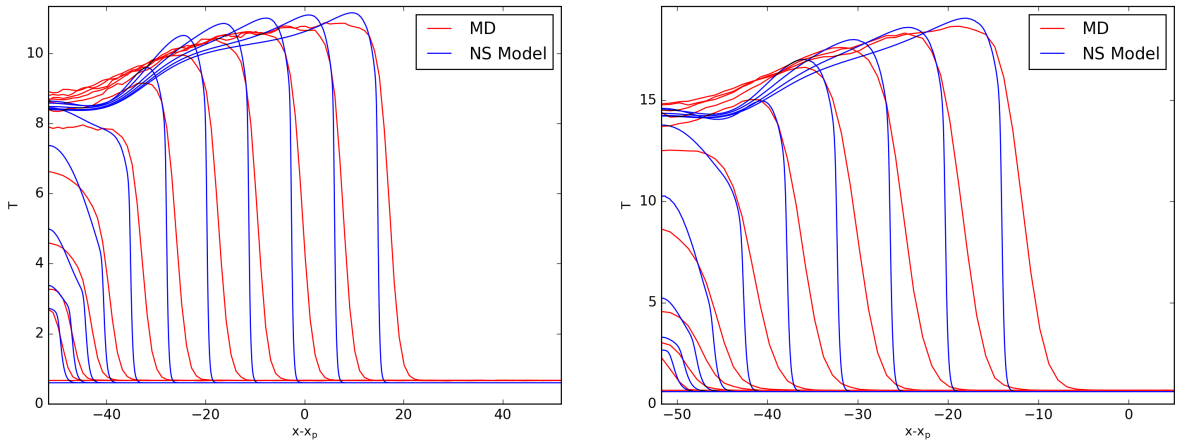

(a) $\frac{Q}{RT_0} = 20$, $\frac{E_A}{RT_0} = 20$ (b) $\frac{Q}{RT_0} = 40$, $\frac{E_A}{RT_0} = 20$

Figure 3.13: Temperature profile comparison of detonation structure from MD with the continuum models during the transition process for $\frac{E_A}{RT_s} = 5$.

in an increase in ignition delay. Therefore, the non-equilibrium reaction rate tend to over predict the MD and equilibrium reaction rate results similar to 0D calculations. Since both models mentioned above are inadequate in capturing the transition process effectively, the Navier-Stokes model is recommended as it incorporates diffusion transport to account for the observed translational non-equilibrium effects in MD.

Finally, a comparison is made between the MD results and the NS model, as shown in Figs. 3.12a and 3.12b. The NS model, which utilizes the transport coefficients from hard sphere gas and the pre-exponential factor similar to the kinetic theory, exhibits good agreement with the MD results for both low and high heat release cases considered. Furthermore, Figs. 3.13a and 3.13b illustrate the comparison of the detonation structure between MD and NS model during the transition process. Thus, the observed fast transition in MD simulations can be attributed to the translational non-equilibrium effects caused by the energy release during the reactions. The magnitude of the energy release governs the kinetic energy of the particles after the reactions, leading to the emergence of finger-like structures ahead of the compression wave that form hotspots, thereby accelerating the ignition process. The diffusive structure produced as a result of these effects leads to the overlap between the reaction zone wave and the shock wave, resulting in the fast transition. Hence, it is evident that the diffusive structure, in conjunction with the energy release, is the underlying cause of the observed behavior.

This finding highlights the necessity of accounting for the transport properties or the diffusive effects when modelling transverse waves to incorporate translational non-equilibrium effects arising from the coupling between pressure wave dynamics and chemistry. Furthermore, by employing the MD model, it becomes possible to evaluate how the presumptions about the individual shock and reaction zone structures in hydrodynamic models of detonations can affect the predictability of detonation wave dynamics, including initiation and failure.

3.7 Concluding Remarks

This chapter investigated the shock-to-detonation transition problem using a reactive dynamics molecular model. The study reveals that conventional Euler hydrodynamic models underestimate the shock amplification rate and the transition to detonation by approximately a factor of two. The findings suggest that shock-induced ignition and the ensuing transition to detonation involve non-equilibrium reactions that overlap with the shock structure and exhibit strong translational non-equilibrium with reactive fingers. Results from the Navier-Stokes model with hard-sphere transport coefficients captures well the acceleration process despite strong indications of non-equilibrium effects. Additionally, the study identifies finger-like structures preceding the compression wave in MD results, which increase with increasing heat release. The fast transition observed in the MD simulations is attributed to the formation of diffusive hotspots ahead of the compression wave, which accelerates the ignition process. Overall, the findings highlight the importance of accounting for transport properties and diffusive effects when modeling transverse waves and incor-

porating translational non-equilibrium effects arising from the coupling between pressure wave dynamics and chemistry when modeling gaseous detonations with fast reactions.

Chapter 4

Viscous Detonation Model for Turbulent Detonations: Structure and Diffraction Dynamics

4.1 Overview and Problem Definition

The present chapter studies the structure of weak viscous detonations introduced by Wood [68]. These detonations have transport coefficients that drive the detonation wave at a speed higher than the Chapman-Jouguet value. The magnitude of the transport coefficients is much larger than the molecular ones. Wood's hyper-viscous detonation model is used as a hydrodynamic model for real turbulent detonations. The effective turbulent diffusion coefficients are adjusted in order to recover the overdrive measured experimentally. The dynamics predicted by this effective hydrodynamic detonation model are then studied for diffracting detonations, to test their usefulness as an engineering coarse-grained description of detonation dynamics.

The diffraction of detonations at abrupt area changes represents a fundamental and pivotal issue in the study of detonation dynamics. This phenomenon arises when a detonation wave, traveling through a confined space, abruptly expands into an unconfined volume. The resulting outcome can be either the quenching of the detonation wave, known as the sub-critical case, or the successful transition and re-establishment of the detonation, which is the super-critical case. The transition point, which is commonly referred to as the critical condition, is of significant interest and has been extensively explored in the scientific literature, as evidenced by studies conducted by Schultz [73] and Thomas et al. [98].

Wood's viscous detonation model is calibrated to recover a global hydrodynamic thickness Δ_{H} of approximately 4λ, based on the research conducted by Edwards et al. [64] and Soloukhin et al. [65]. Numerical simulations of detonation diffraction are then conducted to compare with the recent diffraction experiments of Zangene et al. [9], who determined that the critical channel width for successful diffraction is $W^* \approx \Delta_{\mathrm{H}}$. The dynamics of diffraction are analyzed at several values of W/Δ_{H}.

The present chapter first introduces Wood's model for weak viscous detonations. A novel methodology is provided to obtain the structure numerically by solving a non-linear eigenvalue problem. The double shock structure predicted by Wood's model is tested in separate non-steady hydrodynamic calculations. The investigation then focuses on how Wood's model accounts for detonation diffraction dynamics of cellular detonations in gases.

4.2 Wood's Viscous Detonation Model

A Navier-Stokes description of viscous detonations has been studied by numerous authors [68, 99, 100]. While for weak transport terms, one obtains a structure resembling the ZND structure [101], where the reaction zone does not overlap with the shock, for sufficiently high transport coefficients, the reaction zone overlaps with the shock structure and the detonation speed exceeds the Chapman-Jouguet value. When these detonations are not supported, their structure resembles that of an inert shock with monotonic increase in temperature, speed, pressure and density. To date, the steady structure postulated by Wood [68], sometimes involving a supplementary embedded shock in the structure, has not been verified by non-steady simulations. An exception is the numerical study of Gamezo et al. [69], who observed weak detonations in a study of flame acceleration with enhanced diffusion coefficients to account for turbulence; these authors have not compared their simulations against Wood's theory.

This section is devoted to a brief review of Wood's complex structure, which differs substantially from inviscid theory. A method for obtaining the steady structure of the wave is obtained as a non-linear eigenvalue problem, where given the Mach number of the wave (in excess of the CJ value), the magnitude of the transport coefficients in relation to the reaction rate is found, similar to the procedure for deflagration waves [102, 103]. The details for obtaining the steady traveling solution are provided, and these solutions are verified through non-steady hydrodynamic calculations.

4.2.1 Governing equations

The steady viscous detonation structure can be obtained following the structural arguments presented by Wood [68] by solving the one-dimensional (1D), steady, compressible, reactive Navier-Stokes equations while accounting for the effects of transport coefficients, such as viscosity, heat conduction, and species diffusion. These equations describing the conservation of mass, momentum, and energy, along with species transport, in a reactive flow system are:

$$\frac{\mathrm{d}}{\mathrm{d}\bar{x}}(\bar{\rho}\bar{u}) = 0 \tag{4.1}$$

$$\frac{\mathrm{d}}{\mathrm{d}\bar{x}}\left(\bar{\rho}\bar{u}^2 + \bar{p}\right) = \frac{4}{3}\frac{\mathrm{d}}{\mathrm{d}\bar{x}}\left(\bar{\mu}\frac{\mathrm{d}\bar{u}}{\mathrm{d}\bar{x}}\right) \tag{4.2}$$

$$\frac{\mathrm{d}}{\mathrm{d}\bar{x}}\left(\bar{\rho}(\bar{c}_{\mathrm{P}}\bar{T} + \frac{\bar{u}^2}{2})\bar{u}\right) = \frac{\mathrm{d}}{\mathrm{d}\bar{x}}\left(\bar{k}\frac{\mathrm{d}\bar{T}}{\mathrm{d}\bar{x}}\right) + \frac{4}{3}\frac{\mathrm{d}}{\mathrm{d}\bar{x}}\left(\bar{\mu}\bar{u}\frac{\mathrm{d}\bar{u}}{\mathrm{d}\bar{x}}\right) \tag{4.3}$$

$$\frac{\mathrm{d}}{\mathrm{d}\bar{x}}(\bar{\rho}\bar{u}Y) = \frac{\mathrm{d}}{\mathrm{d}\bar{x}}\left(\bar{\rho}\bar{D}\frac{\mathrm{d}Y}{\mathrm{d}\bar{x}}\right) - \bar{\omega} \tag{4.4}$$

$$\bar{\omega} = \bar{k}_0\bar{\rho}Y\exp\left(-\frac{\bar{E}_{\mathrm{A}}}{\bar{R}\bar{T}}\right) \tag{4.5}$$

The three transport coefficients in this system are $\bar{\mu}$, $\bar{k}$, and $\bar{D}$. They represent the dynamic viscosity, thermal conductivity, and diffusivity, respectively. The symbol $\bar{[]}$ denotes dimensional parameters, and $\bar{c}_{\mathrm{P}}$ is the specific heat.

4.2.2 Non-dimensional parameters

The problem is non-dimensionalized by taking the unburned density $\bar{\rho}_{\mathrm{u}}$ as characteristic density, the sound speed in the unburned gas $\bar{c}_{\mathrm{u}}$ as characteristic speed and

$$\Delta_{\mathrm{H}} = \frac{\bar{k}}{\bar{\rho}_{\mathrm{u}}\bar{c}_{\mathrm{P}}\bar{c}_{\mathrm{u}}} \tag{4.6}$$

as characteristic distance. Note that the latter provides the diffusion length scale dictating the thickness of the weak detonation, as will become evident below. The term "hydrodynamic thickness" is labeled in Wood's viscous detonation model to refer to this length scale.

The non-dimensional variables become:

$$\rho = \frac{\bar{\rho}}{\bar{\rho}_{\mathrm{u}}} \quad T = \frac{\bar{R}\bar{T}}{\bar{c}_{\mathrm{u}}^2} = \frac{1}{\gamma}\frac{\bar{T}}{\bar{T}_{\mathrm{u}}} \quad u = \frac{\bar{u}}{\bar{c}_{\mathrm{u}}} \quad x = \frac{\bar{x}\bar{\rho}_{\mathrm{u}}\bar{c}_{\mathrm{P}}\bar{c}_{\mathrm{u}}}{\bar{k}} \quad \mathrm{Le} = \frac{\bar{k}}{\bar{\rho}\bar{D}\bar{c}_{\mathrm{P}}}$$

$$\mathrm{Pr} = \frac{\bar{\mu}\bar{c}_{\mathrm{P}}}{\bar{k}} \quad Q = \frac{\bar{Q}}{\bar{c}_{\mathrm{u}}^2} = \frac{1}{\gamma}\frac{\bar{Q}}{\bar{R}\bar{T}_{\mathrm{u}}} \quad E_{\mathrm{A}} = \frac{\bar{E}_{\mathrm{A}}}{\bar{c}_{\mathrm{u}}^2} = \frac{1}{\gamma}\frac{\bar{E}_{\mathrm{A}}}{\bar{R}\bar{T}_{\mathrm{u}}} \quad G = \frac{\bar{G}}{\bar{\rho}_{\mathrm{u}}\bar{c}_{\mathrm{u}}}$$

4.2.3 Non-dimensional form of governing equations

With the scaling above, the governing equations in non-dimensional form become:

$$\frac{\mathrm{d}u}{\mathrm{d}x} = \frac{3}{4\mathrm{Pr}}\left(m(u - u_{\mathrm{u}}) + \left(\frac{mT}{u} - T_{\mathrm{u}}\right)\right) \tag{4.7}$$

$$\frac{\mathrm{d}T}{\mathrm{d}x} = m(T - T_\mathrm{u}) + \frac{\gamma - 1}{\gamma}\Bigg(Q(G - mY_\mathrm{u}) - \frac{1}{2}m(u - u_\mathrm{u})^2 + (uT_\mathrm{u} - mT)\Bigg) \tag{4.8}$$

$$\frac{\mathrm{d}G}{\mathrm{d}x} = -\frac{mY\Gamma_0}{u}\exp\left(-\frac{E_\mathrm{A}}{T}\right) \tag{4.9}$$

$$\frac{\mathrm{d}Y}{\mathrm{d}x} = \mathrm{Le}\Big(mY - G\Big) \tag{4.10}$$

where, $m = \rho u$ and $\Gamma_0 = \bar{k}_0\bar{k}/\gamma\bar{p}_\mathrm{u}\bar{c}_\mathrm{P}$, is a function of initial and transport properties of the given mixture only.

The completeness of the above equations is achieved by incorporating boundary conditions at the burnt and unburnt states.

$$\begin{aligned} x \to -\infty &: (u, T, Y, G) = (u_\mathrm{b}, T_\mathrm{b}, Y_\mathrm{b}, G_\mathrm{b}) \\ x \to +\infty &: (u, T, Y, G) = (u_\mathrm{u}, T_\mathrm{u}, Y_\mathrm{u}, G_\mathrm{u}) \end{aligned} \tag{4.11}$$

The subscript "b" and "u" denotes the burnt and unburnt side, respectively. The details of the derivation can be found in Appendix C. In the interest of simplicity, the overbar is excluded throughout the remainder of this chapter.

4.2.4 Boundary conditions

Both the fresh and burnt states are linked by the usual Rankine-Hugoniot jump relations for a detonation propagating at a known Mach number, M_0. The structure of a detonation propagating at an arbitrary Mach number is obtained by solving the governing equations (4.7)-(4.10) with boundary conditions (4.11). In this study, the fresh gas state, mixture properties such as γ, Le, Pr, Q, E_A, and the detonation Mach number M_0 are specified. The unburnt state has a mass fraction Y of 1 for reactant species and 0 for the burnt state, while the reactant mass flux G is M_0 at the unburnt state and 0 at the burnt side. The structure of the detonation is entirely determined once the remaining parameter Γ_0, also known as the burning rate eigenvalue [14], is found. For the type of weak detonations studied, Γ_0 is a non-linear eigenvalue of the system, as a single value simultaneously satisfies the governing equations and boundary conditions. This parameter is identical to the burning rate eigenvalue in deflagration problems [102, 103].

4.2.4.1 Cold boundary difficulty

The cold boundary difficulty in deflagration analyses [103] is also present in the weak detonation problem. When considering the mass flux equation (4.9), the reaction rate is finite at the cold boundary, taken at $x \to +\infty$. Given the finite reaction rate, the gas originating far away from the wave front would evolve to a non-negligible degree of

reaction. The derivative of mass flux does not go to zero until the temperature approaches zero, which is physically unrealistic and mathematically inconvenient.

To address this issue, researchers [99] have introduced a piecewise function called the "ignition temperature approximation". This function represents an elegant and pragmatic way to handle the problem at the cold boundary. Specifically, the function is defined as follows:

$$\frac{\mathrm{d}G}{\mathrm{d}x} = \begin{cases} 0, & T < T_i \\ -\frac{mY\Gamma_0}{u} \exp\left(-\frac{E_\mathrm{A}}{T}\right), & T > T_i \end{cases}$$

1. When the temperature is below the ignition temperature (T_i), the derivative of mass flux is set to zero. This corresponds to the assumption that no chemical reactions can occur at such low temperatures and simplifies the integration of the mass flux equation in this regime.

2. When the temperature is above the ignition temperature, the derivative of mass flux is determined using the Arrhenius relation. This relation expresses the temperature dependence of the reaction rate constant and provides a way to capture the effects of temperature on the chemical kinetics.

In the present study, the ignition temperature is taken to be 1.1 times the fresh gas temperature. The obtained structure is verified to be insensitive to this choice, which agrees with deflagration studies [102, 103]. These conditions serve as stopping criteria for the integration of the mass flux equation, along with the requirement that the mass flux of reactant species, G, equals the initial flux of reactants, M_0. Together, they allow to model reactive systems in a robust and accurate manner, while taking into account the physical and mathematical constraints imposed by the problem.

4.2.4.2 Hot boundary difficulty

The second difficulty lies in the hot boundary state. This is because the hot boundary state is a fixed point in the language of dynamical systems, where the right-hand sides of equations (4.7)-(4.10) vanish. Therefore, integration should be started from a point close to the hot boundary state along a stable trajectory. The difficulty in the burned gases was not addressed by Wood, but only later by Wagner [100], who discussed the linearized problem in terms of its eigenvalues and eigenvector using standard techniques of non-linear ordinary differential equations - see for example the excellent treatment provided by Strogatz [104]. This decomposition is used to numerically solve the structure of Wood's detonation model.

The method requires linearizing the governing equations (4.7)-(4.10) around the hot boundary state using first-order Taylor series expansions:

$$\frac{\mathrm{d}u}{\mathrm{d}x} = \frac{3}{4\mathrm{Pr}}\left(\overbrace{(u-u_\mathrm{b})}^{u'}\left(1-\frac{T_\mathrm{b}}{u_\mathrm{b}^2}\right)+\overbrace{(T-T_\mathrm{b})}^{T'}\frac{1}{u_\mathrm{b}}\right) \tag{4.12}$$

$$\frac{\mathrm{d}T}{\mathrm{d}x} = (G-G_\mathrm{b})\frac{\gamma-1}{\gamma}Q+\frac{(T-T_\mathrm{b})}{\gamma}+(u-u_\mathrm{b})\frac{\gamma-1}{\gamma}\left(\frac{1}{\gamma M_0^2}-(u_\mathrm{b}-1)\right) \tag{4.13}$$

$$\frac{\mathrm{d}G}{\mathrm{d}x} = -(Y-Y_\mathrm{b})\frac{\Gamma_0}{u_\mathrm{b}M_0^2}\exp\left(-\frac{E_\mathrm{A}}{T_\mathrm{b}}\right) \tag{4.14}$$

$$\frac{\mathrm{d}Y}{\mathrm{d}x} = \mathrm{Le}\underbrace{(Y-Y_\mathrm{b})}_{Y'}-\mathrm{Le}\underbrace{(G-G_\mathrm{b})}_{G'} \tag{4.15}$$

The above linearized equations can be represented in matrix form as follows:

$$U' = AU \tag{4.16}$$

$$A = \begin{bmatrix} \frac{3}{4\mathrm{Pr}}\left(1-\frac{T_\mathrm{b}}{u_\mathrm{b}^2}\right) & \frac{3}{4\mathrm{Pr}}\left(\frac{1}{u_\mathrm{b}}\right) & 0 & 0 \\ \frac{\gamma-1}{\gamma}\left(\frac{1}{\gamma M_0^2}-(u_\mathrm{b}-1)\right) & \frac{1}{\gamma} & 0 & \frac{\gamma-1}{\gamma}Q \\ 0 & 0 & \mathrm{Le} & -\mathrm{Le} \\ 0 & 0 & -\frac{\Gamma_0}{u_\mathrm{b}M_0^2}\exp\left(-\frac{E_\mathrm{A}}{T_\mathrm{b}}\right) & 0 \end{bmatrix} \tag{4.17}$$

$$U = \begin{Bmatrix} u' \\ T' \\ Y' \\ G' \end{Bmatrix} \quad U' = \begin{Bmatrix} \frac{\mathrm{d}u'}{\mathrm{d}x} \\ \frac{\mathrm{d}T'}{\mathrm{d}x} \\ \frac{\mathrm{d}Y'}{\mathrm{d}x} \\ \frac{\mathrm{d}G'}{\mathrm{d}x} \end{Bmatrix} \tag{4.18}$$

U and U' represent the column vector of the deviation variables and their derivatives. The matrix A is the Jacobian matrix of the governing equations shown above. The eigenvalues and eigenvectors for this set of linearized equation can be found for this Jacobian matrix. The details regarding the linearization procedure are provided in the Appendix C.

From linear algebra, the general solution for each deviation parameter can be written in terms of the eigenvalues and eigenvectors. For example, the deviation in velocity can be written as:

$$u'(x) = c_1 v_{1,1}\exp^{\lambda_1 x} + c_2 v_{1,2}\exp^{\lambda_2 x} + c_3 v_{1,3}\exp^{\lambda_3 x} + c_4 v_{1,4}\exp^{\lambda_4 x} \tag{4.19}$$

To find the constants in equation (4.19), the boundary conditions are considered. For instance, $x \to -\infty : U \to 0$, the right-hand side in the above equation should be zero. This is true only when all the involving exponentials have finite limits as $x \to -\infty$. The contributions of negative eigenvalues "explode" in this limit. In our system, there is only one positive eigenvalue at the burned state. This means that the phase trajectory approaching the burned gases fixed point is given by the eigenvector of the single eigenvalue that is

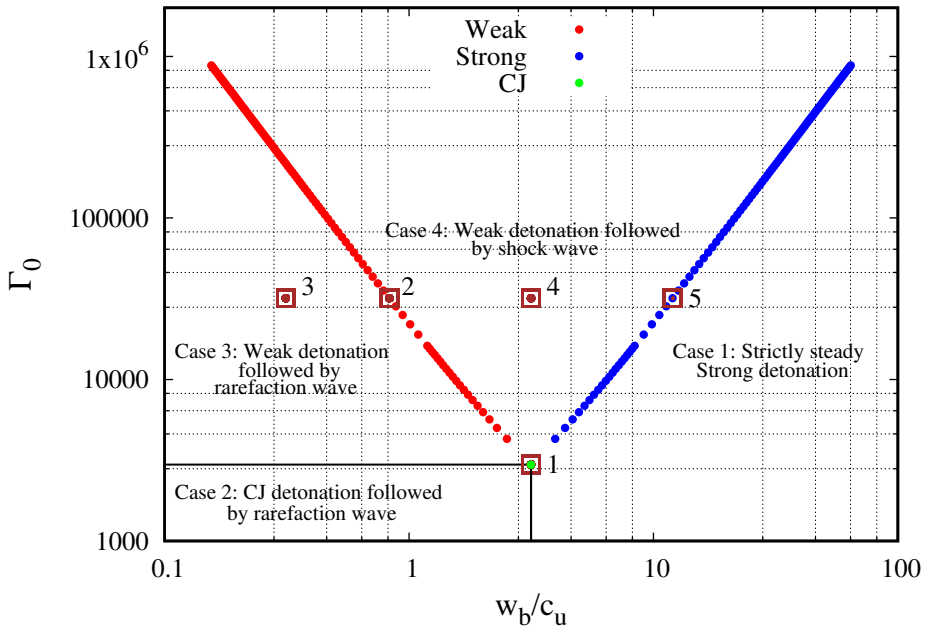

Figure 4.1: The phase diagram of w_b/c_u, Γ_0 for detonation with parameters $\gamma = 1.25$, $E_A/RT_0 = 50$ and $Q/RT_0 = 56$.

positive.

To get the constant c_i, a small deviation is chosen, for example, $u' = 0.0001$ at $x = 0$. Once after finding the constant, the corresponding fluctuation in temperature, mass fraction and the mass flux values at $x = 0$ can also be calculated. And this deviation is added to the hot boundary states which serves as a starting point for the integration.

4.3 The Weak Detonation Structure

The complete determination of the detonation structure, for a given Mach number M_0, and specific set of values, such as $\gamma = 1.25$, $E_A/RT_u = 50$, and $Q/RT_u = 56$, relies on obtaining the burning rate eigenvalue Γ_0. To examine the existence and nature of the flow solutions under fast reactions, where $M_0 \geq M_{CJ}$, a shooting method is utilized, starting from the linearized state near the burnt side as detailed in Section 4.2.4.2. Backward differentiation numerical integration is applied to equations (4.7)-(4.10) with boundary conditions (4.11) for various burning rate eigenvalue, Γ_0, until the integral curve approaches the fresh state as $x \to \infty$. The correct burning rate eigenvalue is then identified through the bisection method. The use of a Lewis number and Prandtl number, both set to 1 and 3/4, respectively, enables the representation of significant mathematical features for detonations.

The following sections provide solutions for steady traveling waves of hyper-viscous detonations. These solutions are illustrated in connection with the solution phase space shown

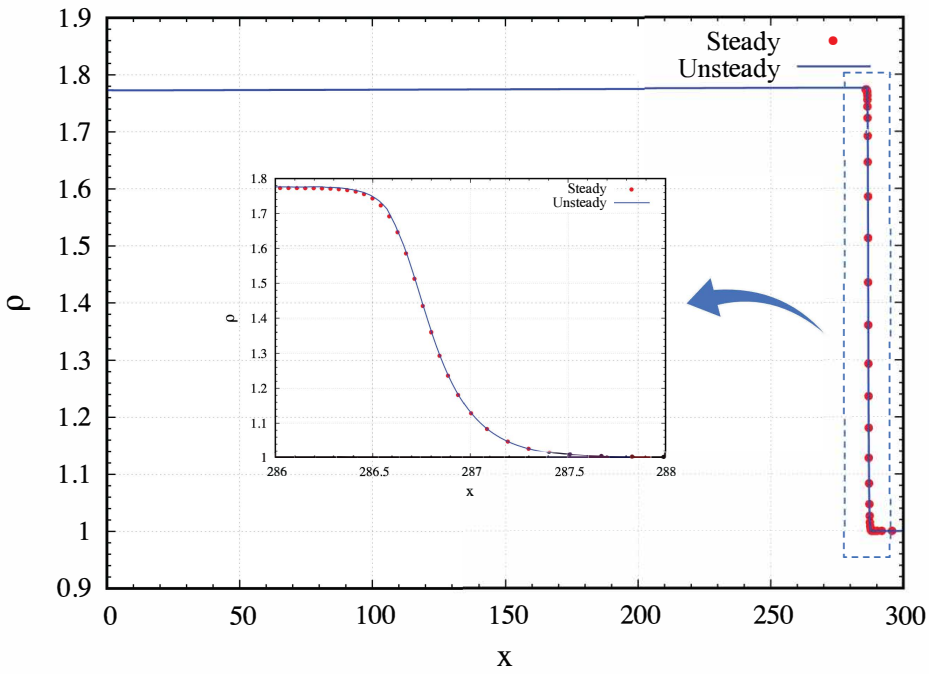

Figure 4.2: Comparison of density profile from steady and unsteady calculations for Point 1: CJ detonation in Fig. 4.1. The inset shows the close view of the detonation structure.

in Figure 4.1, where the piston speed w_P driving the wave and the burning rate eigenvalue Γ_0 are the parameters of interest. Unsteady calculations are also performed using the same technique as in Chapter 3 for Navier-Stokes calculations. The unsteady calculations are initialized with a uniform state and different piston speeds. The calculations are performed in the inertial frame of the steady piston.

4.3.1 Point 1

Point 1 in Fig. 4.1 represents the solution for a steady viscous detonation to propagate at precisely the Chapman-Jouguet speed and obey CJ jump conditions, where the downstream flow is sonic. The critical burning rate eigenvalue is $\Gamma_{CJ} = 2968$. To obtain this solution, the governing equations were linearized near the sonic condition $w_P = w_{CJ}$, solved using eigenvalue decomposition and the shooting method described above. The correct eigenvalue is found using the bisection method until the unburnt state mass flux equals M_{CJ} and the temperature reaches the prescribed ignition temperature. Fig. 4.2 shows the density distribution in this case. The resulting steady viscous detonation structure is monotonic, containing a global reaction zone with overlapping reaction zone and shock, and is plotted alongside the unsteady calculations (Fig. 4.2). The solution is also visualized in the p-v diagram (Fig. 4.7). If $w_P < w_{CJ}$, the detonation structure remains a stable CJ detonation accompanied by rarefaction wave as it expands from w_{CJ} to w_P. This region is identified as Case 2 in the phase space plot.

Note that for the parameter set investigated, the burning rate eigenvalue of $\Gamma_{CJ} = 2968$

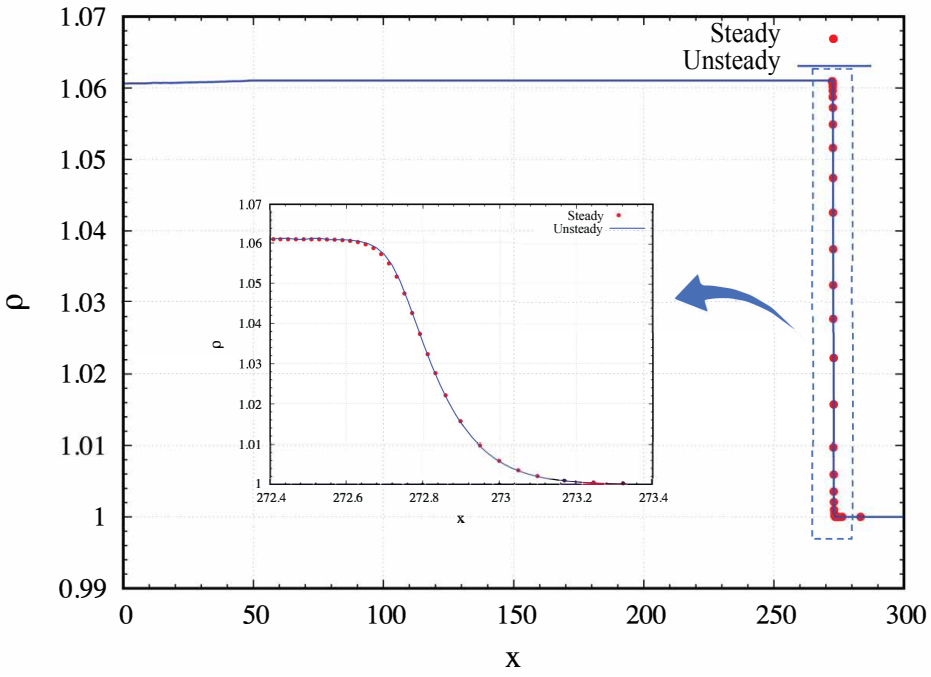

Figure 4.3: Comparison of density profile from steady and unsteady calculations for Point 2: Weak detonation branch in Fig. 4.1. The inset shows the close view of the detonation structure.

is much larger than that obtained for a hard sphere gas where $\Gamma_0 = 3.4$, such as studied in Chapter 3. This illustrates quite unambiguously that Wood's hyper-viscous model applies only for diffusion coefficients at least three orders of magnitude larger than the molecular ones.

4.3.2 Point 2

Waves propagating at speeds larger than the CJ value require larger burning rate eigenvalues than $\Gamma_{\rm CJ}$. The weak detonation's structure and burning rate eigenvalue Γ_0^* (identified as Point 2 in Fig. 4.1) can be obtained through a similar process as described previously, except that the integration starts from the burnt state linearized near the weak detonation state, where $w_{\rm b}^* = w_{\rm P} < w_{\rm CJ}$ and Mach number above $M_{\rm CJ}$. The weak detonation structure displays the same reaction zone and shock coupling as Point 1. Notably, a hydrodynamically stable, strictly steady weak detonation structure exists [68]. A density comparison plot for the weak detonation structure is shown in Fig. 4.3, appearing as a single wave as also illustrated in Fig. 4.7.

4.3.3 Point 3

When the piston speed falls below the weak detonation state ($w_{\rm P} < w_{\rm b}^*$), for $\Gamma_0 = \Gamma_0^*$, the weak detonation wave is accompanied by a rarefaction wave in the reacted products, which

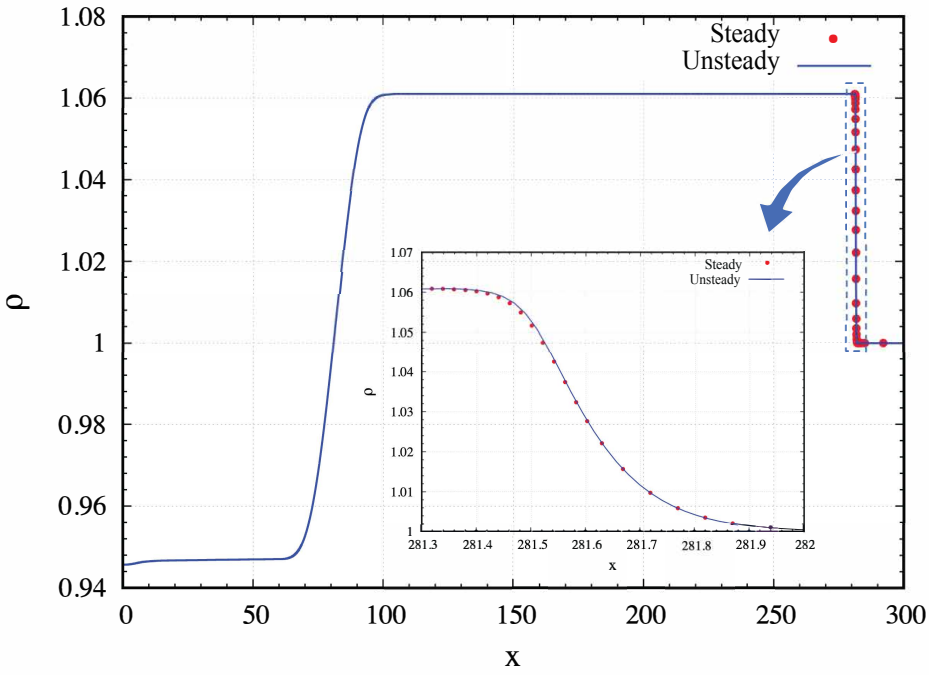

Figure 4.4: Comparison of density profile from steady and unsteady calculations for Point 3: Left of weak detonation branch in Fig. 4.1. The inset shows the close view of the detonation structure.

reduces their mass velocity from w_{b}^{*} to w_{P}. An expansion wave is generated far behind the same weak detonation wave, as confirmed by the non-steady numerical results presented in Fig. 4.4 and the p-v diagram (Fig. 4.7). This regime, Case 3, is characterized by the weak detonation followed by a rarefaction wave in the phase space.

4.3.4 Point 4

A double wave flow pattern of a weak detonation followed by a shock wave in the reacted products appears when the piston velocity w_{P} exceeds w_{b}^{*} and $\Gamma_0 = \Gamma_0^{*}$. Interestingly, the velocity of the following shock wave is slower than that of the weak detonation front, as observed from the slope of the shock wave after the weak detonation state while following the trajectory of point 4 in Fig. 4.7. The unsteady numerical results also show the shock wave far behind the weak detonation (Fig. 4.5). With a fixed value of Γ_0, as w_{P} increases, the velocity of the shock wave changes continuously, and this regime is identified as Case 4 in the phase space. This flow pattern unique to hyper-viscous detonations was first suggested by Wood.

4.3.5 Point 5

A continuous transition from the double wave structure observed at point 4 in the phase space to a strictly strong detonation occurs as the piston velocity w_{P} increases to point 5,

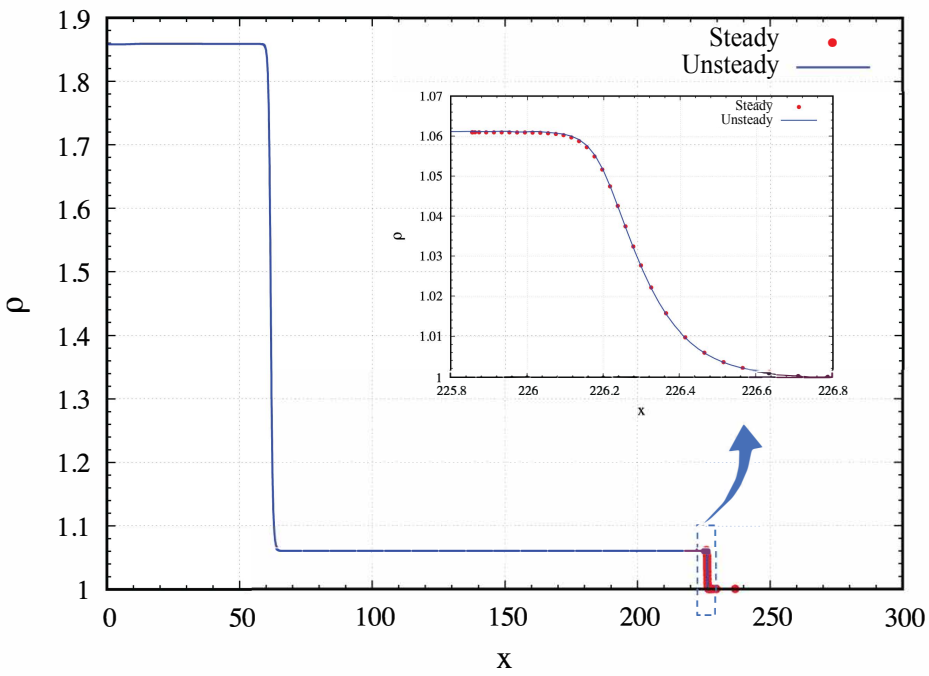

Figure 4.5: Comparison of density profile from steady and unsteady calculations for Point 4: Between strong and weak detonation branch in Fig. 4.1. The inset shows the close view of the detonation structure.

while keeping Γ_0 fixed at Γ_0^*. This is due to the consumption of the same mass flux by both waves, resulting in the shock velocity becoming equal to the weak detonation velocity (as shown in Fig. 4.7). The weak detonation is immediately followed by the shock in this case, as demonstrated in Fig. 4.6. When w_P is further increased for a fixed Γ_0, the two-wave structure becomes unstable because the shock's propagating velocity surpasses that of the weak detonation. This leads to the formation of a single strong detonation wave in the strictly steady strong detonation regime, Case 1.

In summary, for a fixed burning rate eigenvalue Γ_0, the detonation Mach number at any point (2, 3, 4, 5) along the horizontal in Fig. 4.1 is same until the strong detonation branch. This is true for all $\Gamma_0 > \Gamma_{CJ}$, because the state behind a weak detonation is supersonic. In other words, the compression or the rarefaction wave generated by accelerating or decelerating the piston, respectively, will not catch up to the detonation front until the piston speed is equal to that of a strong detonation state. This is well illustrated in p-v diagram (Fig. 4.7) where the end states of the piston travels along the burnt gas inert shock Hugoniot (curved black line) until it coincides with the strong detonation state as shown . This has been verified by performing unsteady calculations at the marked locations along the horizontal line in Fig. 4.1 and the results are compared with steady state ODE's and presented in Figs. 4.2 - 4.6.

A log-log plot of the burning rate eigenvalue obtained from eigen value decomposition technique versus the ratio of detonation speed (D/D_{CJ}) is presented in Fig. 4.8. The figure illustrates the dependence of detonation speed on the pre-exponential factor for different

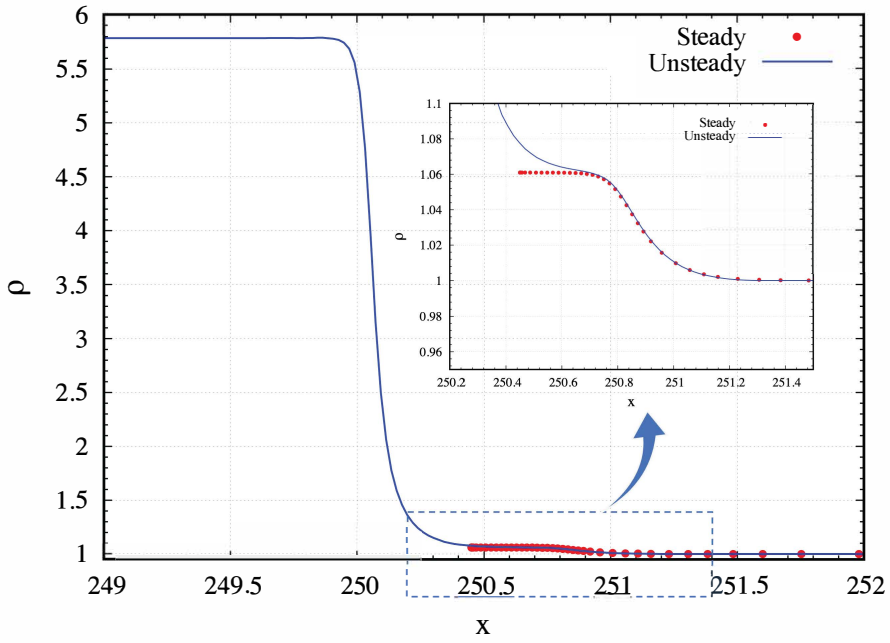

Figure 4.6: Comparison of density profile from steady and unsteady calculations for Point 5: Strong detonation branch in Fig. 4.1. The inset shows the close view of the detonation structure.

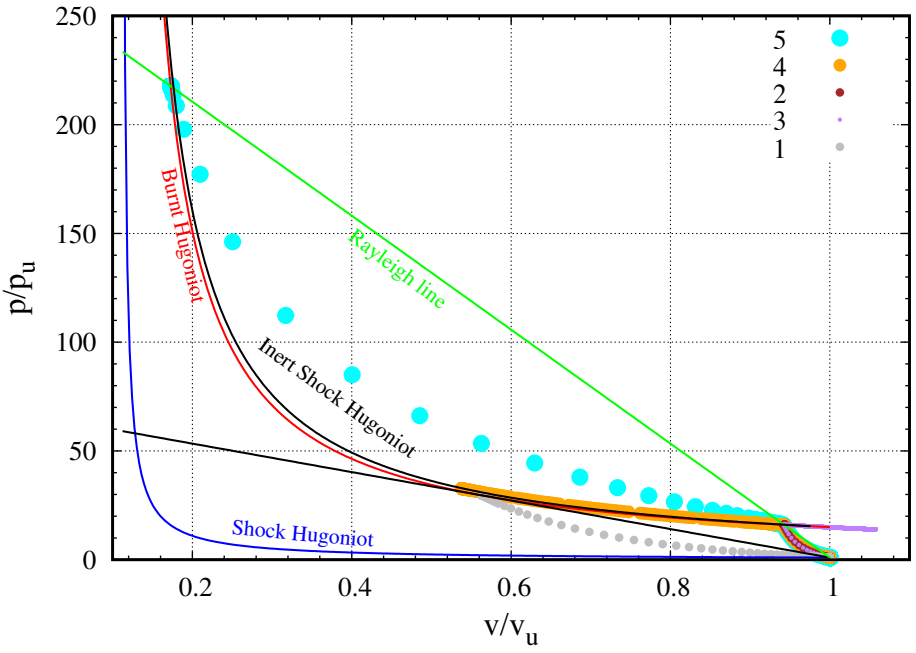

Figure 4.7: p-v diagram for points 1,2,3,4 and 5 in Fig. 4.1.

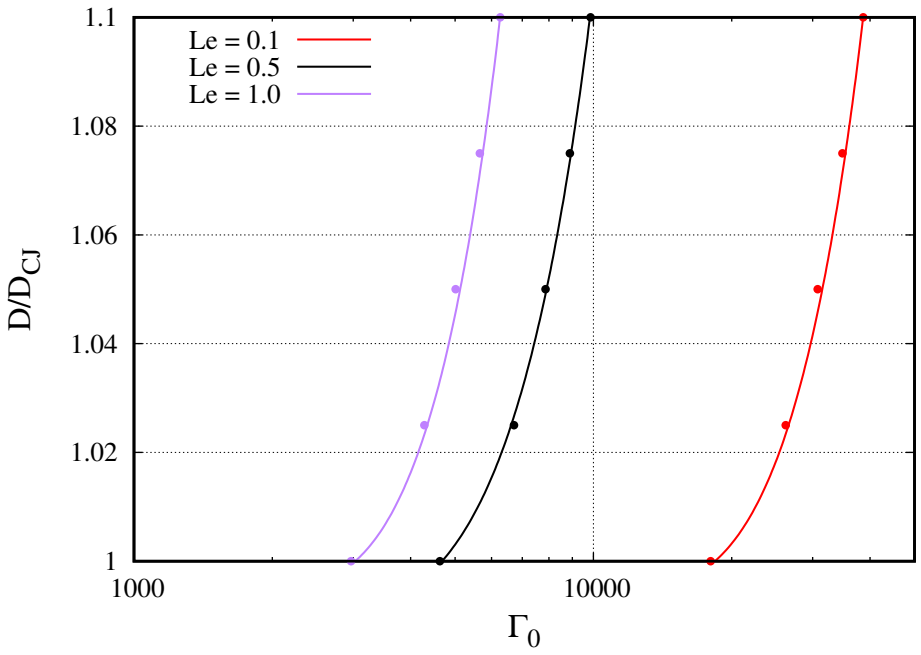

Figure 4.8: Power law fit (solid line) and present results (dots) from steady calculations for Le = 1 (purple), Le = 0.5 (black) and Le = 0.1 (red).

values of Lewis number. The plot reveals a power law relationship between the ratio of detonation speed increase and the pre-exponential factor with an exponent of 2. The figure suggests that an increase in the burning rate eigenvalue, indicating an enhancement of the mixture's effective transport properties, results in a higher detonation speed.

4.4 Calibration of Wood's Viscous Model

As discussed in the introduction, unstable cellular detonations propagate at velocities 1 to 2% higher than Chapman Jouguet values. Wood's hyper-viscous detonation model is therefore very easily calibrated to recover the experimentally observed overdrive.

Inspection of the reaction zone profiles provided above suggest that the hydrodynamic thickness in Wood's model is provided by the diffusive scale given by Eq. (4.6). The kinetic calibration of the model thus involves relating the hydrodynamic thickness of real detonations to that of Wood's model. The global hydrodynamic thickness Δ_H of real cellular detonations are given empirically as approximately 4λ, based on previous studies [64, 65].

Note that a rationalization of the hyper-viscous detonation with very high diffusivity can be obtained by an order of magnitude estimate. Whereas a molecular diffusivity is approximately given by the product of mean molecular speed and mean free path, turbulent diffusivities can be approximated as the product of a mean convective speed and decorrelation length scale of the coherent structures responsible for mixing through Prandtl's

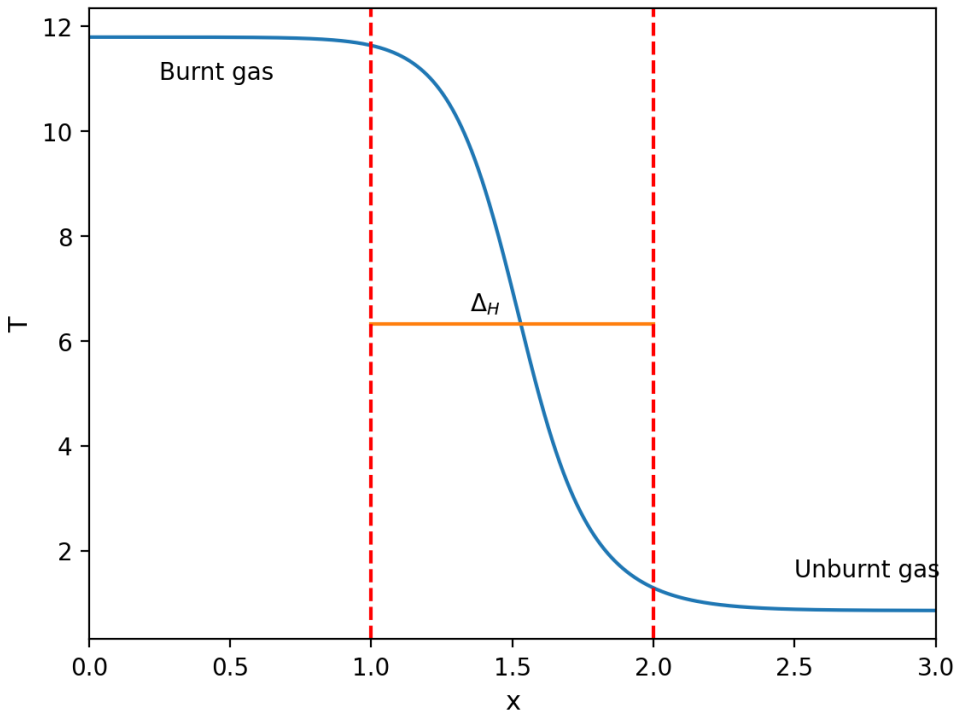

Figure 4.9: 1D steady detonation structure from the viscous model for $\gamma = 1.17$, $Q/RT_{\mathrm{u}} = 70$, and $E_{\mathrm{A}}/RT_{\mathrm{u}} = 22$.

mixing length hypothesis. In cellular detonations the characteristic length scale is the cell size λ while the magnitude of the convective currents is the sound speed in the burned gases c_{b}, yielding a turbulent diffusion coefficient of λc_{b}. Substituting this expression in Eq. (4.6), one obtains

$$\Delta_{\mathrm{H}} \approx \frac{\lambda c_{\mathrm{b}}}{c_{\mathrm{u}}} \approx 3\lambda \tag{4.20}$$

4.5 Dynamics of Diffraction

The present focus shifts to investigating the dynamics of Wood's viscous model for detonation diffraction. The critical diffraction channel width in experiments has been established to be approximately $W^* \approx 3 - 6\lambda$, with the smaller value observed in more irregular mixtures [9, 64, 98]. As a result, the ratio of the critical channel height to the hydrodynamic thickness, W/Δ_{H}, typically falls within the range of 0.75 to 1.5. The diffraction of hyperviscous detonations is studied in this range. In this section, the focus is on the comparison with the recent diffraction experiments reported by Zangene et al. [9] in ethylene-oxygen mixtures who found that the critical channel width for successful diffraction is $W^* \approx \Delta_{\mathrm{H}}$. And accurate data is provided for detonation speeds extrapolated to lossless conditions [66].

Ethylene-oxygen detonation speeds are found to propagate at speeds 1.01 times the CJ values [66], which serves for determining the burning rate eigenvalue, as detailed above. For

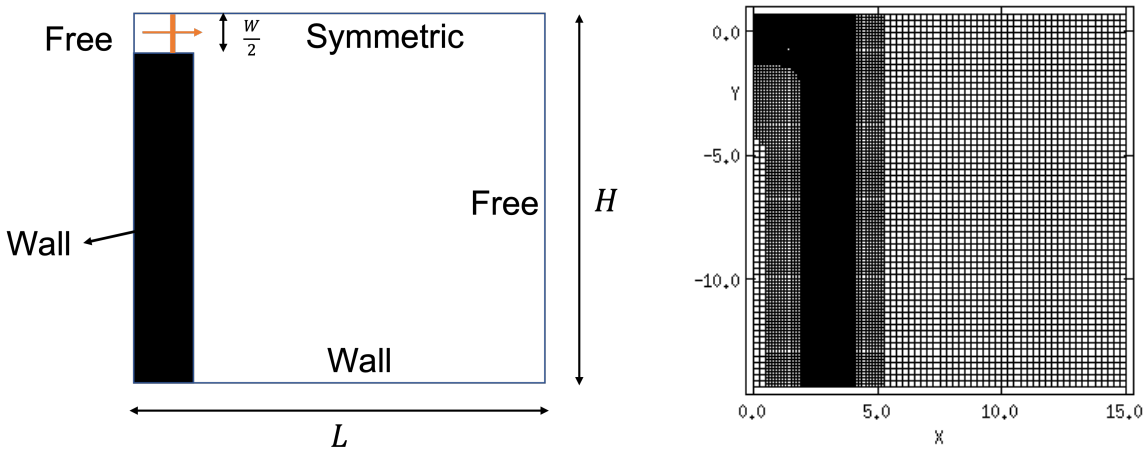

(a) (b)

Figure 4.10: (a) Simulation setup and (b) adaptive mesh refinement with four refinement levels.

this mixture, the isentropic exponent of $\gamma = 1.17$ is estimated for the shocked unburned gas, the Prandtl number is taken as $3/4$, Lewis number as 1, heat release of $Q/RT_u \approx 70$, and the effective activation energy of $E_A/RT_u \approx 22$. These values correspond to the critical mixture properties of an ethylene-oxygen mixture obtained by Zangene et al [9]. The chemical kinetic software Cantera [105] was used to evaluate these properties as explained elsewhere [13]. For this parameter set, the burning rate eigenvalue is $\Gamma_0 = 350$. The steady viscous detonation profile calibrated for overdrive is shown in Fig. 4.9. Note again that the viscous hydrodynamic thickness given by Eq. (4.6) provides an adequate estimate.

4.5.1 Numerical implementation

For numerical computations of the diffraction problem, the same finite-volume computational package, *MG*, utilized in Chapter 3 was used. The steady detonation structure, calibrated from Wood's viscous model using the parameters mentioned in Section 4.5, was initialized in the 2D propagating channel. The left and right boundaries were set to zero gradient boundary conditions, the top boundary to symmetry, and the bottom boundary to wall with slip boundary conditions. The simulation setup is illustrated in Fig. 4.10a.

To enhance the solution's accuracy near discontinuities, an adaptive mesh refinement technique was employed. The mesh was refined around regions with density gradients, internal boundaries, and behind the shocks. The computational domain is discretized using a Cartesian grid, where there are four grid points per unit length on the base grid.

A resolution study (Fig. 4.11) was performed to determine the necessary simulation resolution. Interestingly, raising the resolution from $\lambda_0/16$ to $\lambda_0/64$ had no effect on the solution profile. Unless otherwise stated, four levels of mesh refinement were used, with the number of grid points doubling in each direction at each level (see Fig. 4.10b); thus,

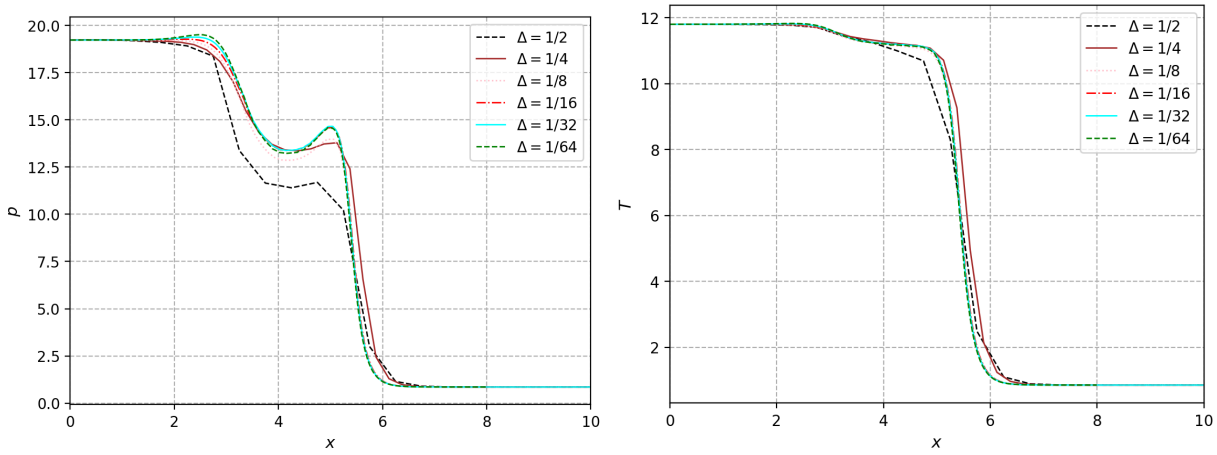

(a) Pressure

(b) Temperature

Figure 4.11: Comparison of detonation structure for various resolutions for detonation diffraction around the corner

the most refined grid spacing was 2^{-5}.

4.5.2 Results and discussion

For the purpose of validation and comparison with existing experimental data, properties along the symmetry axis versus distance are selected for the remainder of the study. To simulate the behavior of the system under varying conditions, numerical experiments are conducted by varying W/Δ_{H} between 0.1 and 5 and the results are plotted (see Figs. 4.12 -4.15).

When the height of the slot surpasses the hydrodynamic thickness ($W/\Delta_{\mathrm{H}} > 1$), the detonation maintains a steady velocity and the shock-reaction zone coupling remains strong, as illustrated in Fig. 4.12. As the slot height approaches the hydrodynamic thickness ($W/\Delta_{\mathrm{H}} = 1$), the detonation slows down more markedly due to the more substantial drop in the speed and pressure due to the sudden area enlargement (refer Fig. 4.13). In this scenario, the reaction wave decelerates to approximately 90% of the Chapman-Jouguet (CJ) speed before re-amplifying again.

Further reduction in W/Δ_{H} results in a more substantial decrease in pressure and speed, since the time scale of reactions becomes progressively longer compared to the expansion time scale. Figures 4.14 and 4.15 show the pressure and speed evolution when $W/\Delta_{\mathrm{H}} = 0.5$ and $W/\Delta_{\mathrm{H}} = 0.1$, respectively.

Figure 4.16 shows a summary of the wave speed evolution established for different W/Δ_{H}. Also shown are the experimental measurements of wave speed in the critical regime of diffraction measured by Zangene et al. [9]. Their data uses a hydrodynamic time

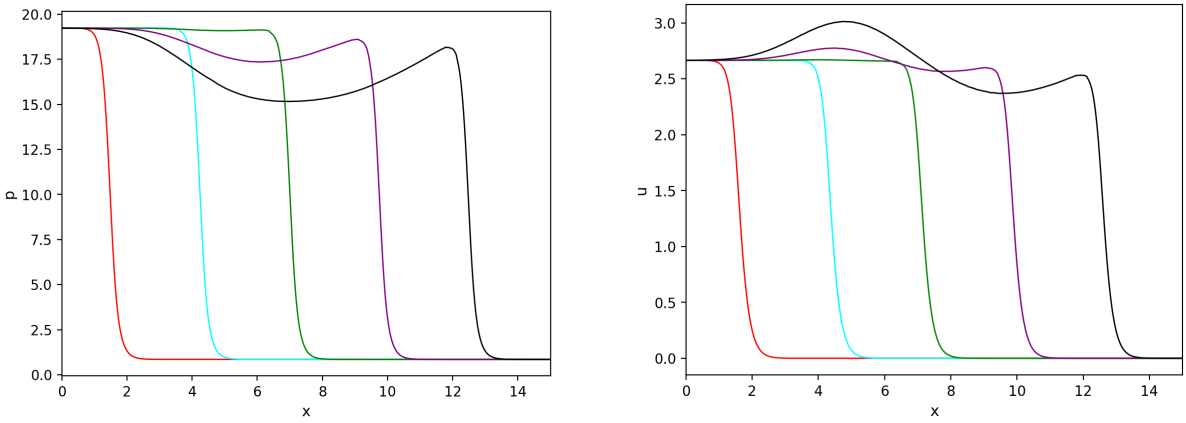

(a) (b)

Figure 4.12: Time evolution of (a) pressure and (b) velocity profile along the axis of symmetry for $W/\Delta_{\mathrm{H}} = 5$.

of

$$t_{\mathrm{H}} = \frac{\Delta_{\mathrm{H}}}{c_{\mathrm{u}}} \approx \frac{4\lambda}{c_{\mathrm{u}}} \tag{4.21}$$

and corresponds to a diffraction condition of $W/\Delta_{\mathrm{H}} \approx 1$. The model with $W/\Delta_{\mathrm{H}} \approx 0.5$ captures very well the speed evolution. The conclusion that can be reached is that a hydrodynamic viscous model captures well the overall dynamics of diffraction with the appropriate length scales within a factor of 2 of calibration for the hydrodynamic thickness.

Nevertheless, it is evident that the viscous model does not have a distinct failure cutoff. A detonation wave is always re-established on a time scale of 1 hydrodynamic time, irrespective of channel width W/Δ_{H}. This deficiency stems from the assumption of a constant nominal burning rate eigenvalue, tuned to represent the intense convective mixing in detonations. In reality, the diffraction of a detonation wave brings about a disintegration of the coherent cellular structure of detonations. This fundamental non-linearity is absent in the present model. An elegant approach to address this challenge would involve incorporating a numerical switch that deactivates the reactions when the velocity falls below a specific threshold, as observed in experiments for sub-critical detonations.

An interesting aspect of the current model is that it permits to propagate detonations with a reaction zone structure much larger than real ones. The hydrodynamic thickness of the viscous model is much larger than the scales of the turbulent deflagration models by several orders of magnitude. It therefore shows great promise for engineering purposes for numerical predictions of detonation dynamics on much coarser grids than required for direct simulation of the turbulent structures.

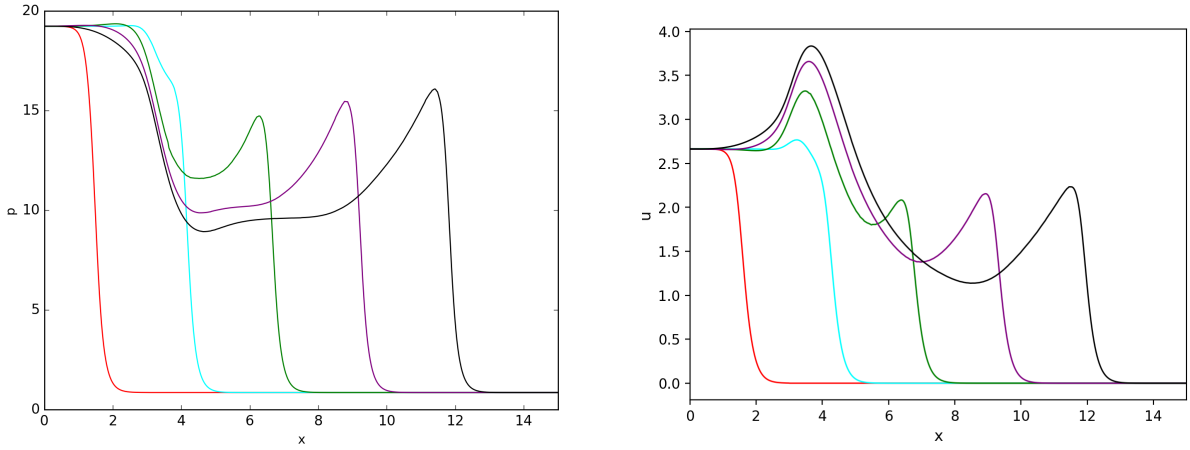

(a) (b)

Figure 4.13: Time evolution of (a) pressure and (b) velocity profile along the axis of symmetry for $W/\Delta_{\mathrm{H}} = 1$.

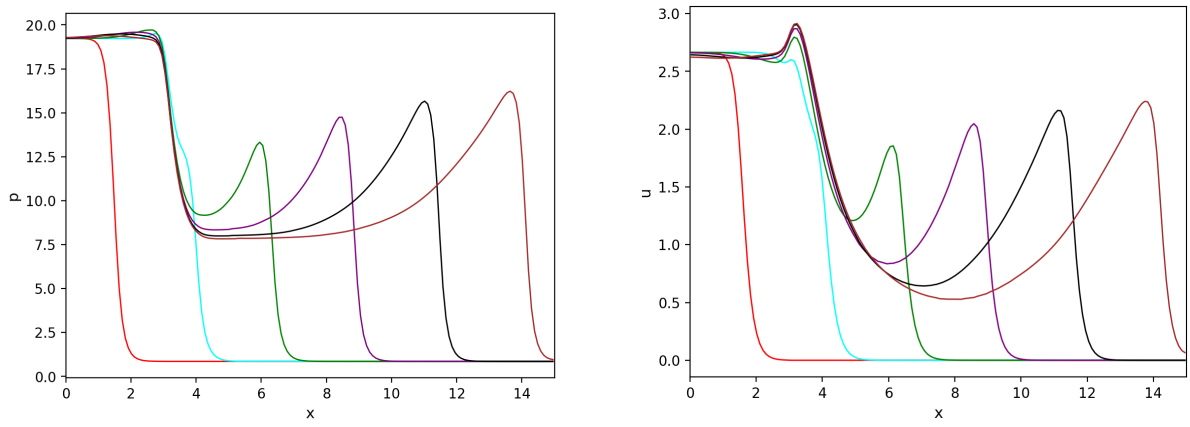

(a) (b)

Figure 4.14: Time evolution of (a) pressure and (b) velocity profile along the axis of symmetry for $W/\Delta_{\mathrm{H}} = 0.5$.

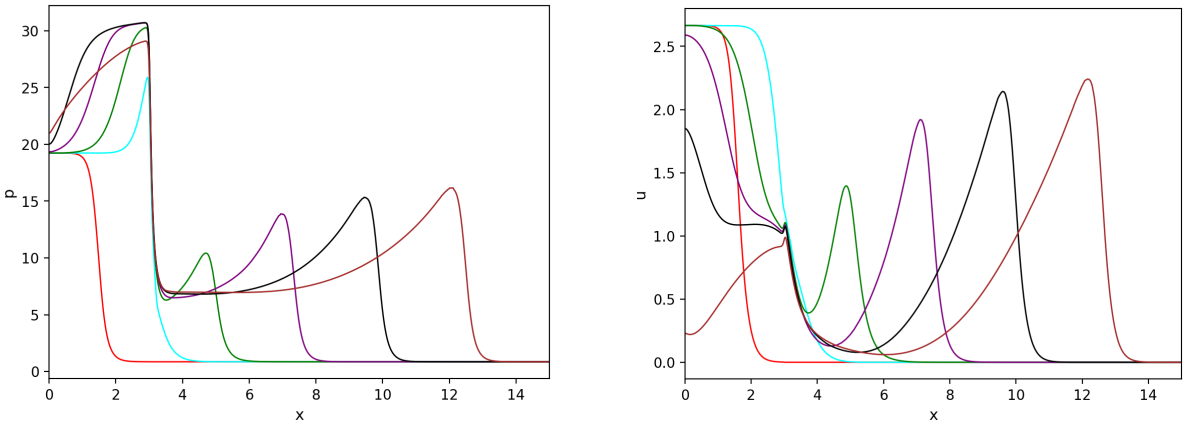

(a) (b)

Figure 4.15: Time evolution of (a) pressure and (b) velocity profile along the axis of symmetry for $W/\Delta_{\mathrm{H}} = 0.1$.

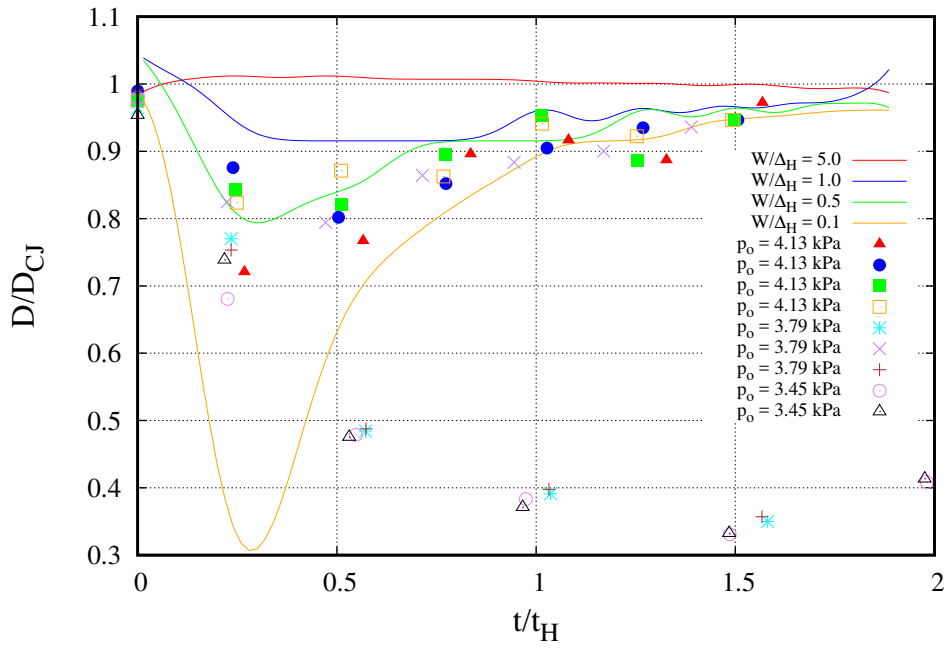

Figure 4.16: The temporal variation of shock speed along the symmetry axis. The solid line represents the outcomes obtained from the present model for distinct values of slot height (W), while the data points signify the series of experimental results obtained for various initial pressures. (Data courtesy of Farzane Zangene, see also [9]).

4.6 Summary

This chapter provided an overview of Wood's theory for hyper-viscous detonations and developed a method to obtain the structure and calibrate it for predictive capabilities of cellular detonation dynamics. The model was found to provide a satisfactory prediction of detonation attenuation and reformation during diffraction, comparing favorably to experiment. This suggests that the premise of a hyper-viscous model for turbulent detonations shows promise for further development. Nevertheless, the model does not predict complete extinction. Further refinement is required for modeling how the strong magnitude of turbulent diffusivity depends on the disintegration of the cellular structure of detonations during diffraction and similar phenomena.

Chapter 5

Conclusions and Recommendations

In this thesis, the role of translational non-equilibrium on the detonation was investigated and addressed numerically at the microscopic and macroscopic levels. The current chapter summarizes the findings from this study and draws conclusions. Final remarks are given on any recommendations that should be considered in the future.

5.1 Concluding Remarks

The study on thermal ignition reveals the existence of two non-equilibrium regimes of ignition. At high temperatures, the ignition delay is longer than predicted by standard kinetic theory assuming local equilibrium, indicating the importance of considering non-equilibrium effects in kinetic predictions. Although the trend was captured by Prigogine and Xhrouet qualitatively, the perturbation model failed at this extreme, as the perturbation assumes slow reactions in the limit of high activation energy. On the other hand, at low temperatures, especially for high heat release, the ignition delay is shorter than predicted by standard kinetic theory. The perturbation scheme of Prigogine and Mahieu that includes the effect of energy release in the perturbation of the distribution function accurately captures the effect. However, the perturbation model used in the study fails at this extreme as it assumes slow reactions in the limit of high activation energy. Consideration of the auto-ignition problem in hydrogen-oxygen at low temperatures in the first part of the thesis suggests that non-equilibrium effects involving energy release can be expected in the auto-catalytic loops of H_2O_2 and HO_2 through local sequences of high energy release followed by high activation reaction of these two species. The hard sphere model's applicability to real reacting systems should be approached with caution, as the model neglects quantum-governed electron cloud interactions and fails to consider factors like the steric effect. These considerations may reduce collision correlations and potentially impact the validity of molecular chaos.

The study of the shock-to-detonation transition problem using a simple reactive dynamics molecular model demonstrates that the shock amplification rate and the transition to detonation occur about twice as fast as for conventional Euler hydrodynamic models.

Molecular dynamic simulations indicate that finger-like structures driven by longitudinal non-equilibrium run ahead of the bulk shock structure. This phenomenon appears to be stronger for more energetic systems. The fast transition observed in the MD simulations was attributed to the formation of hot spots ahead of the compression wave, which accelerated the ignition process. The findings have significant implications for modeling gaseous detonations with fast reactions, where pressure wave dynamics and reactivity in the detonation structure are more strongly coupled than previously predicted by Euler models. Furthermore, these results emphasize the need to account for transport properties and diffusive effects when modeling transverse waves and incorporate translational non-equilibrium effects arising from the coupling between pressure wave dynamics and chemistry. Surprisingly, however, a Navier-Stokes description using hard-sphere transport coefficients captures satisfactorily the acceleration process, despite strong indications of non-equilibrium effects.

The present work also suggested a model for the 3D hydrodynamic structure of cellular detonations consisting of Wood's hyper-viscous detonation structure. The model uses an artificially high turbulent diffusion coefficient to account for turbulent convection in the hydrodynamic structure of detonations. The model calibration requires the experimentally determined hydrodynamic thickness and detonation speed excess with respect to the equilibrium Chapman-Jouguet theory. The study shows that Wood's model predicts weak detonations with overlapping reaction zone and shock structure. Comparison with experiment suggest that turbulent diffusivities in detonations are larger than laminar ones by two to three orders of magnitude. The dynamics of Wood's viscous model was found to capture correctly the time scales of detonation attenuation and reformation in diffraction experiments. However, the model does not predict complete extinction. This finding suggests that the hyper-viscous model for turbulent detonations shows promise for further development provided the link between turbulent diffusivity and cellular structure modification is incorporated.

5.2 Contributions to Original Knowledge

The thesis extends the earlier 2D work of Sirmas to 3D for a more realistic understanding of the role of translational non-equilibrium on ignition and validates Prigogine's kinetic theory model for reaction rate corrections. The study highlights the necessity of incorporating non-equilibrium effects in kinetic predictions, particularly for systems where the kinetics are calibrated experimentally in nearly isothermal conditions. It also shows that no existing perturbation scheme provides a uniformly valid approximation. This indicates the need for empirical correction factors to existing reaction rates based on molecular dynamic results, as provided in the current thesis.

This study sheds light on the shock-to-detonation transition problem by revealing that conventional hydrodynamic models underestimate the transition rate. In contrast, the Navier-Stokes model with hard-sphere transport coefficients accurately predicts the acceleration process, despite strong indications of non-equilibrium effects. The study emphasizes the importance of accounting for transport properties, diffusive effects, and non-equilibrium

effects when modeling transverse waves, and provides insights into the formation of diffusive hotspots and their role in accelerating the ignition process.

The success of the 1D hyper-viscous model in predicting the dynamics of turbulent detonations sheds light on the connection between large-scale physics and small-scale dynamics. It is anticipated that the model may also be used as an engineering computational tool to predict large-scale problems on much coarser grids at a lower computational cost. The hydrodynamic thickness of the model is several orders of magnitude larger than the scales of turbulent deflagrations, making it an attractive option for numerical predictions of detonation dynamics on much coarser grids than those required for direct simulation of turbulent structures.

5.3 Recommendations

The thesis presents straightforward models for investigating translational non-equilibrium effects in detonations. However, to gain deeper insights or more accurately mimic physical systems, further improvements should be considered.

From a chemical reaction kinetics perspective, hydrocarbon mixtures typically involve chain-branching and proceed through various stages of reactions. The applicability of the hard sphere model to real reacting systems may benefit from cautious consideration, as quantum-governed electron cloud interactions are not accounted for, and factors such as the steric effect remain unaddressed. These aspects could lead to potential reductions in collision correlations and could have implications for the validity of molecular chaos. To better address real chemical systems, incorporating a more realistic chemistry model could expand the scope of the present study. The study proposes that future research should focus on multiple reactions, such as the auto-catalytic H_2O_2 loop, which has also been found to be responsible for auto-ignition in hydrocarbons.

The investigation of the shock-to-detonation transition problem through a reactive dynamics molecular model reveals a crucial insight: conventional Euler hydrodynamic models fall short in capturing the shock amplification rate and the transition to detonation. To further expand the study, exploring different limits, such as determining the activation energy at which diffusion effects become insignificant, could yield valuable results. Moreover, this exploration could pave the way for developing more precise models applicable to a broad range of thermal ignition problems. Furthermore, probing the impact of reactant composition, temperature, and pressure on the model's accuracy would enable optimization for real-world applications, such as combustion engines.

To advance the understanding of detonation phenomena, it is essential to investigate the performance of the 1D viscous model in detonations that are highly unstable. Under such circumstances, non-steady effects play a more dominant role, and the turbulent structure of the reaction zone provides a mechanism for enhancing the ignition process. Thus, future research should focus on modeling how the strong magnitude of turbulent diffusivity depends on the disintegration of the cellular structure of detonations during diffraction and similar phenomena.

APPENDICES

Appendix A

Equilibrium Reaction Rate

A.1 Reaction Rate in 3D

The expression for reaction rate for reacting collisions is given by,

Rate of reacting collisions	= Rate of collisions	× Fraction of collisions that involve sufficient energy	× Fraction of sufficiently energetic collisions that actually result in reaction

The first term on the RHS is the bimolecular collision term. The second term, is the activation or energy factor and the third term is the steric factor, is defined as the experimental value of rate constant and the one predicted by collision theory. Steric factor is unity in this study.

The reaction rate for the present model in 3D can be written as

$$-\frac{\mathrm{d}\bar{n}_\mathrm{A}}{\mathrm{d}\bar{t}} = -\frac{\mathrm{d}\bar{n}_\mathrm{B}}{\mathrm{d}\bar{t}} = \frac{1}{2}\frac{\mathrm{d}\bar{n}_\mathrm{C}}{\mathrm{d}\bar{t}} = \underbrace{\bar{n}_\mathrm{A}\bar{n}_\mathrm{B}\bar{d}_\mathrm{AB}^2\left(\frac{8\pi\bar{k}_\mathrm{B}\bar{T}}{\mu_\mathrm{AB}}\right)^{1/2}}_{\text{rate of collisions}} \underbrace{\exp\left(-\frac{\mu_\mathrm{AB}\bar{g}_\mathrm{o}^2}{2\bar{k}_\mathrm{B}\bar{T}}\right)}_{\text{fraction of energetic collision}} \tag{A.1}$$

$$\bar{e}_\mathrm{A} = \frac{1}{4}\bar{m}\bar{g}_0^2$$
$$\mu_\mathrm{AB} = \frac{\bar{m}_\mathrm{A}\bar{m}_\mathrm{B}}{\bar{m}_\mathrm{A}+\bar{m}_\mathrm{B}} = \frac{\bar{m}}{2} \qquad \because \bar{m}_\mathrm{A} = \bar{m}_\mathrm{B} = \bar{m}$$

where, $\bar{g}_0$ and $\bar{e}_\mathrm{A}$ are the relative velocity and activation energy per unit mole, respectively. The number density $\bar{n}$ can be converted to mass fraction with

$$\bar{n}_i = \frac{Y_i\bar{\rho}N}{\bar{W}_i} = \frac{Y_i\bar{\rho}}{\bar{m}}$$

where, $\bar{W}_i = N\bar{m}$ - is the molecular weight of particle i, N - is the number of particles, $\bar{m}$

- is the mass of the particle i

Applying the above simplifications in equation (A.1) gives

$$\frac{1}{2}\frac{\mathrm{d}Y_{\mathrm{C}}\frac{\bar{\rho}}{\bar{m}}}{\mathrm{d}\bar{t}} = \frac{Y_{\mathrm{A}}\bar{\rho}}{\bar{m}}\frac{Y_{\mathrm{B}}\bar{\rho}}{\bar{m}}\bar{d}_{\mathrm{AB}}^2\left(\frac{16\pi\bar{k}_{\mathrm{B}}\bar{T}}{\bar{m}}\right)^{1/2}\exp\left(-\frac{\bar{e}_{\mathrm{A}}}{\bar{k}_{\mathrm{B}}\bar{T}}\right)$$
$$\bar{\rho}\frac{\mathrm{d}Y_{\mathrm{C}}}{\mathrm{d}\bar{t}} = 2\bar{n}\bar{\rho}Y_{\mathrm{A}}Y_{\mathrm{B}}\bar{d}_{\mathrm{AB}}^2(16\pi\bar{R}\bar{T})^{1/2}\exp\left(-\frac{\bar{E}_{\mathrm{A}}}{\bar{R}\bar{T}}\right) \tag{A.2}$$

The activation enerygy per unit mass is expressed as $\bar{E}_{\mathrm{A}} = \bar{e}_{\mathrm{A}}/m$. From the relation for packing factor,

$$\eta = \bar{n} \times \bar{V}_{\mathrm{hs}}$$
$$\eta = \bar{n} \times \frac{4}{3}\pi\frac{\bar{d}_{\mathrm{AB}}^3}{8}$$
$$\Rightarrow \bar{n} = \frac{6\eta}{\pi\bar{d}_{\mathrm{AB}}^3}$$

Substituting for $\bar{n}$ in equation (A.2)

$$\bar{\rho}\frac{\mathrm{d}Y_{\mathrm{C}}}{\mathrm{d}\bar{t}} = 12\frac{\eta}{\sqrt{\pi}\bar{d}_{\mathrm{AB}}}\bar{\rho}Y_{\mathrm{A}}Y_{\mathrm{B}}(16\bar{R}\bar{T})^{1/2}\exp\left(-\frac{\bar{E}_{\mathrm{A}}}{\bar{R}\bar{T}}\right) \tag{A.3}$$

Non-dimensional parameters:

$$\rho = \frac{\bar{\rho}}{\bar{\rho}_0} \quad T = \frac{\bar{R}\bar{T}}{\bar{e}_0} \quad u = \frac{\bar{u}}{\sqrt{\bar{e}_0}} \quad x = \frac{\bar{x}}{\bar{\lambda}_0} \quad t = \frac{\bar{t}\sqrt{\bar{e}_0}}{\bar{\lambda}_0} \tag{A.4}$$
$$Q = \frac{\bar{Q}}{\bar{e}_0} \quad E_{\mathrm{A}} = \frac{\bar{E}_{\mathrm{A}}}{\bar{e}_0} \quad e = \frac{\bar{e}}{\bar{e}_0} \quad \omega = \frac{\bar{\omega}\sqrt{\bar{e}_0}}{\bar{\rho}_0\bar{\lambda}_0} \tag{A.5}$$

The reaction rate is expressed by applying the above non-dimensional parameters as follows:

$$\omega_{\mathrm{C}} = \rho\frac{\mathrm{d}Y_{\mathrm{C}}}{\mathrm{d}t} = 48\frac{\eta}{\sqrt{\pi}d_{\mathrm{AB}}}\rho Y_{\mathrm{A}}Y_{\mathrm{B}}\sqrt{T}\exp\left(-\frac{E_{\mathrm{A}}}{T}\right) \tag{A.6}$$

Appendix B

Non-Dimensional Form of Continuum Models

Non-dimensional parameters

$$\rho = \frac{\bar{\rho}}{\bar{\rho}_0} \quad T = \frac{\bar{R}\bar{T}}{\bar{e}_0} \quad u = \frac{\bar{u}}{\sqrt{\bar{e}_0}} \quad x = \frac{\bar{x}}{\bar{\lambda}_0} \quad t = \frac{\bar{t}\sqrt{\bar{e}_0}}{\bar{\lambda}_0} \quad \mathrm{Le} = \frac{\bar{k}}{\bar{\rho}_0 \bar{c}_\mathrm{P} \bar{D}}$$
$$\mathrm{Pr} = \frac{\bar{\mu}\bar{c}_\mathrm{P}}{\bar{k}} \quad Q = \frac{\bar{Q}}{\bar{e}_0} \quad E_\mathrm{A} = \frac{\bar{E}_\mathrm{A}}{\bar{e}_0} \quad e = \frac{\bar{e}}{\bar{e}_0} \quad \omega = \frac{\bar{\omega}\bar{\lambda}_0}{\sqrt{\bar{\rho}_0 \bar{e}_0}}$$

B.1 Navier-Stokes Model

The 1D unsteady Navier-Stokes equation is given by

$$\frac{\partial \bar{\rho}}{\partial \bar{t}} + \frac{\partial(\bar{\rho}\bar{u})}{\partial \bar{x}} = 0 \tag{B.1}$$

$$\frac{\partial(\bar{\rho}_i)}{\partial \bar{t}} + \frac{\partial(\bar{\rho}_i(\bar{u} + \bar{V}_i))}{\partial \bar{x}} = \bar{\omega} \tag{B.2}$$

$$\frac{\partial(\bar{\rho}\bar{u})}{\partial \bar{t}} + \frac{\partial(\bar{\rho}\bar{u}^2 + \bar{p})}{\partial \bar{x}} = \frac{4}{3}\bar{\mu}\frac{\partial}{\partial \bar{x}}\left(\frac{\partial \bar{u}}{\partial \bar{x}}\right) \tag{B.3}$$

$$\frac{\partial(\bar{\rho}\bar{e}_{tot})}{\partial \bar{t}} + \frac{\partial\big((\bar{\rho}\bar{e}_{tot} + \bar{p})\bar{u}\big)}{\partial \bar{x}} = \bar{k}\frac{\partial}{\partial \bar{x}}\left(\frac{\partial \bar{T}}{\partial \bar{x}}\right) + \frac{4}{3}\bar{\mu}\frac{\partial}{\partial \bar{x}}\left(\bar{u}\frac{\partial \bar{u}}{\partial \bar{x}}\right) + \bar{Q}\bar{\omega} \tag{B.4}$$

where, the reaction rate, $\bar{\omega}$, is obtained from one-step Arrhenius form:

$$\bar{\omega} = \bar{k}_0 \bar{\rho} Y \exp\left(\frac{\bar{E}_\mathrm{A}}{\bar{R}\bar{T}}\right) \tag{B.5}$$

$\bar{e}_{tot} = \frac{\bar{p}}{\bar{\rho}(\gamma-1)} + \frac{1}{2}\bar{u}^2$, energy conservation is given by the sum of total sensible energy and kinetic energy.

Equation of state:

$$\bar{p} = \bar{\rho}\bar{R}\bar{T}$$

The non-dimensionalized reaction rate becomes,

$$\bar{\omega} = k_0 \rho Y \exp\left(\frac{E_\mathrm{A}}{T}\right) \tag{B.6}$$

Equations (B.1), (B.2), (B.3) and (B.4) are non-dimensionalized using the above mentioned non-dimensional parameters. By doing so, Equation (B.1) becomes,

$$\frac{\partial \rho}{\partial t} + \frac{\partial(\rho u)}{\partial x} = 0 \tag{B.7}$$

Equation (B.2) $\Rightarrow$

$$\frac{\partial(\rho Y_i)}{\partial t} + \frac{\partial(\rho u Y_i)}{\partial x} - \frac{\bar{D}}{\sqrt{\bar{e}_0}\bar{\lambda}_0}\frac{\partial}{\partial x}\left(\rho \frac{\partial Y_i}{\partial x}\right) = \omega_i$$

From kinetic theory [77], the relationship between mean free path and thermal conductivity is given by:

$$\begin{aligned}
\bar{k} &= \beta_\mathrm{k}\bar{n}\bar{m}\bar{C}\bar{\lambda}_0\bar{c}_\mathrm{V} \\
\bar{k} &= \beta_\mathrm{k}\bar{n}\bar{m}\bar{C}\bar{\lambda}_0\frac{\bar{\zeta}}{2}R \qquad \because \quad \bar{c}_\mathrm{V} = \frac{\bar{\zeta}}{2}R \\
\bar{k} &= \beta_\mathrm{k}\bar{\rho}_0\sqrt{3R\bar{T}}\bar{\lambda}_0\frac{\bar{\zeta}}{2}\frac{\bar{c}_\mathrm{P}(\gamma-1)}{\gamma} \qquad \because \quad \bar{C} = \sqrt{3R\bar{T}} \\
\bar{\lambda}_0 &= \frac{2\gamma}{\beta_\mathrm{k}3(\gamma-1)}\frac{\bar{k}}{\bar{\rho}_0\bar{c}_\mathrm{P}\sqrt{3R\bar{T}_0}} \\
\bar{\lambda}_0 &= \frac{2\gamma}{\beta_\mathrm{k}3(\gamma-1)}\frac{\bar{k}}{\bar{\rho}_0\bar{c}_\mathrm{P}\sqrt{2\bar{e}_0}}
\end{aligned}$$

where, $\bar{C}$ is the mean molecular speed and β_k is the proportionality constant in the energy transport. In the transport of energy there is a correlation between the velocity of the molecule and the amount of energy transported. That is, molecules with high translational energy tend to come from greater distances away from the place of its last collision. The value of the constant taking into account these and other secondary effects for monatomic gases is that

$$\beta_\mathrm{k} = \frac{5}{4}$$

$$\frac{\partial(\rho Y_i)}{\partial t} + \frac{\partial(\rho u Y_i)}{\partial x} - C\frac{1}{\mathrm{Le}}\frac{\partial}{\partial x}\left(\rho \frac{\partial Y_i}{\partial x}\right) = \omega_i \tag{B.8}$$

where, $C = \frac{\beta_\mathrm{k}3(\gamma-1)}{2\gamma}$. Similarly, (eq. (B.3)) can be written as,

$$\frac{\partial(\rho u)}{\partial t} + \frac{\partial(\rho u^2 + p)}{\partial x} = \frac{4}{3} C\mathrm{Pr} \frac{\partial}{\partial \bar{x}} \left(\frac{\partial u}{\partial x} \right) \tag{B.9}$$

Equation (B.4) $\Rightarrow$

$$\frac{\partial(\rho e_{tot})}{\partial t} + \frac{\partial\big((\rho e_{tot} + p)u\big)}{\partial x} = C \frac{\gamma}{\gamma - 1} \frac{\partial}{\partial \bar{x}} \left(\frac{\partial T}{\partial x} \right) + \frac{4}{3} C\mathrm{Pr} \frac{\partial}{\partial x} \left(u \frac{\partial u}{\partial x} \right) + Q\omega \tag{B.10}$$

B.2 Euler Model

The 1D unsteady Euler equations are obtained by eliminating the transport terms in the governing equations B.1 - B.4.

$$\frac{\partial \bar{\rho}}{\partial \bar{t}} + \frac{\partial(\bar{\rho}\bar{u})}{\partial \bar{x}} = 0 \tag{B.11}$$

$$\frac{\partial(\bar{\rho}\bar{Y}_i)}{\partial \bar{t}} + \frac{\partial(\bar{\rho}\bar{u}\bar{Y}_i)}{\partial \bar{x}} = \bar{\omega}_i \tag{B.12}$$

$$\frac{\partial(\bar{\rho}\bar{u})}{\partial \bar{t}} + \frac{\partial(\bar{\rho}\bar{u}^2 + \bar{p})}{\partial \bar{x}} = 0 \tag{B.13}$$

$$\frac{\partial(\bar{\rho}\bar{e}_{tot})}{\partial \bar{t}} + \frac{\partial\big((\bar{\rho}\bar{e}_{tot} + \bar{p})\bar{u}\big)}{\partial \bar{x}} = \bar{Q}\bar{\omega}_i \tag{B.14}$$

And the reaction rate is obtained from kinetic theory as mentioned in (eq. (A.6)).The process of non-dimensionalizing the Euler equations is straightforward and utilizes the same dimensionless parameters presented above. The non-dimensional form of governing equations are:

$$\frac{\partial \rho}{\partial t} + \frac{\partial(\rho u)}{\partial x} = 0 \tag{B.15}$$

$$\frac{\partial(\rho Y_i)}{\partial t} + \frac{\partial(\rho u Y_i)}{\partial x} = \omega_i \tag{B.16}$$

$$\frac{\partial(\rho u)}{\partial t} + \frac{\partial(\rho u^2 + p)}{\partial x} = 0 \tag{B.17}$$

$$\frac{\partial(\rho e_{tot})}{\partial t} + \frac{\partial\big((\rho e_{tot} + p)u\big)}{\partial x} = Q\omega_i \tag{B.18}$$

Appendix C

Steady State Viscous Detonations

C.1 Governing Equations for Steady State Viscous Detonations Structure

The 1D steady Navier-Stokes equation is given by

$$\frac{\mathrm{d}}{\mathrm{d}\bar{x}}(\bar{\rho}\bar{u}) = 0 \tag{C.1}$$

$$\frac{\mathrm{d}}{\mathrm{d}\bar{x}}(\bar{\rho}\bar{u}^2 + \bar{p}) = \frac{4}{3}\frac{\mathrm{d}}{\mathrm{d}\bar{x}}\left(\bar{\mu}\frac{\mathrm{d}\bar{u}}{\mathrm{d}\bar{x}}\right) \tag{C.2}$$

$$\frac{\mathrm{d}}{\mathrm{d}\bar{x}}\left(\bar{\rho}(\bar{c}_{\mathrm{P}}\bar{T} + \frac{\bar{u}^2}{2})\bar{u}\right) = \frac{\mathrm{d}}{\mathrm{d}\bar{x}}\left(\bar{k}\frac{\mathrm{d}\bar{T}}{\mathrm{d}\bar{x}}\right) + \frac{4}{3}\frac{\mathrm{d}}{\mathrm{d}\bar{x}}\left(\bar{\mu}\bar{u}\frac{\mathrm{d}\bar{u}}{\mathrm{d}\bar{x}}\right) + \bar{Q}\bar{\omega} \tag{C.3}$$

$$\frac{\mathrm{d}}{\mathrm{d}\bar{x}}(\bar{\rho}\bar{u}Y) = \frac{\mathrm{d}}{\mathrm{d}\bar{x}}\left(\bar{\rho}\bar{D}\frac{\mathrm{d}Y}{\mathrm{d}\bar{x}}\right) - \bar{\omega} \tag{C.4}$$

$$\bar{\omega} = \bar{k}_0\bar{\rho}Y\exp\left(-\frac{\bar{E}_{\mathrm{A}}}{\bar{R}\bar{T}}\right) \tag{C.5}$$

Equation of state:

$$\bar{p} = \bar{\rho}\bar{R}\bar{T}$$

Eqns. (C.3) + (C.4)$\bar{Q}$ gives,

$$\frac{\mathrm{d}\left(\bar{\rho}\left(\bar{c}_{\mathrm{P}}\bar{T} + Y\bar{Q} + \frac{\bar{u}^2}{2}\right)\bar{u}\right)}{\mathrm{d}\bar{x}} = \frac{\mathrm{d}}{\mathrm{d}\bar{x}}\left(\bar{k}\frac{\mathrm{d}\bar{T}}{\mathrm{d}\bar{x}}\right) + \frac{4}{3}\frac{\mathrm{d}}{\mathrm{d}\bar{x}}\left(\bar{\mu}\bar{u}\frac{\mathrm{d}\bar{u}}{\mathrm{d}\bar{x}}\right) + \frac{\mathrm{d}}{\mathrm{d}\bar{x}}\left(\bar{\rho}\bar{D}\bar{Q}\frac{\mathrm{d}Y}{\mathrm{d}\bar{x}}\right) \tag{C.6}$$

Eq. (C.4) can be written as:

$$\frac{\mathrm{d}}{\mathrm{d}\bar{x}}\Bigg(\underbrace{\bar{\rho}\bar{u}Y - \bar{\rho}\bar{D}\frac{\mathrm{d}Y}{\mathrm{d}\bar{x}}}_{\bar{G}}\Bigg) = -\bar{\omega}$$

$$\frac{\mathrm{d}\bar{G}}{\mathrm{d}\bar{x}} = -\bar{\omega} \tag{C.7}$$

where,

$$\bar{G} = \bar{\rho}\bar{u}Y - \bar{\rho}\bar{D}\frac{\mathrm{d}Y}{\mathrm{d}\bar{x}}$$

Upon rearranging,

$$\frac{\mathrm{d}Y}{\mathrm{d}\bar{x}} = \frac{1}{\bar{\rho}\bar{D}}\big(\bar{\rho}\bar{u}Y - \bar{G}\big) \tag{C.8}$$

Integrating Eq. (C.1) with respect to $\bar{x}$ and applying the boundary condition to find the integration constant. The same procedure is repeated for eqs. (C.2) and (C.6).

$$\begin{aligned}\bar{\rho}\bar{u} &= \text{const.}\\ \bar{\rho}\bar{u} &= \bar{\rho}_{\mathrm{u}}\bar{u}_{\mathrm{u}} = m\end{aligned} \tag{C.9}$$

Eq. (C.2) $\Rightarrow$

$$\begin{aligned}\big(\bar{\rho}\bar{u}^2 + \bar{p}\big) &= \frac{4}{3}\bar{\mu}\frac{\mathrm{d}\bar{u}}{\mathrm{d}\bar{x}} + \text{const.}\\ \big(\bar{\rho}_{\mathrm{u}}\bar{u}_{\mathrm{u}}^2 + \bar{p}_{\mathrm{u}}\big) &= \text{const.}\\ \bar{\rho}\bar{u}^2 + \bar{p} &= \frac{4}{3}\bar{\mu}\frac{\mathrm{d}\bar{u}}{\mathrm{d}\bar{x}} + \bar{\rho}_{\mathrm{u}}\bar{u}_{\mathrm{u}}^2 + \bar{p}_{\mathrm{u}}\\ \frac{\mathrm{d}\bar{u}}{\mathrm{d}\bar{x}} &= \frac{3}{4\bar{\mu}}\Big(\bar{\rho}\bar{u}^2 + \bar{\rho}\bar{R}\bar{T} - \bar{\rho}_{\mathrm{u}}\bar{u}_{\mathrm{u}}^2 - \bar{\rho}_{\mathrm{u}}\bar{R}\bar{T}_{\mathrm{u}}\Big)\end{aligned} \tag{C.10}$$

Eq. (C.6) $\Rightarrow$

$$\begin{aligned}\bar{\rho}\big(\bar{c}_{\mathrm{P}}\bar{T} + Y\bar{Q} + \frac{\bar{u}^2}{2}\big)\bar{u} - \bar{\rho}_{\mathrm{u}}\big(\bar{c}_{\mathrm{P}}\bar{T}_{\mathrm{u}} + Y_{\mathrm{u}}\bar{Q} + \frac{\bar{u}_{\mathrm{u}}^2}{2}\big)\bar{u}_{\mathrm{u}} &= \bar{k}\frac{\mathrm{d}\bar{T}}{\mathrm{d}\bar{x}} + \frac{4}{3}\bar{\mu}\bar{u}\frac{\mathrm{d}\bar{u}}{\mathrm{d}\bar{x}} + \bar{\rho}\bar{D}\bar{Q}\frac{\mathrm{d}Y}{\mathrm{d}\bar{x}}\\ \frac{\mathrm{d}\bar{T}}{\mathrm{d}\bar{x}} = \frac{1}{\bar{k}}\Bigg(\bar{\rho}\big(\bar{c}_{\mathrm{P}}\bar{T} + Y\bar{Q} + \frac{\bar{u}^2}{2}\big)\bar{u} - \bar{\rho}_{\mathrm{u}}\big(\bar{c}_{\mathrm{P}}\bar{T}_{\mathrm{u}} + Y_{\mathrm{u}}\bar{Q} + \frac{\bar{u}_{\mathrm{u}}^2}{2}\big)\bar{u}_{\mathrm{u}} - \frac{4}{3}\bar{\mu}\bar{u}\frac{\mathrm{d}\bar{u}}{\mathrm{d}\bar{x}} - \bar{\rho}\bar{D}\bar{Q}\frac{\mathrm{d}Y}{\mathrm{d}\bar{x}}\Bigg)\end{aligned} \tag{C.11}$$

Eqns. (C.7) - (C.11) are the simplified form of the governing equations. The steady detonation structure is obtained by integrating this system of ODEs, which leads to the formation of a quartet of equations to solve for G, T, u, and Y.

C.1.1 Non-Dimensional Form of Simplified Governing Equation

Non-dimensional parameters

$$\rho = \frac{\bar{\rho}}{\bar{\rho}_\mathrm{u}} \quad T = \frac{R\bar{T}}{\bar{c}_\mathrm{u}^2} = \frac{1}{\gamma}\frac{\bar{T}}{\bar{T}_\mathrm{u}} \quad p = \frac{\bar{p}}{\bar{\rho}_\mathrm{u}\bar{c}_\mathrm{u}^2} = \frac{1}{\gamma}\frac{\bar{p}}{\bar{p}_\mathrm{u}} \quad u = \frac{\bar{u}}{\bar{c}_\mathrm{u}} \quad x = \frac{\bar{x}\bar{\rho}_\mathrm{u}\bar{c}_\mathrm{P}\bar{c}_\mathrm{u}}{\bar{k}} \quad t = \frac{\bar{t}\bar{\rho}_\mathrm{u}\bar{c}_\mathrm{P}\bar{c}_\mathrm{u}^2}{\bar{k}}$$
$$\mathrm{Pr} = \frac{\bar{\mu}\bar{c}_\mathrm{P}}{\bar{k}} \quad \omega = \frac{\bar{\omega}\bar{k}}{\bar{\rho}_\mathrm{u}^2\bar{c}_\mathrm{P}\bar{c}_\mathrm{u}^2} \quad Q = \frac{1}{\gamma}\frac{\bar{Q}}{R\bar{T}_\mathrm{u}} \quad E = \frac{1}{\gamma}\frac{\bar{E}_\mathrm{A}}{R\bar{T}_\mathrm{u}} \quad e = \frac{1}{\gamma}\frac{\bar{e}}{R\bar{T}_\mathrm{u}} \quad G = \frac{\bar{G}}{\bar{\rho}_\mathrm{u}\bar{c}_\mathrm{u}}$$

Equations (C.7), (C.8), (C.10) and (C.11) are non-dimensionalized using the above-mentioned scaling.

$$\frac{\mathrm{d}G}{\mathrm{d}x} = -\frac{mY\Gamma_0}{u}\exp\left(-\frac{E_\mathrm{A}}{T}\right) \tag{C.12}$$

where, $\Gamma_0 = \frac{k_0\bar{k}}{\gamma\bar{p}_\mathrm{u}\bar{c}_\mathrm{P}}$.

$$\frac{\mathrm{d}Y}{\mathrm{d}x} = \mathrm{Le}\Big(mY - G\Big) \tag{C.13}$$

$$\frac{\mathrm{d}u}{\mathrm{d}x} = \frac{3}{4\mathrm{Pr}}\left(m(u-u_\mathrm{u}) + \left(\frac{mT}{u} - T_\mathrm{u}\right)\right) \tag{C.14}$$

$$\frac{\mathrm{d}T}{\mathrm{d}x} = m(T-T_\mathrm{u}) + \frac{\gamma-1}{\gamma}\left(Q(G-mY_\mathrm{u}) - \frac{1}{2}m(u-u_\mathrm{u})^2 - (mT - uT_\mathrm{u})\right) \tag{C.15}$$

C.2 Linearization of the Steady State Equation

A saddle point near the hot boundary state of this system causes numerical integration to fail to converge as x approaches infinity. To overcome the singularities resulting from burned gas conditions in the compressible regimes, namely saddle points, the linearized version of the governing equation employs eigenvalue decomposition. Consequently, the non-dimensional form of the simplified governing equations is linearized in the vicinity of the hot boundary.

$$\frac{\mathrm{d}u}{\mathrm{d}x} = \frac{3}{4\mathrm{Pr}}\left(m(u-u_\mathrm{u}) + \left(\frac{mT}{u} - T_\mathrm{u}\right)\right)$$
$$\frac{\mathrm{d}T}{\mathrm{d}x} = m(T-T_\mathrm{u}) + \frac{\gamma-1}{\gamma}\left(Q(G-mY_\mathrm{u}) - \frac{1}{2}m(u-u_\mathrm{u})^2 + (uT_\mathrm{u} - mT)\right)$$

$$\frac{\mathrm{d}Y}{\mathrm{d}x} = \mathrm{Le}\Big(mY - G\Big)$$
$$\frac{\mathrm{d}G}{\mathrm{d}x} = -\frac{mY\Gamma_0}{u}\exp\Big(-\frac{E_\mathrm{A}}{T}\Big)$$

$$\frac{\mathrm{d}u}{\mathrm{d}x} = \frac{3}{4\mathrm{Pr}}\Bigg(m(u_\mathrm{b}-u_\mathrm{u}) + T_\mathrm{u}\Big(\frac{mT_\mathrm{b}}{u_\mathrm{b}T_\mathrm{u}}-1\Big) + (u-u_\mathrm{b})\Big(m+\Big(\frac{-mT_\mathrm{b}}{u_\mathrm{b}^2}\Big)\Big) + (T-T_\mathrm{b})\frac{m}{u_\mathrm{b}}\Bigg)$$

$$\frac{\mathrm{d}u}{\mathrm{d}x} = \frac{3}{4\mathrm{Pr}}\Bigg((u-u_\mathrm{b})m\Big(1-\frac{T_\mathrm{b}}{u_\mathrm{b}^2}\Big) + (T-T_\mathrm{b})\frac{m}{u_\mathrm{b}}\Bigg) \tag{C.16}$$

$$\frac{\mathrm{d}T}{\mathrm{d}x} = m(T_\mathrm{b}-T_\mathrm{u}) + \frac{\gamma-1}{\gamma}\Big(Q(G_\mathrm{b}-mY_\mathrm{u}) - \frac{1}{2}m(u_\mathrm{b}-u_\mathrm{u})^2 - (mT_\mathrm{b}-u_\mathrm{b}T_\mathrm{u})\Big)$$
$$+(G-G_\mathrm{b})\Big(\frac{\gamma-1}{\gamma}\Big)Q + (T-T_\mathrm{b})m\Big(1-\Big(\frac{\gamma-1}{\gamma}\Big)\Big) + (u-u_\mathrm{b})\Big(\frac{\gamma-1}{\gamma}\Big)\Big(-\frac{1}{2}2m(u_\mathrm{b}-u_\mathrm{u})+T_\mathrm{u}\Big)$$

$$\frac{\mathrm{d}T}{\mathrm{d}x} = (G-G_\mathrm{b})\Big(\frac{\gamma-1}{\gamma}\Big)Q + (T-T_\mathrm{b})\frac{m}{\gamma} + (u-u_\mathrm{b})\Big(\frac{\gamma-1}{\gamma}\Big)\Big(-m(u_\mathrm{b}-u_\mathrm{u})+T_\mathrm{u}\Big) \tag{C.17}$$

$$\frac{\mathrm{d}Y}{\mathrm{d}x} = \mathrm{Le}\Big((mY_\mathrm{b}-G_\mathrm{b}) + (Y-Y_\mathrm{b})m - (G-G_\mathrm{b})\Big)$$

$$\frac{\mathrm{d}Y}{\mathrm{d}x} = \mathrm{Le}\Big((Y-Y_\mathrm{b})m - (G-G_\mathrm{b})\Big) \tag{C.18}$$

$$\frac{\mathrm{d}G}{\mathrm{d}x} = -\frac{mY_\mathrm{b}\Gamma_0}{u_\mathrm{b}}\exp(-\frac{E_\mathrm{A}}{T_\mathrm{b}}) - (Y-Y_\mathrm{b})\frac{m\Gamma_0}{u_\mathrm{b}}\exp(-\frac{E_\mathrm{A}}{T_\mathrm{b}}) - (T-T_\mathrm{b})\frac{mY_\mathrm{b}\Gamma_0}{u_\mathrm{b}}\frac{E_\mathrm{A}\exp(-\frac{E_\mathrm{A}}{T_\mathrm{b}})}{T_\mathrm{b}^2}$$
$$+(u-u_\mathrm{b})\frac{m\Gamma_0}{u_\mathrm{b}^2}Y_\mathrm{b}\exp(-\frac{E_\mathrm{A}}{T_\mathrm{b}})$$

$$\frac{\mathrm{d}G}{\mathrm{d}x} = -(Y-Y_\mathrm{b})\frac{m\Gamma_0}{u_\mathrm{b}}\exp(-\frac{E_\mathrm{A}}{T_\mathrm{b}}) - (T-T_\mathrm{b})\frac{mY_\mathrm{b}\Gamma_0}{u_\mathrm{b}}\frac{E_\mathrm{A}\exp(-\frac{E_\mathrm{A}}{T_\mathrm{b}})}{T_\mathrm{b}^2} + (u-u_\mathrm{b})\frac{m\Gamma_0}{u_\mathrm{b}^2}Y_\mathrm{b}\exp(-\frac{E_\mathrm{A}}{T_\mathrm{b}})$$

$$\frac{\mathrm{d}G_i}{\mathrm{d}x} = -(Y - Y_\mathrm{b})\frac{m\Gamma_0}{u_\mathrm{b}}\exp(-\frac{E_\mathrm{A}}{T_\mathrm{b}}) \tag{C.19}$$

$$u' = u - u_\mathrm{b} \qquad T' = T - T_\mathrm{b}$$
$$G' = G - G_\mathrm{b} \qquad Y' = Y - Y_\mathrm{b}$$

Applying the above deviation variable to Eqns. (C.16)-(C.19)

$$\begin{aligned}
\frac{\mathrm{d}u'}{\mathrm{d}x} &= \frac{3}{4\mathrm{Pr}}\left(u'm\left(1 - \frac{T_\mathrm{b}}{u_\mathrm{b}^2}\right) + T'\frac{m}{u_\mathrm{b}}\right)\\
\frac{\mathrm{d}T'}{\mathrm{d}x} &= G'\left(\frac{\gamma-1}{\gamma}\right)Q + T'\frac{m}{\gamma} + u'\left(\frac{\gamma-1}{\gamma}\right)\left(-m(u_\mathrm{b} - u_\mathrm{u}) + T_\mathrm{u}\right)\\
\frac{\mathrm{d}Y'}{\mathrm{d}x} &= \mathrm{Le}\left(mY' - G'\right)\\
\frac{\mathrm{d}G_i'}{\mathrm{d}x} &= -Y'\frac{m\Gamma_0}{u_\mathrm{b}}\exp(-\frac{E_\mathrm{A}}{T_\mathrm{b}})
\end{aligned}$$

The system of equations can be expressed in matrix form as

$$U^{'} = AU$$

where,

$$A = \begin{bmatrix}
\frac{3}{4\mathrm{Pr}}\left(m\left(1 - \frac{T_\mathrm{b}}{u_\mathrm{b}^2}\right)\right) & \frac{3}{4\mathrm{Pr}}\left(\frac{m}{u_\mathrm{b}}\right) & 0 & 0\\
\left(\frac{\gamma-1}{\gamma}\right)\left(-m(u_\mathrm{b} - u_\mathrm{u}) + T_\mathrm{u}\right) & \frac{m}{\gamma} & 0 & \left(\frac{\gamma-1}{\gamma}\right)Q\\
0 & 0 & m\mathrm{Le} & -\mathrm{Le}\\
0 & 0 & -\frac{m\Gamma_0}{u_\mathrm{b}}\exp(-\frac{E_\mathrm{A}}{T_\mathrm{b}}) & 0
\end{bmatrix}$$

$$U = \begin{bmatrix} u^{'} \\ T^{'} \\ Y^{'} \\ G^{'} \end{bmatrix} \qquad U^{'} = \begin{bmatrix} \frac{\mathrm{d}u^{'}}{\mathrm{d}x} \\ \frac{\mathrm{d}T^{'}}{\mathrm{d}x} \\ \frac{\mathrm{d}Y^{'}}{\mathrm{d}x} \\ \frac{\mathrm{d}G^{'}}{\mathrm{d}x} \end{bmatrix}$$

References

[1] A. L. Sánchez and F. A. Williams, "Recent advances in understanding of flammability characteristics of hydrogen," Prog. Energy and Combust. Sci., vol. 41, pp. 1–55, 2014.

[2] M. I. Radulescu, G. J. Sharpe, C. K. Law, and J. H. Lee, "The hydrodynamic structure of unstable cellular detonations," Journal of Fluid Mechanics, vol. 580, p. 31, 2007.

[3] J. H. Lee, The detonation phenomenon. Cambridge University Press, 2008.

[4] D. W. Brenner, D. Robertson, M. Elert, and C. White, "Detonations at nanometer resolution using molecular dynamics," Physical review letters, vol. 70, no. 14, p. 2174, 1993.

[5] A. J. Heim, N. Grønbech-Jensen, E. M. Kober, and T. C. Germann, "Molecular dynamics simulations of detonation instability," Physical Review E, vol. 78, no. 4, p. 046710, 2008.

[6] N. Sirmas and M. I. Radulescu, "Thermal ignition revisited with two-dimensional molecular dynamics: role of fluctuations in activated collisions," Combustion and Flame, vol. 13, pp. 79–88, 2017.

[7] A. Mulero, C. A. Galan, M. I. Parra, and F. Cuadros, "Equations of state for hard spheres and hard disks," Lect. Notes Phys., vol. 753, pp. 37–109, 2008.

[8] I. Prigogine and M. Mahieu, "Sur la perturbation de la distribution de Maxwell par des reactions chimiques en phase gazeuse," Physica, vol. 16, no. 1, pp. 51–64, 1950.

[9] F. Zangene, Q. Xiao, and M. Radulescu, "Critical diffraction of irregular structure detonations and their predictability from experimentally obtained $d\kappa$ data," Proceedings of the Combustion Institute, 2022.

[10] I. B. Zel'dovich, A. P. Genich, and G. B. Manelis, "Distinctive features of translational relaxation at a shock-wave front in gas mixtures," Doklady Akademii Nauk SSSR, vol. 248, no. 2, p. 349–351, 1979.

[11] V. Velikodnyi, "Effects of translational nonequilibrium in the shock wave front in dense gases and liquids," High Temperature, vol. 40, pp. 62–70, 2002.

[12] M. I. Radulescu, The propagation and failure mechanism of gaseous detonations: experiments in porous-walled tubes. PhD thesis, McGill University, 2003.

[13] Q. Xiao and M. I. Radulescu, "Role of instability on the limits of laterally strained detonation waves," Combustion and Flame, vol. 220, pp. 410–428, 2020.

[14] F. A. Williams, Combustion Theory. The Benjamin/Cummins Publishing Company, Menlo Park, California, 1985.

[15] I. Prigogine and E. Xhrouet, "On the perturbation of Maxwell distribution function by chemical reactions in gases," Physica, vol. 15, no. 11-12, pp. 913–932, 1949.

[16] A. Borisov, "On the origin of exothermic centres in gaseous mixtures," Acta Astronautica, vol. 1, no. 7, pp. 909–920, 1974.

[17] J. Gorecki and J. Gryko, "The adiabatic thermal explosion in a small system: Comparison of the stochastic approach with the molecular dynamics simulation," J. Stat. Phys., vol. 48, no. 1-2, pp. 329–342, 1987.

[18] J. Gorecki, J. Popielawski, and A. S. Cukrowski, "Molecular-dynamics study on the influence of nonequilibrium effects on the rate of chemical reaction," Physical Review A, vol. 44, no. 6, pp. 3791–3795, 1991.

[19] J. Gorecki and J. N. Gorecka, "Molecular dynamics simulations of nonequilibrium rate constant in a model exothermic reaction," Chem. Phys. Lett., vol. 319, no. 1-2, pp. 173–178, 2000.

[20] A. Lemarchand and B. Nowakowski, "Fluctuation-induced and nonequilibrium-induced bifurcations in a thermochemical system," Molecular Simulation, vol. 30, no. 11-12, pp. 773–780, 2004.

[21] R. Present, "Chapman-Enskog method in chemical kinetics," J. Chem. Phys., vol. 48, no. 11, pp. 4875–4877, 1968.

[22] B. D. Shizgal and M. Karplus, "Nonequilibrium contributions to the rate of reaction. I. Perturbation of the velocity distribution function," J. Chem. Phys., vol. 52, no. 8, pp. 4262–4278, 1970.

[23] B. D. Shizgal and D. G. Napier, "Nonequilibrium effects in reactive systems; the effect of reaction products and the validity of the Chapman-Enskog method," Physica A, vol. 223, pp. 50–86, 1996.

[24] S. Chapman and T. G. Cowling, The mathematical theory of non-uniform gases. Cambridge University Press, 1958.

[25] A. M. Dean, "Predictions of pressure and temperature effects upon radical addition and recombination reactions," American Chemical Society, vol. 89, pp. 4600–4608, 1985.

[26] P. R. Westmoreland, J. B. Howard, J. P. Longwell, and A. M. Dean, "Combustion and pyrolysis reactions by bimolecular QRRK," AIChE Journal, vol. 32, no. 12, pp. 1971–1979, 1985.

[27] M. Döntgen, L. C. Kröger, and K. Leonhard, "Hot β-scission of radicals formed via hydrogen abstraction," Proc. Combust. Inst., vol. 36, pp. 135–142, 2017.

[28] M. Döntgen and K. Leonhard, "Discussion of the separation of chemical and relaxational kinetics of chemically activated intermediates in master equation simulations," J. Phys. Chem., vol. 121, pp. 1563–1570, 2017.

[29] M. P. Burke, C. F. Goldsmith, Y. Georgievskii, and S. J. Klippenstein, "Towards a quantitative understanding of the role of non-Boltzmann reactant distributions in low temperature oxidation," Proc. Combust. Inst., vol. 35, pp. 205–213, 2015.

[30] N. J. Labbe, R. Sivaramakrishnan, C. F. Goldsmith, Y. Georgievskii, J. A. Miller, and S. J. Klippenstein, "Ramifications of including non-equilibrium effects for HCO in flame chemistry," Proc. Combust. Inst., vol. 36, pp. 525–532, 2017.

[31] C. F. Goldsmith, M. P. Burke, Y. Georgievskii, and S. J. Klippenstein, "Effect of non-thermal product energy distributions on ketohydroperoxide decomposition kinetics," Proc. Combust. Inst., vol. 35, pp. 283–290, 2015.

[32] M. M. Mansour and F. Baras, "Microscopic simulation of chemical systems," Physica A, vol. 188, no. 1, pp. 253–276, 1992.

[33] W. Fickett and W. C. Davis, Detonation. University of California Press, 1979.

[34] V. Gamezo, D. Desbordes, and E. Oran, "Two-dimensional reactive flow dynamics in cellular detonation waves," Shock waves, vol. 9, pp. 11–17, 1999.

[35] G. J. Sharpe, "Transverse waves in numerical simulations of cellular detonations," Journal of Fluid Mechanics, vol. 447, pp. 31–51, 2001.

[36] G. Cael, H. D. Ng, K. R. Bates, N. Nikiforakis, and M. Short, "Numerical simulation of detonation structures using a thermodynamically consistent and fully conservative reactive flow model for multi-component computations," Proceedings of the Royal Society A: Mathematical, Physical and Engineering Sciences, vol. 465, no. 2107, pp. 2135–2153, 2009.

[37] M. Radulescu, A. Matsuo, and C. Law, "A convective-diffusive reaction zone structure model for turbulent detonations," in 44th AIAA Aerospace Sciences Meeting and Exhibit, p. 951, 2006.

[38] Y. Mahmoudi, N. Karimi, R. Deiterding, and S. Emami, "Hydrodynamic instabilities in gaseous detonations: comparison of euler, navier–stokes, and large-eddy simulation," Journal of Propulsion and Power, vol. 30, no. 2, pp. 384–396, 2014.

[39] V. Gamezo, A. Vasil'Ev, A. Khokhlov, and E. Oran, "Fine cellular structures produced by marginal detonations," Proceedings of the Combustion Institute, vol. 28, no. 1, pp. 611–617, 2000.

[40] J. L. Ziegler, R. Deiterding, J. E. Shepherd, and D. I. Pullin, "An adaptive high-order hybrid scheme for compressive, viscous flows with detailed chemistry," Journal of Computational Physics, vol. 230, no. 20, pp. 7598–7630, 2011.

[41] R. H. Kraichnan, "Inertial ranges in two-dimensional turbulence," The Physics of Fluids, vol. 10, no. 7, pp. 1417–1423, 1967.

[42] C. E. Leith, "Diffusion approximation for two-dimensional turbulence," The Physics of Fluids, vol. 11, no. 3, pp. 671–672, 1968.

[43] G. K. Batchelor, "Computation of the energy spectrum in homogeneous two-dimensional turbulence," The Physics of Fluids, vol. 12, no. 12, pp. II–233, 1969.

[44] K. Gottiparthi, F. Genin, S. Srinivasan, and S. Menon, "Simulation of cellular detonation structures in ethylene-oxygen mixtures," in 47th AIAA Aerospace Sciences Meeting including The New Horizons Forum and Aerospace Exposition, p. 437, 2009.

[45] S. Menon and W. H. Calhoon, "Subgrid mixing and molecular transport modeling in a reacting shear layer," Symposium (International) on Combustion, vol. 26, no. 1, pp. 59–66, 1996.

[46] V. Chakravarthy and S. Menon, "Subgrid modeling of turbulent premixed flames in the flamelet regime," Flow, turbulence and combustion, vol. 65, pp. 133–161, 2000.

[47] V. Sankaran and S. Menon, "Les of scalar mixing in supersonic mixing layers," Proceedings of the combustion Institute, vol. 30, no. 2, pp. 2835–2842, 2005.

[48] B. M. Maxwell, Turbulent combustion modelling of fast-flames and detonations using compressible LEM-LES. PhD thesis, Université d'Ottawa/University of Ottawa, 2016.

[49] J. Austin, The role of instability in gaseous detonation Ph. D. PhD thesis, thesis, California Institute of Technology, Pasadena, California, USA, 2003.

[50] J. Austin, F. Pintgen, and J. Shepherd, "Reaction zones in highly unstable detonations," Proceedings of the Combustion Institute, vol. 30, no. 2, pp. 1849–1857, 2005.

[51] V. Manzhalei, "Fine structure of the leading front of a gas detonation," Combustion, Explosion and Shock Waves, vol. 13, no. 3, pp. 402–404, 1977.

[52] B. M. Maxwell, R. R. Bhattacharjee, S. S. Lau-Chapdelaine, S. A. Falle, G. J. Sharpe, and M. I. Radulescu, "Influence of turbulent fluctuations on detonation propagation," Journal of Fluid Mechanics, vol. 818, pp. 646–696, 2017.

[53] J. Dold and A. Kapila, "Comparison between shock initiations of detonation using thermally-sensitive and chain-branching chemical models," Combustion and Flame, vol. 85, no. 1-2, pp. 185–194, 1991.

[54] J. Dold, A. Kapila, and M. Short, "Theoretical description of direct initiation of detonation for one-step chemistry," Dynamic structure of detonation in gaseous and dispersed media, pp. 109–141, 1991.

[55] J. J. Gilman, "Mechanochemistry," science, vol. 274, no. 5284, pp. 65–65, 1996.

[56] M. R. Armstrong, J. M. Zaug, N. Goldman, I.-F. W. Kuo, J. C. Crowhurst, W. M. Howard, J. A. Carter, M. Kashgarian, J. M. Chesser, T. W. Barbee, et al., "Ultrafast shock initiation of exothermic chemistry in hydrogen peroxide," The Journal of Physical Chemistry A, vol. 117, no. 49, pp. 13051–13058, 2013.

[57] J. B. Anderson and L. N. Long, "Direct monte carlo simulation of chemical reaction systems: Prediction of ultrafast detonations," The Journal of chemical physics, vol. 118, no. 7, pp. 3102–3110, 2003.

[58] D. R. White, "Turbulent Structure of Gaseous Detonation," The Physics of Fluids, vol. 4, pp. 465–480, 04 1961.

[59] S. Rybanin, "Turbulence in detonation," Combustion Explosion and Shock Waves, vol. 2, pp. 15–18, 1966.

[60] M. Reynaud, S. Taileb, and A. Chinnayya, "Computation of the mean hydrodynamic structure of gaseous detonations with losses," Shock Waves, vol. 30, p. 645–669, 2020.

[61] Y. A. Nikolaev and D. V. Zak, "Quasi-one-dimensional model of self-sustaining multifront gas detonation with losses and turbulence taken into account," Combustion Explosion and Shock Waves, vol. 25, p. 103–112, 1989.

[62] J. H. S. Lee and M. I. Radulescu, "On the hydrodynamic thickness of cellular detonations," Combustion Explosion and Shock Waves, vol. 41, no. 6, pp. 745–765, 2005.

[63] J. Lee, R. Knystautas, and C. Guirao, "The link between cell size, critical tube diameter, initiation energy and detonability limits," Fuel-Air Explosions, pp. 157–187, 1982.

[64] D. Edwards, A. Jones, and D. Phillips, "The location of the chapman-jouguet surface in a multiheaded detonation wave," Journal of Physics D: Applied Physics, vol. 9, no. 9, p. 1331, 1976.

[65] R. Soloukhin, "Multiheaded structure of gaseous detonation," Combustion and Flame, vol. 10, no. 1, pp. 51–58, 1966.

[66] C. Brochet, N. Manson, M. Rouze, and W. Struck, "Influence of the initial pressure on the velocity of stable detonations in stoichiometric mixtures of propane-oxygen and acetylene-oxygen," C. R. Hebd. Sceances Acad. Sci., vol. 257, pp. 2412–2414, 1963.

[67] M. I. Radulescu and B. Borzou, "Dynamics of detonations with a constant mean flow divergence," Journal of Fluid Mechanics, vol. 845, pp. 346–377, 2018.

[68] W. Wood, "Existence of detonations for large values of the rate parameter," The Physics of Fluids, vol. 6, no. 8, pp. 1081–1090, 1963.

[69] V. Gamezo, A. Poludnenko, and E. Oran, "One-dimensional evolution of fast flames," in Proceedings of the 23rd International Colloquium on the Dynamics of Explosions and Reactive Systems, Irvine, CA, vol. 25, 2011.

[70] X. Mi, E. V. Timofeev, and A. J. Higgins, "Effect of spatial discretization of energy on detonation wave propagation," Journal of Fluid Mechanics, vol. 817, p. 306–338, 2017.

[71] M. I. Radulescu and J. E. Shepherd, "Dynamics of galloping detonations: inert hydrodynamics with pulsed energy release," in Bulletin of the American Physical Society, 68th Annual Meeting of the APS Division of Fluid Dynamics, (Boston, MA), 22 - 25 November 2015.

[72] J. Lee, Dynamics of Exothermicity, ch. On the critical diameter problem, p. 321–336. Gordon and Breech, 1996.

[73] E. Schultz, Detonation diffraction through an abrupt area expansion. PhD thesis, California Institute of Technology, 2000.

[74] I. Moen, A. Sulmistras, G. Thomas, D. Bjerketvedt, and P. Thibault, "Influence of cellular regularity on the behavior of gaseous detonations," Dynamics of explosions, pp. 220–243, 1986.

[75] D. Edwards, G. Thomas, and M. Nettleton, "The diffraction of a planar detonation wave at an abrupt area change," Journal of Fluid Mechanics, vol. 95, no. 1, pp. 79–96, 1979.

[76] J. H. S. Lee, "Dynamic parameters of gaseous detonations," Annual Review of Fluid Mechanics, vol. 16, no. 1, pp. 311–336, 1984.

[77] W. G. Vincenti and C. H. Kruger, Introduction to physical gas dynamics. Krieger, 1975.

[78] D. R. Kassoy, "A theory of adiabatic, homogeneous explosion from initiation to completion," Combustion Science and Technology, vol. 10, no. 1-2, pp. 27–35, 1975.

[79] B. J. Alder and T. E. Wainwright, "Studies in molecular dynamics. 1. General method," J. Chem. Phys., vol. 31, no. 2, pp. 459–466, 1959.

[80] T. Pöschel and T. Schwager, Computational granular dynamics: models and algorithms. Springer-Verlag, Berlin, Heidelberg, New York, 2005.

[81] Y. Song, R. M. Stratt, and E. A. Mason, "The equation of state of hard spheres and the approach to random closest packing," J. Chem. Phys, vol. 88, pp. 1126–1133, 1988.

[82] J. W. Meyer and A. K. Oppenheim, "On the shock-induced ignition of explosive gases," in Symposium (International) on Combustion, vol. 13, pp. 1153–1164, Elsevier, 1971.

[83] C. Gardner, Experimental investigation of auto-ignition delay times and soot formation in gaseous fuel mixtures. PhD thesis, University of Wales, 2010.

[84] K. Seshadri, N. Peters, and G. Paczko, "Rate-ratio asymptotic analysis of autoignition of n-heptane in laminar nonpremixed flows," Combustion and Flame, vol. 146, no. 1, pp. 131 – 141, 2006.

[85] P. Saxena, N. Peters, and F. A. Williams, "An analytical approximation for high-temperature autoignition times of higher alkanes," Combustion and Flame, vol. 149, no. 1, pp. 79 – 90, 2007.

[86] J. W. Meyer and A. K. Oppenheim, "Coherence theory of the strong ignition limit," Combustion and Flame, vol. 17, no. 1, pp. 65 – 68, 1971.

[87] A. Khokhlov, "Development of hot spots and ignition behind reflected shocks in $2H_2 + O_2$," in Proceedings of the 25th ICDERS, 2015.

[88] K. P. Grogan and M. Ihme, "Weak and strong ignition of hydrogen/oxygen mixtures in shock-tube systems," in Proceedings of the Combustion Institute, vol. 35, pp. 2181 – 2189, 2015.

[89] A. V. Eletski, A. N. Starostin, and M. D. Taran, "Quantum corrections to the equilibrium rate constants of inelastic processes," Phys. Usp., vol. 48, pp. 281–294, 2005.

[90] A. V. Drakon, A. V. Emelianov, A. V. Eremin, E. V. Gurentsov, Y. V. Petrushevich, A. N. Starostin, M. D. Taran, and V. E. Fortov, "Quantum phenomena in ignition and detonation at elevated density," Phys. Rev. Lett., vol. 109, p. 183201, 2012.

[91] G. J. Sharpe, "Shock-induced ignition for a two-step chain-branching kinetics model," Physics of Fluids, vol. 14, pp. 4372–4388, 11 2002.

[92] G. J. Sharpe and N. Maflahi, "Homogeneous explosion and shock initiation for a three-step chain-branching reaction model," Journal of Fluid Mechanics, vol. 566, p. 163–194, 2006.

[93] J. O. Hirschfelder, C. F. Curtiss, and R. B. Bird, "Molecular theory of gases and liquids," Molecular theory of gases and liquids, 1964.

[94] S. Falle, "Self-similar jets," Monthly Notices of the Royal Astronomical Society, vol. 250, no. 3, pp. 581–596, 1991.

[95] S. Falle and S. Komissarov, "An upwind numerical scheme for relativistic hydrodynamics with a general equation of state," Monthly Notices of the Royal Astronomical Society, vol. 278, no. 2, pp. 586–602, 1996.

[96] B. Van Leer, "Towards the ultimate conservative difference scheme. iv. a new approach to numerical convection," Journal of computational physics, vol. 23, no. 3, pp. 276–299, 1977.

[97] G. Sharpe and S. Falle, "Numerical simulations of premixed flame cellular instability for a simple chain-branching model," Combustion and Flame, vol. 158, no. 5, pp. 925–934, 2011.

[98] G. Thomas, D. Edwards, J. Lee, R. Knystautas, I. Moen, and Y. Wei, "Detonation diffraction by divergent channels," Dynamics of Explosions, Prog Astro Aero, vol. 106, pp. 144–154, 1986.

[99] J. O. Hirschfelder and C. F. Curtiss, "Theory of detonations. i. irreversible unimolecular reaction," The Journal of Chemical Physics, vol. 28, no. 6, pp. 1130–1147, 1958.

[100] D. H. Wagner, "The existence and behavior of viscous structure for plane detonation waves," SIAM Journal on Mathematical Analysis, vol. 20, no. 5, pp. 1035–1054, 1989.

[101] W. Wood, "Existence of detonations for small values of the rate parameter," The Physics of Fluids, vol. 4, no. 1, pp. 46–60, 1961.

[102] W. Rakotoarison and M. I. Radulescu, "A dynamical system approach for solving the steady structure of high speed deflagrations," Proceedings of the Combustion Institute, 2022.

[103] J. Powers, Combustion Thermodynamics and Dynamics. Cambridge University Press, Apr. 2016.

[104] S. Strogatz, Nonlinear dynamics and chaos. Addison-Wesley, 1994.

[105] D. G. Goodwin, H. K. Moffat, I. Schoegl, R. L. Speth, and B. W. Weber, "Cantera: An object-oriented software toolkit for chemical kinetics, thermodynamics, and transport processes." https://www.cantera.org, 2022. Version 2.6.0.